UNIVERSITY OF OKLAHOMA

GRADUATE COLLEGE

FUSION OF MULTIPLE INERTIAL MEASUREMENTS UNITS AND ITS APPLICATION IN REDUCED COST, SIZE, WEIGHT, AND POWER SYNTHETIC APERTURE RADARS

A DISSERTATION

SUBMITTED TO THE GRADUATE FACULTY

in partial fulfillment of the requirements for the

Degree of

DOCTOR OF PHILOSOPHY

By

BRIAN M. SUN
Norman, Oklahoma
2022

FUSION OF MULTIPLE INERTIAL MEASUREMENTS UNITS AND ITS APPLICATION IN REDUCED COST, SIZE, WEIGHT, AND POWER SYNTHETIC APERTURE RADARS

A DISSERTATION APPROVED FOR THE
SCHOOL OF ELECTRICAL AND COMPUTER ENGINEERING

BY THE COMMITTEE CONSISTING OF

Dr. Jay McDaniel, Chair

Dr. Mark Yeary, Co-Chair

Dr. Hjalti Sigmarsson

Dr. Caleb Fulton

Dr. Nathan Goodman

Dr. Jeff Basara

This work is dedicated to my wife, my son, and my family. Without their support and encouragement this work would not have been possible.

Acknowledgments

I greatly thank Dr. Jay McDaniel for his support, guidance and advisement through this work. Without Dr. McDaniel and his efforts in supporting and providing fantastic feedback this work not have been successful. Dr. McDaniel showed me how to always keep in mind the application and importance of my research and encouraged me to provide data for how to implement and apply the work.

I am also very grateful for the encouragement and support provided by Dr. Mark Yeary. Dr. Yeary encouraged me to pursue a doctoral degree and was insurmountable in removing challenges and obstacles while I worked through this work. Dr. Yeary taught me to work efficiently and effectively when conducting research.

I would also like to thank Dr. Nathan Goodman for his advisement and technical expertise during challenging times during this work. Dr. Goodman provided incredibly helpful insights on topics in this work. The technical insights provided were key to overcoming some of the key issues encountered during this work. Dr. Goodman taught me the importance of connecting the big picture to the results.

I show great appreciation for my colleague Russell Kenney for his assistance and diligence in providing the system used in this research. Russell also provided a great sounding board and insight into possible issues throughout the project he also is a great partner in operating the system. His donated tireless hours were crucial in making sure the experiments ran smoothly and effectively.

Lastly, I am forever in debt to my wife, Alex who supported me in my worst times and encouraged me in my best times. Her assistance in keeping our beautiful son distracted when I was a giant ball of stress was critical in the completion of this work. She found the energy to encourage me and lift me up during my worst times and launched a business and career during this work. I am incredibly inspired by her and am forever thankful for her.

Table of Contents

List of Tables

List of Figures

Abstract

Position navigation and timing (PNT) is the concept of determining where an object is on the Earth (position), the destination of the object (navigation), and when the object is in these positions (timing). In autonomous applications, these three attributes are crucial to determining the control inputs required to control and move the platform through an area. Traditionally, the position information is gathered using mainly a global positioning system (GPS) which can provide positioning sufficient for most PNT applications. However, GPS navigational solutions are limited by slower update rates, limited accuracy, and can be unreliable. GPS solutions update slower due to the signal having to travel a great distance from the satellite to the receiver. Additionally, the accuracy of the GPS solution relies on the environment of the receiver and the effects caused by additional reflections that introduce ambiguity into the positional solution. As result, the positional solution can become unstable or unreliable if the ambiguities are significant and greatly impact the accuracy of the positional solution. A common solution to addressing the shortcomings of the GPS solution is to introduce an additional sensor focused on measuring the physical state of the platform. The sensors popularly used are inertial measurement units (IMU) and can help provide faster positional accuracy as the transmission time is eliminated. Furthermore, the IMU is directly measuring physical forces that contribute to the position of the platform, therefore, the ambiguities caused by additional signal reflections are also eliminated. Although the introduction of the IMU helps mitigate some of the shortcomings of GPS, the sensors introduce a slightly different set of challenges. Since the IMUs directly measure the physical forces experienced by the platform, the position is estimated using these measurements. The estimates of position utilize the previously known position and estimate the changes to the position based on the accelerations measured by the IMUs. As the

IMUs intrinsically have sensor noise and errors in their measurements, the noise errors directly impact the accuracy of the position estimated. These inaccuracies are further compounded as the erroneous position estimate is now used as the basis for future position calculations. Inertial navigation systems (INS) have been developed to pair the IMUs with the GPS to overcome the challenges brought by each sensor independently. The data provided from each sensor is processed using a technique known as *data fusion* where the statistical likelihood of each positional solution is evaluated and used to estimate the most likely position solution given the observations from each sensor. Data fusion allows for the navigation solution to provide a positional solution at the sampling rate of the fastest sensor while also limiting the compounding errors intrinsic to using IMUs.

Synthetic aperture radar (SAR) is an application that utilizes a moving radar to synthetically generate a larger aperture to create images of a target scene. The larger aperture allows for a finer spatial resolution resulting in higher quality SAR images. For synthetic aperture radar applications, the PNT solution is fundamental to producing a quality image as the range to a target is only reported by the radar. To form an image, the range to each target must be aligned over the coherent processing interval (CPI). In doing so, the energy reflected from the target as the radar is moving can be combined coherently and resolved to a pixel in the image product. In practice, the position of the radar is measured using a navigational solution utilizing a GPS and IMU. Inaccuracies in these solutions directly contribute to the image quality in a SAR system because the measured range from the radar will not agree with the calculated range to the location represented by the pixel. As a result, the final image becomes unfocused and the target will be blurred across multiple pixels.

For INS systems, increasing the accuracy of the final position estimate is de-

pendent on the accuracy of the sensors in the system. An easy way to increase the accuracy of the INS solution is to upgrade to a higher grade IMU. As a result, the errors compounded by the IMU estimations are minimized because the intrinsic noise perturbations are smaller. The trade-off is the IMU sensors increase in cost, size, weight, and power (C-SWAP) as the quality of the sensor increases. The increase in C-SWAP is a challenge of utilizing higher grade IMUs in INS navigational solutions for SAR applications. This problem is amplified when developing miniaturized SAR systems. In this dissertation, a method of leveraging the benefits of data fusion to combine multiple IMUs to produce higher accuracy INS solutions is presented. Specifically, the C-SWAP can be reduced when utilizing lower-quality IMUs. The use of lower quality IMUs presents an additional challenge of providing positional solutions at the rates required for SAR. A method of interpolating the position provided by the fusion algorithm while maintaining positional accuracy is also presented in this dissertation.

The methods presented in this dissertation are successful in providing accurate positional solutions from lower C-SWAP INS. The presented methods are verified in simulations of motion paths and the results of the fusion algorithms are evaluated for accuracy. The presented methods are instrumented in both ground and flight tests and the results are compared to a 3rd party accurate position solution for an accuracy metric. Lastly, the algorithms are implemented in a miniaturized SAR system and both ground and airborne SAR tests are conducted to evaluate the effectiveness of the algorithms. In general, the designed algorithms are capable of producing positional accuracy at the rate required to focus SAR images in a miniaturized SAR system.

1 Introduction

Advancements in vehicles and moving platforms are allowing for an increasing amount of sophisticated systems to be deployed for accomplishing various tasks. The vehicles have made it possible to reach areas and traverse terrain with greater efficiency. As the development of these platforms has evolved the need for accurate position solutions has increased. The systems deployed on these vehicles are becoming more and more reliant on knowing where the platform is at any given time. For systems that are traversing an area, it is crucial to know the current position, relative to the destination, to reach the desired destination. Other systems that are gathering intelligence over an area rely on the position of the platform to understand the information received. In both applications, positional accuracy plays a big role in producing the desired outcome. Additionally, these applications rely on accurate timing to understand how to navigate the platform to the desired destination or how the intelligence collected is changing with time.

The concept of *navigation* is the act of monitoring and controlling the movement of a platform from one location to another. The location of a vehicle or platform at a specific time are needed to navigate and control the trajectory of the platform. Depending on the abilities of the platform, parameters of the platform will need to be manipulated to control or change the trajectory of the platform. How these parameters are manipulated rely on knowledge of where the platform is relative to the destination at any point in time. Navigational systems are used to produce the position of the platform at any given time satisfying a concept known as position, navigation, and timing (PNT). The concept of PNT is self explanatory but presents a significant challenge in practice and current solutions focus on providing solutions on Earth. Methods used to produce the location on Earth includes but are not limited to the use of navigating using the stars, satellites, and inertial

measurements. Navigation by the stars is done by determining the location of the platform relative to the constellations. The main limitation of navigation by the stars is that it is less effective during the day as the constellations are not visible. Satellite navigation overcomes the limitation as the solution is available during the day as well as the night. In addition, the satellites produce a location that is relative to the satellites that are placed in geosynchronous orbit. All these concepts share a similar basis where the PNT solution is relative to a known position in Euclidean space. The core issue becomes how is the Euclidean space defined for the known position compared to the PNT solution. As a result, the core challenge of producing an accurate PNT solution is reliant on a deep understanding of what the PNT solution is relative to. This challenge is amplified when system and measurement uncertainty is taken into account.

Traditionally, PNT solutions use a global positioning system (GPS) to determine the location of the navigating body. GPS provides PNT by creating a network of satellites that are deployed such that the location of each satellite relative to the Earth's surface is known for any given time. The range to each of these satellites can be estimated for a given point on the Earth and the position can be triangulated using these ranges. One drawback for radar applications is GPS typically updates at lower frequencies than traditional radar pulse repetition frequencies (PRFs), typically on the order of 50 Hz. Furthermore, the accuracy is approximately 30 centimeters using the recently established L5 band. As known, the L-band is the IEEE designation for the range of frequencies in the radio spectrum from 1 to 2 GHz [5]. Within the L-band, L5 is a new signal designed for civilian use and it is centered at 1176 MHz. However, utilization of the L2 band produces a positional accuracy on the order of 1 meter.

Modern-day synthetic aperture radar (SAR) systems require a precise position,

navigation, and timing (PNT) solution to accurately determine its relative position in space. This allows for the range from the navigating body to any scatterer in the target scene, over the coherent processing interval (CPI), to be precisely known. During radar signal processing of the captured data, such as the backprojection algorithm [18], phase correction of the slow-time data is performed before Doppler processing so that all of the power is compressed into the appropriate range bins. However, to achieve a focused image as described, the relative position in space must be accurate to within a fraction of a wavelength [19], which is determined by the frequency of the transmitted signal. Therefore, for higher transmitted frequencies, such as those used in millimeter-wave SAR, a highly precise navigation solution is required. Moreover, since several pulses of data will be captured over the CPI, it is highly desirable to have a PNT solution on a pulse-by-pulse basis so that the phase can be accurately compensated on each fast-time data set during processing. If implemented correctly, the resultant is a focused black and white image of the target scene.

1.1 Motivation

Recent developments in small-form unmanned aerial vehicles (UAV) have drastically accelerated the need for miniaturization of aerial payloads such as target detection and imaging [16]. In SAR systems, the miniaturization of the antenna drives an increase in operational frequency. Increases in operational frequency results in a lower error tolerance in radar imaging techniques. As a result, reliable timing and position systems are required of the platform. As the development of smaller autonomous vehicles continue the goal of miniaturization of platforms is a large area of interest [55]. The effort in miniaturization of SAR systems is twofold, one is to miniaturize the platform as a whole and the other is to miniaturize the

systems deployed to the platform. The first effort allows for smaller platforms are developed such as drones and quad-copters to accomplish specialized tasks that do not require a large vehicle. The other effort allows for additional versatility as more systems to be deployed to the platform without increasing the size of the platform as a whole. Overall, the miniaturization effort is often measured by the reduction in cost, size, weight, and power (C-SWAP) of the system. As the PNT solution is a critical component of a radar, the reduction of C-SWAP in the PNT subsystem is critical in the miniaturization of imaging radars.

The utilization of satellite navigation alone is insufficient for SAR applications due to a multitude of limitations. The main limitation of satellite navigation for radar imaging is that the update rate of the position estimates is often slow due to the long transmission range of the satellite. Furthermore, these transmissions are calculations of the range between the receiver and the satellite. The location of the platform on earth can then be calculated from the range given the location of the satellite. Another limitation to satellite communication is that the communications rely on line of sight and the range measurement can be inaccurate if the signal is reflected before it is received by the receiver. One method of overcoming the limitations of satellite navigation is the use of inertial sensors which measure the accelerations undergone by the platform. Using these sensors the initial position is used to calculate the new position given the change in time δt. Inertial sensors often update at faster rates than satellite receivers and can more reliably produce a navigation solution. However, these sensors can produce inaccurate position solutions as the sensor errors are compounded as the accelerations are integrated and the calculated position estimate is the basis of the next position calculation. The true location of the platform is non-trivial to obtain as the sensors used to measure the location all introduce some amount of uncertainty. In addition, the reference point

used to determine the location is different for each coordinate frame. The coordinate frames are discussed in section 2. In order to produce a high quality product in radar imaging applications it is of great interest to increase the frequency of PNT solutions to be synchronous with radar PRFs.

Most navigation systems leverage multiple sensors to overcome the shortcomings of each independent sensor. A common approach is to use a global positioning system (GPS) satellite receiver to achieve accurate position measurements and an inertial measurement unit (IMU) to capture and estimate the position when GPS updates are unavailable [64, 74]. In this configuration, the accuracy and timing of the GPS satellites are leveraged to overcome the errors caused by IMU and the IMU helps produce position solutions at a faster rate than GPS. Additionally, the IMU is also able to produce position solutions in the event the GPS signal is unavailable. The integration of these measurements is commonly done by *data fusion*.

Another challenge of satellite navigation is GPS requires an open sky to obtain a signal to provide a viable position solution, and signal integrity can degrade significantly as the navigating body traverses different environments. The low update rate and the possibility of signal loss contribute to the main disadvantages of GPS [12, 60]. An inertial measurement unit (IMU), commonly used in conjunction with GPS, often provides data at a higher PRF, typically on the order of 100 to 200 Hz. The IMU provides data that allows for the estimation of the navigating body's current position, and the faster update rate of the IMU data allows for position estimates to be reported more often than GPS. One major advantage of the IMU is that it can provide position estimates down to an accuracy of 1 millimeter if an ultra-low bias navigational grade unit is used. However, this increased accuracy comes at the expense of a higher cost, bulkier, and heavier unit. Additionally, IMUs will drift or "walk", and the associated errors are compounded as the position estimate

is made over time [27]-[30]. Moreover, IMUs provide position estimates based on acceleration and gyroscopic measurements, and the error increases at a significant rate since the position is calculated by integrating the drifting IMU accelerometer and gyroscope measurements [53]. For SAR, either of these solutions can be used independently in low transmitted frequency or short-duration applications. If either of these criteria are to be exceeded, a more complex PNT solution is required.

Given the shortcomings of current PNT solutions that utilize a single IMU and GPS, a solution of producing accurate PNT solutions at the rates on the order of SAR PRFs is needed. In addition, the PNT solution developed needs to also minimize the C-SWAP in order to be deployed on the new miniaturization of SAR systems.

The application of reduced C-SWAP PNT solutions extends beyond SAR. The technology will enable the development of smaller platforms that require PNT solutions. These applications include miniature unmanned aerial vehicles (UAV), autonomous cars, and other autonomous systems. Furthermore, the use of data fusion to achieve more accurate positional accuracy by adding more sensors is a key enabler to reducing C-SWAP without having to sacrifice positional accuracy in these applications.

2 Navigation Basics

In order to determine the location of an entity, measurements of the entity relative to external reference point is required. These measurements can be ranges to known locations and the location of the entity is triangulated based on measurements relative to the known locations. In the case of self-locating, the measurements can be the external forces experienced by the platform. The forces can be in the form of accelerations and angular rotations experienced by the platform. In this chapter, the devices, or sensors, used to obtain the measurements and the reference external reference points are detailed. In addition, the challenges of utilizing these sensors in a PNT solution are described. Similarly, methods of utilizing the information gathered by the sensors to find produce the positional solution are presented in this chapter. The errors and challenges from the methods and sensors described in this chapter are a major cause of poor quality SAR images that are described in future chapters.

2.1 Sensors

The information required to calculate the position of the platform is measured using GPS, gyroscopes, and accelerometers. These three sensor types are used to measure and quantify the position and physical forces the platform experiences. The physical forces can be used in with the last known position to estimate the current position of the platform. Gyroscopes and accelerometers measure the angular rate and specific force, respectively. *Inertial sensors* are sensors that measure physical forces on the platform with no external reference. Sensors like GPS that measure the position and velocity of the platform relative to an external source are not considered to be inertial sensors. In addition, inertial measurement units (IMUs) are combinations of accelerometers and gyroscopes. IMUs typically are comprised of 3

of each sensor to sense the physical forces in the three-dimensional Cartesian coordinate system. The IMU is the primary sensor in an inertial navigation system. The construction of accelerometers generally uses a mass coupled with a spring system along the sensitive axis. As the mass is displaced by acceleration, the displacement of the mass can be sensed by the springs. Based on the known spring constant and the amount of the known mass was displaced the acceleration experienced can be reported. As a result, the bigger the mass the more sensitive the accelerometer. In the same vein, gyroscopes use a similar concept and larger masses lead to a more sensitive gyroscope. The larger, more sensitive sensors also scale in costs as the sensors are larger and have to be more precisely manufactured to optimize the performance. Micro-electromechanical systems (MEMS) sensors are also available and offer lower-cost manufacturing in smaller packages at the cost of performance. MEMS sensors can provide the optimal solutions for specific applications where factors such as shock tolerance or size, weight, and power (SWaP) restrict the use for larger more precise sensors. As a result, there are five categories of these sensors that help engineers narrow the quality of the sensor for the specific application. The five categories are marine, aviation, intermediate, tactical, and consumer. Each of these categories provides a performance of ~ 1.8 km in the first 24 hours, ~ 1.5 km in the first hour, and ~ 15 km in the first hour for marine, aviation, and intermediate grades respectively. In addition, the tactical grade IMUs can only be used for inertial navigation systems for a few minutes and the consumer-grade requires significant calibration to be able to be used for inertial navigation applications.

2.1.1 GPS

GPS sensors calculate the range the platform is from the network of satellites in geostationary orbit. Geostationary orbit means the satellites are in the same location

relative to the rotation of the Earth. The more satellites the range is calculated from the more accurate the position is. The platform range to a single satellite produces a sphere of possible locations the platform can be. As the number of satellites in the network is increased the position possibilities are limited by the intersection of each of the spheres created by the different satellites. These ranges are calculated using a stable clock signal and transmitting when and where the satellite was when the signal was transmitted. The range can then be calculated by taking the difference between the time the signal was received and the time the signal was transmitted and multiplying by the propagation speed (i.e, speed of light). The ranges from each satellite can then be used to triangulate the location of the platform relative to the satellite network. Since the satellite network is synchronous to the Earth's orbit the location on the earth can accurately be calculated.

2.1.2 Issues with GPS

Since GPS range is based on the transmissions from the satellite, the signal can only be received if there is a line-of-sight (LOS) between the satellite and the receiver. In many cases, the line of sight may not be achievable to multiple satellites in the network. In urban environments, signals can be obstructed by buildings and structures and can get erroneous signals that are reflections from the surrounding buildings. The reflections are not the expected direct path from the satellite to the receiver and translate to an often longer range as the signal is a sum of the distance from the satellite to the reflection point and the receiver distance from the reflection point. Environmental terrain can also obstruct the signal from lower elevation satellites. In addition to signal obstructions, GPS errors can come from transmission delays as the signal propagates through the ionosphere and troposphere [52]. These delays increase the possible range of the platform, resulting in less accuracy.

Signal attenuation also introduces error into the position estimation of the platform. As the receiver moves into an environment that contains overhead cover such as indoors or areas with dense foliage, the signal becomes attenuated. The attenuation causes poor signal-to-noise ratios and the receiver is unable to receive the information required to triangulate position. The same scenario occurs when the signal is severely degraded due to jamming or RF interference in dense RF environments. Furthermore, these issues cause difficulty in obtaining the positional solution making the accuracy of GPS systems to be limited to meter accuracy.

2.1.3 Real-Time Kinematic (RTK)

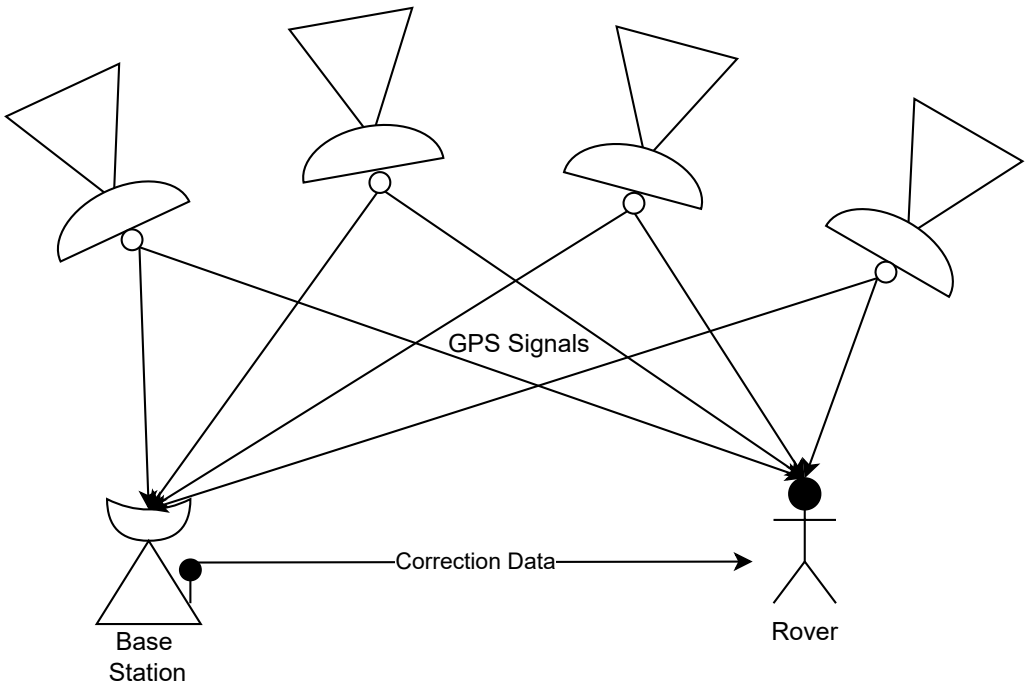

Figure 2.1: Concept of RTK GPS. GPS signals are received at the base station and the rover the position errors are estimated at the base station and the correction data is sent to the rover.

One way to improve the accuracy of the GPS sensors is to utilize a technique known as Real-Time Kinematic positioning. The technique utilizes multiple ground stations to help correct the errors caused by satellite transmission of GPS signals. RTK is a surveying technique that takes GPS measurements at a base station and calculates the pseudo-range errors for the received signals. The idea is that the position of the base station is known as it is stationary. When the base station is deployed the GPS positions are accumulated for a long time and the positions are averaged to obtain an accurate position of the base station. In general, the longer the GPS positions of the base station are accrued the better the accuracy of the position of the base station. As a result, the pseudo-range errors are more accurate. The pseudo-range errors are calculated using a binary sequence that is known between the satellite and the receiver. As the receiver's sequence is delayed to match the satellite, the transmission delay can be calculated. This delay is used to correct the GPS errors caused by transmission delays from the satellite. In addition, the range to the rover from the base station can be calculated and position corrections calculated at the base station can be transmitted to correct the rover's position.

2.1.4 Accelerometers

Accelerometers are sensors that measure acceleration along a sensitive axis. The design of these sensors utilizes a mass-spring system to measure the displacement experienced by the mass during acceleration. The idea is that the mass is suspended between two springs and encased in a case. As the sensor accelerates the position of the mass relative to the case changes and the forces the springs exert on the mass change. As the spring constants are known, the position of the mass relative to the case can be used to calculate the acceleration undergone by the sensor.

In three-axis IMUs, there are 3 mass-spring systems with each of their sensi-

tive axes making up a Cartesian coordinate frame. This coordinate frame is often aligned or transformed to the coordinate frame of the navigational body based on the mounting orientation of instrumentation.

One limitation to accelerometers is the measurement of gravitational forces where gravity applies a force to the frame and the mass of the sensor equally. As a result, there is no positional change between the mass and the case resulting in no acceleration in measurement. Furthermore, accelerometers measure only non-gravitational acceleration. Measurements from the accelerometers are often expressed in g where $1g = 9.80665\frac{m}{s^2}$.

2.1.5 Gyroscopes

Gyroscopes, or gyros for short, measure the angular velocities experienced by the sensor. A common implementation of gyros is the utilization of a spinning disk. The free-spinning disk is mounted in such a way that the axis of rotation of the disk is perpendicular to the sensitive axis. As this mass spins Newton's third law of motion applies where the angular momentum is conserved. In this way, the free-spinning disk will remain rotating in the same axis even if an angular velocity is applied to the case. As a result, the angular difference between the spinning disk and the case can be used to measure the angular velocity experienced by the sensor.

Other designs of gyros involved fiberoptics arranged in a ring. As a signal is transmitted through the fiberoptic ring the time the signal takes to traverse the ring is measured. As angular rotation is applied to the sensor, the time for the signal to traverse the ring changes proportionally with the angular velocity experienced. In this way, the fiberoptic ring can sense the angular velocity experienced. The angular velocity is often measured in $\frac{^\circ}{s}$ or $\frac{radians}{s}$. Gyros also are often aligned to the same axis as accelerometers in instrumentation. Doing so allows for acceleration

and rotations to be measured by the accelerometers and gyros for that Cartesian coordinate frame. This allows for characterization of how the sensor is moving along the axes and how the orientation of the sensor is changing with respect to the axes. Inertial measurement units(IMUs) are often instrumented this way where 3 accelerometers and 3 gyros are packaged to sense rotations and accelerations of the coordinate frame.

2.2 Coordinate Frames

In navigation there are many frames of reference to describe the location of an object on Earth. These coordinate frames help link the measurement of a sensor to the physical location on the planet. In general, the coordinate frames all have a different point of reference. For example, the sensor has a coordinate frame defined where the origin is centered on the sensor whereas the Earth-centered coordinate frames have the core of the earth as the origin. Understanding the differences between these coordinate frames for navigation is crucial to obtaining an accurate position estimate. These coordinate frames give context to the location or orientation given. The systems define key references to describe an object. For example, an arbitrary position point of X, Y, Z does not give context to how the location is changing relative to the planet. However, an X, Y, Z value in a specific coordinate system can help distinguish if the position is rotating with the planet or staying constant independent from the rotational effects of the planet. This key detail is important when describing a location on the surface of the Earth as opposed to an object in space. In addition, some of the frames are better at distinguishing the attitude of the navigational body as opposed to the physical location of the body. For instance, the coordinate frame that is tied and oriented to the navigational platform is useful for measuring the attitude changes of the platform instead of the location

of the platform. The frames relevant to this paper are the Earth-centered inertial (ECI), Earth-centered Earth Fixed (ECEF), north, east, down (NED), and the body frame. A picture of each of the relevant coordinate frames is shown in Fig. 2.2.

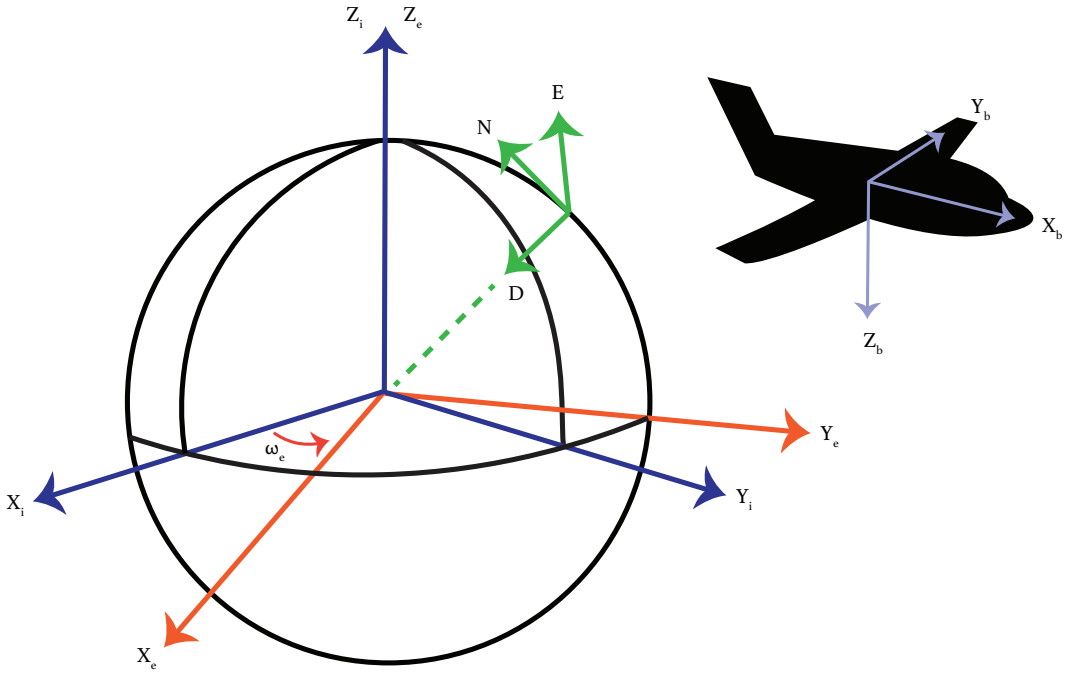

Figure 2.2: Coordinate frames used in navigation. ECI frame is shown in blue, ECEF frame is shown in orange, NED frame is shown in green, and body frame is shown in light blue on the aircraft.

2.2.1 Earth-Centered Inertial (ECI)

The origin of the ECI frame is defined at the center of the Earth and does not accelerate or rotate with the Earth. The z-axis points to the north pole and is along the Earth's axis of rotation. The X and y-axis are aligned with the equator completing a right-hand Cartesian coordinate system. The X-axis is aligned with pointing to the Sun at the vernal equinox. This coordinate frame is useful for interpreting the measurements from inertial sensors which take measurements in an inertial coordi-

nate frame. As this coordinate system does not rotate, it is useful for determining the location of spacecraft and other navigational entities in space. The ECI frame is denoted by i in this dissertation.

2.2.2 Earth-centered Earth Fixed (ECEF)

The ECEF frame is defined with the origin at the center of the Earth. There are 2 key points for the ECEF frame the first is the intersection between the equator and the 0° longitude, popularly known as the IERS Reference Meridian (IRM). The second key point is the north pole. The x-axis of the ECEF frame points to the first key point and the z-axis points to the north pole with the y-axis completing the right-hand Cartesian coordinate system pointing at 90° longitude. The ECEF coordinate plane rotates along the z-axis at a rate equivalent to the rotation of the Earth. As a result, the coordinate frame is useful for determining the location relative to the Earth. The ECEF frame is denoted by e in this dissertation.

2.2.3 North, East, Down

The NED frame is defined to be on the surface of the earth where the z-axis is pointing toward the center of the earth. The x-axis is aligned with the north pole and the y-axis points East to complete the coordinate frame. This coordinate frame is useful for determining the orientation of the navigational body relative to North, East, and Down. This frame's origin is not fixed and is based on the location on Earth and as a result, this frame is not used as a reference frame but is useful for understanding attitude and velocity changes in position relative to the surface of the Earth. These attitude and velocity changes can then be used to align the measurements from the navigating body to a fixed orientation. Due to the frame definition pointing to the north pole, the frame has a major limitation at the poles of

the Earth as the North axis becomes undefined. The NED frame is denoted as n in this dissertation.

2.2.4 Body frame

The body frame is the coordinate frame that is tied to the navigational body. The x-axis points to the forward direction of the navigational body and the z-axis points down on the navigational body and the y-axis completes the right-hand Cartesian coordinate system. The origin of this frame is the same as the NED frame and is useful for understanding the orientation of the navigational body. In addition, the changes in attitude measured by the onboard sensors can be aligned with this frame. Onboard sensors often have their orientation fixed to this frame. This frame is denoted by b in this dissertation.

2.2.5 Coordinate Transformations

In order to resolve the location of a navigational body, a way to transform measurements, orientations, and locations in the multiple coordinate frames is necessary. Transformations between these frames can be done based on resolving the orientations of each of these coordinate frames with respect to each other. To put it simply, the measurements in one coordinate frame can be expressed in a different coordinate frame through a series of rotations and projections. These rotations and projections can be done using Euler angles and trigonometry. In the 2-dimensional case with two coordinate systems that share a similar origin. The transformation can be done by projecting the location from one coordinate frame onto another. An example of the 2d transformation case is shown in 2.3.

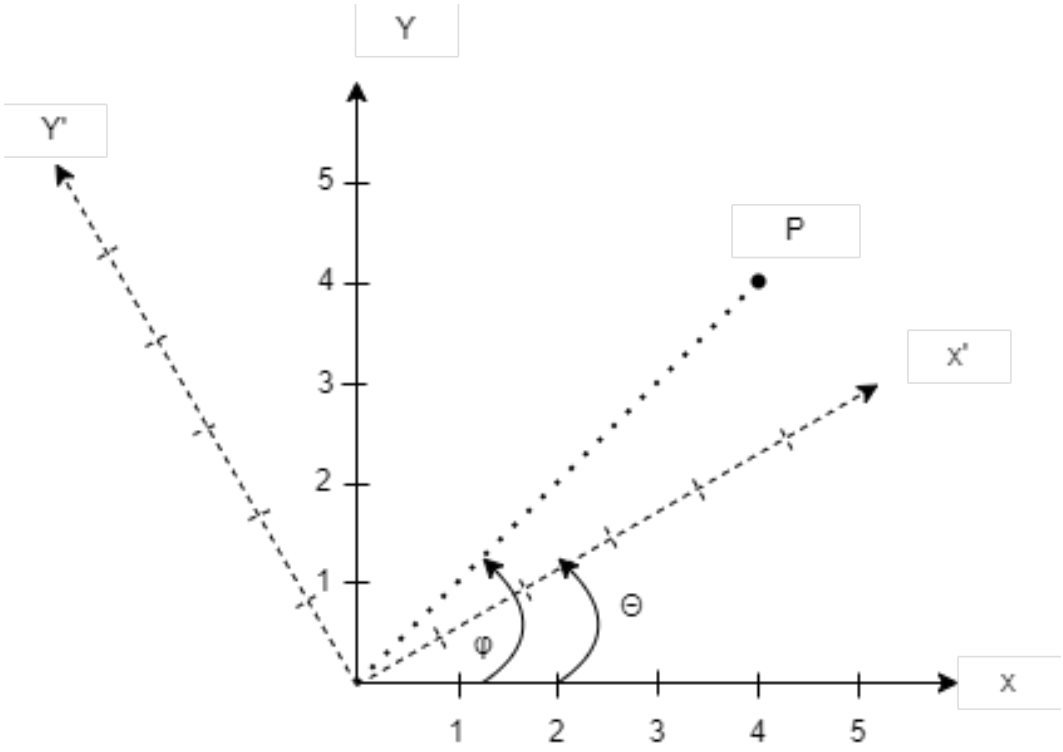

Figure 2.3: 2d transformation of a point between two coordinate systems. The dotted coordinate system is a rotation of the solid coordinate frame by the angle θ.

For example, in 2.3 the transformation of point P from the solid coordinate frame to the dotted coordinate frame can be calculated by

$$P_{Y'} = \sqrt{(}P_X^2 + P_Y^2)\sin(\phi) \tag{2.1}$$

and

$$P_{X'} = \sqrt{(}P_X^2 + P_Y^2)\cos(\phi) \ . \tag{2.2}$$

where P_X and P_Y are the x and y coordinates of point P in the solid coordinate system and $P_{X'}$ and $P_{Y'}$ are the x and y coordinates in the dotted coordinate frame in Fig. 2.3. Furthermore, the angles ϕ is the angles from the solid coordinate system to vector P and θ is the angle of rotation between the solid coordinate system and

the dotted coordinate system. Conversely, the point P can be converted back from the dotted coordinate frame to the solid frame by

$$P_Y = \sqrt{(}P_{x'}^2 + P_{y'}^2)\sin(\phi + \theta) \tag{2.3}$$

and

$$P_X = \sqrt{(}P_x^2 + P_y^2)\cos(\phi + \theta) \ . \tag{2.4}$$

The magnitude of the vector P can be simplified to $r = \sqrt{(}P_x^2 + P_y^2)$ and using the trigonometric identity of

$$\cos(A + B) = \cos(A)\cos(B) - \sin(A)\sin(B) \tag{2.5}$$

The transformation between the two coordinate frames can be generalized to any points by using a transformation matrix shown by

$$\begin{bmatrix} X' \\ Y' \end{bmatrix} = \begin{bmatrix} cos\phi & -sin\phi \\ sin\phi & cos\phi \end{bmatrix} \begin{bmatrix} X \\ Y \end{bmatrix} \tag{2.6}$$

where

$$C_{XX'} = \begin{bmatrix} cos\phi & -sin\phi \\ sin\phi & cos\phi \end{bmatrix} \tag{2.7}$$

is defined as the rotation matrix required to transform from the dotted coordinate frame X', Y', Z' to the solid coordinate frame X, Y, Z. Extrapolating this concept to 3 dimensions is similar in concept where the location is rotated to the new coordinate frame. The key difference in the 3-dimensional case is that rotations along one dimension can cause additional changes in rotations for other axes. As a result, the order of rotation is important when transforming 3-dimensional coordinate frames. Euler rotation matrices in 3 dimensions are calculated by combining the ro-

tation matrix in each Cartesian axis. For instance, an Euler rotation that is done by rotating about the x, y, and z-axis in the respective order can be calculated by multiplying the rotation matrix about x (C_x), the rotation matrix about y (C_y), and the rotation matrix about z (C_z). The rotation matrix in each of these axis are expressed by

$$C_x = \begin{bmatrix} 1 & 0 & 0 \\ 0 & cos\phi & -sin\phi \\ 0 & sin\phi & cos\phi \end{bmatrix} \tag{2.8}$$

$$C_y = \begin{bmatrix} cos\theta & 0 & sin\theta \\ 0 & 1 & 0 \\ -sin\theta & 0 & cos\theta \end{bmatrix} \tag{2.9}$$

$$C_z = \begin{bmatrix} cos\psi & -sin\psi & 0 \\ sin\psi & cos\psi & 0 \\ 0 & 0 & 1 \end{bmatrix} \tag{2.10}$$

where θ, ϕ,and ψ are the angle of rotation about the respective x, y, z axes. As a result. the Euler rotation matrix in the order of X, Y, Z, denoted by C_{xyz} is equivalent to

$$C_{xyz} = C_x C_y C_z = \begin{bmatrix} 1 & 0 & 0 \\ 0 & cos\theta & -sin\theta \\ 0 & sin\theta & cos\theta \end{bmatrix} \begin{bmatrix} cos\phi & 0 & sin\phi \\ 0 & 1 & 0 \\ -sin\phi & 0 & cos\phi \end{bmatrix} \begin{bmatrix} cos\psi & -sin\psi & 0 \\ sin\psi & cos\psi & 0 \\ 0 & 0 & 1 \end{bmatrix} \tag{2.11}$$

and is evaluated to

$$C_{\text{xyz}} = \begin{bmatrix} C_{xyz}(11) & C_{xyz}(12) & C_{xyz}(13) \\ C_{xyz}(21) & C_{xyz}(22) & C_{xyz}(23) \\ C_{xyz}(31) & C_{xyz}(32) & C_{xyz}(33) \end{bmatrix} \tag{2.12}$$

where each element in the 3d rotation matrix is defined as

$$C_{xyz}(11) = \cos(\phi)\cos(\psi) \tag{2.13}$$

$$C_{xyz}(12) = -\cos(\theta)\sin(\psi) + \sin(\theta)\sin(\phi)\cos(\psi) \tag{2.14}$$

$$C_{xyz}(13) = \sin(\theta)\sin(\psi) + \cos(\theta)\cos(\psi)\sin(\phi) \tag{2.15}$$

$$C_{xyz}(21) = \cos(\phi)\sin(\psi) \tag{2.16}$$

$$C_{xyz}(22) = \cos(\theta)\cos(\psi) + \sin(\theta)\sin(\phi)\sin(\psi) \tag{2.17}$$

$$C_{xyz}(23) = -\sin(\theta)\cos(\psi) + \cos(\theta)\sin(\phi)\sin(\psi) \tag{2.18}$$

$$C_{xyz}(31) = -\sin(\phi) \tag{2.19}$$

$$C_{xyz}(32) = \cos(\phi)\sin(\theta) \tag{2.20}$$

$$C_{xyz}(33) = \cos(\theta)\cos(\phi) \tag{2.21}$$

$$\tag{2.22}$$

In changing the order of the rotations, the structure of the rotation matrix remains the same but the elements of the matrix are calculated by by multiplying the rotation matrices in a different order. For example, a rotation sequence of Z, Y, X, denoted by C_{zyx}, is accomplished by performing the rotations in (2.11) in reverse. Doing so

the rotation matrix calculation as described by (2.11) becomes

$$C_{zyx} = C_z C_y C_x = \begin{bmatrix} cos\psi & -sin\psi & 0 \\ sin\psi & cos\psi & 0 \\ 0 & 0 & 1 \end{bmatrix} \begin{bmatrix} cos\phi & 0 & sin\phi \\ 0 & 1 & 0 \\ -sin\phi & 0 & cos\phi \end{bmatrix} \begin{bmatrix} 1 & 0 & 0 \\ 0 & cos\theta & -sin\theta \\ 0 & sin\theta & cos\theta \end{bmatrix} . \tag{2.23}$$

The resulting elements of the rotation matrix C_{zyx} evaluate to

$$C_{xyz}(11) = \cos(\psi)\cos(\phi) \tag{2.24}$$

$$C_{xyz}(12) = \cos(\psi)\sin(\phi) + \sin(\theta) - \sin(\psi)\cos(\theta) \tag{2.25}$$

$$C_{xyz}(13) = \cos(psi)\sin(\phi)\cos(\theta + \sin(\theta)\sin(\psi) \tag{2.26}$$

$$C_{xyz}(21) = \cos(\phi)\sin(\psi) \tag{2.27}$$

$$C_{xyz}(22) = \sin(\psi)\sin(\phi)sin(\theta) + \cos(\psi)\cos(\theta) \tag{2.28}$$

$$C_{xyz}(23) = \sin(\psi)\sin(\phi)\cos(\theta) - \cos(\psi)\sin(\theta) \tag{2.29}$$

$$C_{xyz}(31) = -\sin(\phi) \tag{2.30}$$

$$C_{xyz}(32) = \cos(\phi)\sin(\theta) \tag{2.31}$$

$$C_{xyz}(33) = \cos(\theta)\cos(\phi) \tag{2.32}$$

$$\tag{2.33}$$

In navigation applications, the rotation order of Z,Y,X are useful when orienting the body frame to the NED frame. In doing so allows for the acceleration in the body frame as measured by the IMU to be transformed to the acceleration in the NED frame. Accelerations in the NED frame allow for the calculation of the change in latitude, longitude, and altitude. An example of transforming from the 3-dimensional NED frame to the body frame using a the rotation matrix C_{bn} is shown

in 2.34-2.43.

$$C_{\mathrm{bn}}(11)(k) = \cos(\phi(k))\cos(\theta(k)) \tag{2.34}$$

$$C_{\mathrm{bn}}(12)(k) = \cos(\phi(k))\sin(\theta(k))\sin(\psi(k)) - \cos(\psi(k))\sin(\phi(k)) \tag{2.35}$$

$$C_{\mathrm{bn}}(13)(k) = \sin(\phi(k))\sin(\psi(k)) + \cos(\phi(k))\cos(\psi(k))\sin(\theta(k)) \tag{2.36}$$

$$C_{\mathrm{bn}}(21)(k) = \cos(\theta(k))\sin(\phi(k)) \tag{2.37}$$

$$C_{\mathrm{bn}}(22)(k) = \cos(\phi(k))\cos(\psi(k)) + \sin(\phi(k))\sin(\theta(k))\sin(\psi(k)) \tag{2.38}$$

$$C_{\mathrm{bn}}(23)(k) = \cos(\psi(k))\sin(\phi(k))\sin(\theta(k)) - \cos(\phi(k))\sin(\psi(k)) \tag{2.39}$$

$$C_{\mathrm{bn}}(31)(k) = -\sin(\theta(k)) \tag{2.40}$$

$$C_{\mathrm{bn}}(32)(k) = \cos(\theta(k))\sin(\psi(k)) \tag{2.41}$$

$$C_{\mathrm{bn}}(33)(k) = \cos(\theta(k))\cos(\psi(k)) \tag{2.42}$$

$$\tag{2.43}$$

The GPS latitude, longitude and height are expressed in the NED frame and are converted to the ECEF Cartesian coordinate system by applying a transform. The transform used to convert the GPS coordinates to the ECEF Cartesian coordinates is shown in (2.44)

$$\begin{bmatrix} X \\ Y \\ Z \end{bmatrix} = \begin{bmatrix} (R_E + H_b)\cos(L_b)\cos(\lambda_b) \\ (R_E + H_b)\cos(L_b)\sin(\lambda_b) \\ ((1-e^2)R_E + H_b)\sin(L_b) \end{bmatrix} \tag{2.44}$$

where L_b is the GPS latitude, λ_b is the GPS longitude, H_b is the GPS height, e is the eccentricity of the Earth and R_E is the radius of the earth. This conversion allows for easier plotting and visualization. ECEF coordinates can be visualized in a Cartesian coordinate system whereas the latitude, longitude, and height values

are visualized on a globe. As a result, the latitude, longitude, and height values are often distorted when plotted on a Cartesian system.

2.3 Dead Reckoning

A popular method of predicting a positional solution is known as *dead reckoning*. Dead Reckoning is the method of estimating the position of a moving platform by using speed and heading to predict the position over a specific time. The method uses a motion model to calculate the next known position using information from sensors that measure speed and heading. Given the time elapsed from the last sensor update the position can be calculated by taking the previous known position estimate and adding the velocity vector multiplied by the elapsed time to get the position distanced traversed by the moving platform. This process is done by utilizing

$$P_k = P_{k-1} + v_k dt \tag{2.45}$$

where P_k is the current position, P_{k-1} is the position calculated at the previous time step and $v_k dt$ is the current velocity multiplied by the elapsed time.

Extrapolating the equations to include acceleration allows for the position to be estimated more accurately based on the acceleration experienced by the platform. These accelerations can be measured using an IMU or accelerometers. As a result, The position can be estimated from the IMU measurements using (2.46). In addition, the velocity of the navigating body can be estimated using (2.47).

$$p_k = p_{k-1} + v_k \delta t + \frac{1}{2} a_k \delta t^2 \tag{2.46}$$

$$v_k = v_{k-1} + a_k \delta t \tag{2.47}$$

Where p_k is the position at the current time step, p_{k-1} is the position at the previous time step, v_k is the velocity at the current time step, a_k and a_{k-1} are the accelerations at the current and previous time steps, respectively, and δt is the time difference between the previous and current time steps.

The main limitation of this method of producing a navigational solution is errors in the sensor measurements. The errors caused by the sensor measurements compound and cause the navigation solution to become more erroneous over time as the method is recursive. As shown in equation 2.45, the errors from the current sensor measurement are added to the sensors errors that were included in the previous sensor measurement. As a result, the deviation over time from the true position traversed by the platform is known as *sensor walk* or *sensor drift*. One popular way to combat this is to use higher precision and ultra-low noise sensors that minimize the errors introduced into the system. The current trade-off is that the accuracy of the sensors is proportional to the C-SWAP of the sensors. In general, the C-SWAP of the sensors increases as the accuracy of the sensors increase.

2.4 Motion Model

The values recorded from the instrumented NovAtel IMU unit are acceleration expressed in the body coordinate frame. To process the data in the local north, east, down (NED) frame, the raw IMU values are rotated using an Euler rotation matrix shown in (2.34). These rotation values are used to build the rotation matrices described in the previous section. The rotation sequence used for the rotation matrix is ZYX. The rotation angles of ϕ, θ, and ψ are defined as roll, pitch, and yaw, respectively, as shown in Fig. 2.4, and are acquired from the gyroscope. As explained in [46], the gyroscope measurements can cause errors in attitude determination which significantly impacts the accuracy in the final predicted location of the navigating body. The Earth spin rate and the rate of the NED frame are also included in these measurements and need to be removed to obtain accurate attitude estimation. A detailed explanation of determining attitude from the gyroscope measurements while accounting for Earth effects is explained in [33]. The Earth spin rate ($\omega_{\mathrm{ie}}^{\mathrm{n}}$) is notated

Figure 2.4: Euler angles defined as rotations around the axis as follows: Roll (ϕ) is the rotation around X, Pitch (θ) is the rotation around Y, and Yaw (ψ) is the rotation around Z.

as the rate of the Earth-centered Earth fixed frame (e) with respect to the inertial frame (i) resolved in the NED frame (n). Similarly, the rate of rotation of the n frame is represented as the e frame with respect to the n frame resolved in the n frame. In short, $\omega_{\text{ie}}^{\text{n}}$ represents the Earth spin rate transformed to the NED frame and $\omega_{\text{ne}}^{\text{n}}$ is the rate of change the NED frame experiences as the Earth rotates. To remove the Earth rotation rate, $\omega_{\text{ie}}^{\text{i}} = [\,0\ 0\ 7292115e{-}11\,](rad/s)$, is converted to the body frame by multiplying the previous rotation matrix $C_{\text{bn}}(k-1)$, given in (2.34),

with $\omega_{\mathrm{ie}}^{\mathrm{i}}$. The same is done for the rate experienced by the NED frame by

$$\omega_{\mathrm{en}}^{\mathrm{e}}(k) = \begin{bmatrix} \dfrac{v_E(k-1)}{r_{\mathrm{neff}}} \\ -\dfrac{v_N(k-1)}{r_{\mathrm{meff}}} \\ \dfrac{v_{\mathrm{E}}(k-1)\tan(p_L(k-1)}{r_{\mathrm{neff}}} \end{bmatrix} \tag{2.48}$$

where the latitude (p_{L}) and the velocity of the navigating body, $[\, v_{\mathrm{N}} \;\; v_{\mathrm{E}} \;\; v_{\mathrm{D}} \,]$, are combined with the effective meridian (r_{meff}) and transverse radius (r_{neff}) of the Earth to get $\omega_{\mathrm{ie}}^{\mathrm{n}}$. The meridian and transverse radii of the Earth are calculated using

$$r_{\mathrm{m}}(k) = \frac{R_0(1-e_c^2)}{(1-e_c^2\sin^2(p_{\mathrm{L}}(k)))^{3/2}} \tag{2.49}$$

and

$$r_{\mathrm{meff}}(k) = r_{\mathrm{m}} + p_{\mathrm{alt}}(k) \tag{2.50}$$

where r_m is the meridian radius of curvature, R_0 is the Earth's equatorial radius, e_c is the Earth's eccentricity, and r_{meff} is the effective meridian radius at the current altitude ($p_{\mathrm{alt}}(k)$) and latitude ($p_{\mathrm{L}}(k)$). The corrected gyroscope measurements are calculated by

$$\omega_{\mathrm{true}}(k) = \tilde{\omega} - C_{\mathrm{bn}}^T(k-1)((\omega_{\mathrm{ne}}^{\mathrm{n}}) + (\omega_{\mathrm{ie}}^{\mathrm{n}})) \tag{2.51}$$

where $\omega_{\mathrm{true}}(k)$ is the true attitude rates and $\tilde{\omega}$ are the measured gyroscope values [32]. The values are added to the previous attitude to produce the current attitude of the platform. The attitude is used in (2.34) to calculate the rotation matrix for converting from the body frame to the NED frame. The rotation matrix (C_{bn}) is used to rotate the acceleration vector to the NED frame. The transformation of the

acceleration vector can be calculated using

$$a(k) = (C_{\text{bn}}(k-1) - C_{\text{bn}}(k))(IMU_{\text{meas}})\frac{dt}{2} + E \tag{2.52}$$

where $a(k)$ is the current acceleration, IMU_{meas} are the accelerometer values in the body frame, and dt is the change in time. Lastly, E is the Earth's accelerations measured by the accelerometer. The Earth's accelerations include gravity as well as the rotation of the Earth. The current acceleration values are then used to calculate the current velocity $v(k)$. The position is then calculated from $v(k)$. For the altitude component of the position, the calculation is straightforward and can be calculated using

$$p_{\text{alt}}(k) = p_{\text{alt}}(k) + v_D(k)\frac{dt}{2} \tag{2.53}$$

where p_{alt} is the altitude component of position and $v_D(k)$ is the velocity in the down component of the NED frame. As for the latitude, the equation must take into account the curvature of the Earth. Combining (2.49) and (2.50) allows for the latitude rate of change to be calculated as

$$\dot{p_L} = \frac{v_N(k)}{r_{\text{meff}}(k-1)} + \frac{v_N(k)}{r_{\text{meff}}(k)} \tag{2.54}$$

where $v_N(k)$ is the current velocity in the north direction of the NED coordinate frame. Finally, the latitude coordinate is calculated by

$$p_L(k) = p_L(k-1) + \dot{p}_L(k)\frac{dt}{2} \tag{2.55}$$

where $p_L(k)$ is the current latitude coordinate and $p_L(k-1)$ is the latitude coordinate for the previous time step. Similarly, the calculation of the longitude value requires taking into account the curvature of the Earth. However, instead of using

the meridian radius of the Earth, the transverse curvature of the Earth must be calculated. The calculation of the transverse curvature of the Earth differs from the meridian as

$$r_n = \frac{R_0}{\sqrt{1 - e^2 \sin(p_L(k))}} \tag{2.56}$$

and the effective transverse curvature is calculated by

$$r_{\text{neff}}(k) = r_n + p_{\text{alt}}(k). \tag{2.57}$$

The rate of change in longitude is then calculated very similarly to the rate of change in latitude as shown by

$$\dot{\lambda}(k) = \frac{v_E(k)}{r_{\text{neff}}(k)\cos(p_L(k))} + \frac{v_E(k)}{r_{\text{meff}}(k)\cos(p_L(k))} \tag{2.58}$$

where $v_E(k)$ is the velocity in the east component of the NED frame. The final longitude coordinate is then calculated using $\dot{\lambda}$ and the duration of the time step as shown by

$$p_\lambda(k) = p_\lambda(k-1) + \dot{\lambda}(k)\frac{dt}{2}. \tag{2.59}$$

2.5 Summary

In this chapter, the relevant sensors utilized to obtain positional solutions is described. In addition, the challenges that are inherent to the use of each of the sensors are also described. These challenges create challenges to utilizing a single sensor to measure the position of the moving platform.

The coordinate frames used to expressed the positional solution is also detailed in this chapter. These coordinate frames provide reference points that are crucial in determining the location of a platform. The meaning of the position solution is only meaningful when expressed in these coordinate frames. Otherwise, the positional solution is only a mere set of numbers with no definition of what the position is relative to.

Lastly, the methods used in calculating a positional solution from the measurements received by IMUs is described. These methods assume the measurements are error free and does not provide any correction for the errors in the actual measurements. In the next chapter, techniques used to overcome these errors are described. The techniques utilize multiple sensors to overcome the challenges of any single sensor used in calculating a positional solution.

3 Data Fusion

In this chapter, the errors of the sensors are minimized by using a technique called data fusion. Data fusion is a modern technique that utilizes estimation theory and data from multiple sources to provide a more accurate position estimate [72]. In general, the goal is to use the best aspects of each sensor, which ideally compensate for the weak points of any other given sensor when fused. Although the technique allows for more accurate positional solutions, the technique still presents two challenges for SAR. The first challenge is producing positional solutions at the rate required to form a SAR image. The second challenge is producing positional accuracy required for SAR imaging. In this chapter interpolation techniques are presented to address the first challenge.

The integration of GPS sensors with multiple additional inputs has been used in autonomous vehicles for navigation purposes as discussed in [62, 71]. One popular method of fusing data from multiple sources is the utilization of the Kalman filter. Examples in the literature are abundant, including Nallapu et. al. [28, 45, 46, 57]. In brief, the attitude determination system in [45] executes a pre-programmed Kalman filter that combines a micro-electromechanical system (MEMS) gyroscope, a magnetometer, and an accelerometer. The Kalman filter has also been shown to provide the ability to estimate the errors of an INS system as described in [66].

The idea of data fusion is used to combine the data from the GPS and the IMU in order to produce a single position solution. It should be noted that the Kalman filter can be utilized for the fusion of multiple disparate sensors such as LIDAR and even cell towers shown by [38]. Data fusion combines the accuracy of the GPS solution as well as the faster, more stable IMU measurement resulting in a single position solution that is stable, accurate, and updated rapidly. Traditional applications of IMU and GPS fusion combine the measurements from a single IMU with

the solution from GPS. In order to increase the accuracy of the position solution, an ultra-low bias navigational grade IMU can be used to offer superior sensor performance. While a navigational grade IMU will produce the best positional estimation, these modules are typically large in size, expensive, heavy, and consume a significant amount of power. Therefore, there is a trade-off between a more accurate position solution and an increase in C-SWaP. This becomes a significant challenge for navigating bodies, such as unmanned aerial vehicles, that may require extremely accurate position solutions but are SWaP constrained.

3.1 Kalman Filter

The Kalman Filter is a method of fusing sequential measurements by utilizing the statistical errors in the system. The Kalman filter uses a model to make predictions on the system state at the next time step. The measurements of the system state are then fused with the model by estimating the joint distribution of the measurement and the predicted system state. As a result, the prediction model is improved using the joint distribution and the results are often more accurate than the measurement alone. The filter is a recursive method that utilizes the weighted average that favors measurements with more certainty. This is done utilizing the process and measurement co-variances. The Kalman filter assumes a normal Gaussian distribution of the system errors.

The Kalman filter can be used to fuse two measurements with a weighting function. The Kalman filter typically is implemented with predicting the state at a future timestep with an uncertainty value. The uncertainty in this measurement grows until a measurement is observed. The measurement is then used to correct the predictions using the weighted average. As a result, the uncertainty of the fused state estimation is decreased and the process is repeated to form a recursive process. The weighted

average of the two measurements is calculated using the prediction uncertainty divided by the sum of the prediction uncertainty and the measurement uncertainty as calculated by

$$K_n = \frac{p_{k|k-1}}{p_{k|k-1} + R_k} \quad . \tag{3.1}$$

In (3.1), K_n is the Kalman gain used to represent the weighted average between the estimation uncertainty, $p_{k|k-1}$ at the current state k given the previous state $k-1$, and the measurement uncertainty R_k. The Kalman gain is used to weigh the impact of the measurement and the predictions in the final estimation of the current state x_k. In general, the state update equation can be written as

$$x_k = x_{k-1} + K_k(y_k - x_{k-1}) \tag{3.2}$$

where x_{k-1} is the previous state estimation and y_k is the measurement of the current state. The weight of the impact of the measurement vs prediction is inversely proportional to the respective uncertainties. Additionally, the Kalman gain is bound between 0 and 1 to ensure the contribution of the measurement and the prediction does not exceed the reported value. For example, if the Kalman gain is greater than one the weight on the prediction is negative and introduces error if the prediction is estimating positive values. Similarly, the weight on the measurement is greater than 1 and the measurement becomes amplified and errors can be introduced by a false amplification. This becomes obvious when expanding the equation in (3.2), to

$$x_k = (1 - K_k)x_{k-1} + K_k y_k \quad . \tag{3.3}$$

As a result, low uncertainty, or high confidence, in the measurements results in a high K_k causing the weight on x_{k-1} to be low meaning the measurement contributes more to the final estimation of the current state. This logically makes sense as

the high confidence in the measurement should result in the final estimation being closer to the measurement. Similarly, high uncertainty, or low confidence, in the measurement results in a high weight $(1 - K_k)$ in the state prediction. Logically, this means that the prediction should contribute more to the final estimation if the received measurement is highly uncertain.

The Kalman filter also allows for the estimation of uncertainty using the Kalman gain. The concept is similar to the state estimation where the uncertainty at state k can be estimated using

$$p_k = (1 - K_k)p_{k|k-1} \quad . \tag{3.4}$$

The rate of convergence for the uncertainty is controlled by the Kalman gain in this case. High confidence in the measurement value equates to a low $(1 - K_k)$ term which results in a large decrease in uncertainty based on the previously estimated uncertainty value. Conversely, low confidence in the measurement value results in a high $(1 - k_k)$ which means the change in uncertainty is decreased by a small increment. Using these relationships the Kalman filter can adjust the uncertainty of the estimation of the current state based on the covariance matrices of the measurement and predictions. Intuitively, the concept makes sense as more measurements are observed the confidence in the estimation should increase which equates to a lower uncertainty value. This allows for the filter to converge to true values as the filter recursively makes more estimates.

For system states that are more than 1 dimension, the Kalman filter can be extrapolated to multiple dimensions by converting the equations to handle matrices. For example, estimating the location of a moving vehicle is often expressed in 3 dimensions. In this scenario, the state X_k in (3.3) becomes a vector containing the X, Y, and Z coordinate of the vehicle's location. Furthermore, the dimension of the vehicle state can be further extended to contain velocity and acceleration converting

X_k into

$$\mathbf{x_k} = \begin{bmatrix} X \\ Y \\ Z \\ V_x \\ V_y \\ V_z \\ a_x \\ a_y \\ a_z \end{bmatrix} \tag{3.5}$$

where X, Y, and Z are the location coordinates, V_x, V_y, and V_z are the velocity in each coordinate axis and a_x, a_y, and a_z are the acceleration in each coordinate axis. Similarly, the covariance matrix p_k in (3.4) is converted to

$$\mathbf{p_k} = \begin{pmatrix} COV(x,x) & COV(x,y) & COV(x,z) & COV(x,V_x) & COV(x,V_y) & COV(x,V_z) & COV(x,a_x) & COV(x,a_y) & COV(x,a_z) \\ COV(y,x) & COV(y,y) & COV(y,z) & COV(y,V_x) & COV(y,V_y) & COV(y,V_z) & COV(y,a_x) & COV(y,a_y) & COV(y,a_z) \\ COV(z,x) & COV(z,y) & COV(z,z) & COV(z,V_x) & COV(z,V_y) & COV(z,V_z) & COV(z,a_x) & COV(z,a_y) & COV(z,a_z) \\ COV(V_x,x) & COV(V_x,y) & COV(V_x,z) & COV(V_x,V_x) & COV(V_x,V_y) & COV(V_x,V_z) & COV(V_x,a_x) & COV(V_x,a_y) & COV(V_x,a_z) \\ COV(V_y,x) & COV(V_y,y) & COV(V_y,z) & COV(V_y,V_x) & COV(V_y,V_y) & COV(V_y,V_z) & COV(V_y,a_x) & COV(V_y,a_y) & COV(V_y,a_z) \\ COV(V_z,x) & COV(V_z,y) & COV(V_z,z) & COV(V_z,V_x) & COV(V_z,V_y) & COV(V_z,V_z) & COV(V_z,a_x) & COV(V_z,a_y) & COV(V_z,a_z) \\ COV(a_x,x) & COV(a_x,y) & COV(a_x,z) & COV(a_x,V_x) & COV(a_x,V_y) & COV(a_x,V_z) & COV(a_x,a_x) & COV(a_x,a_y) & COV(a_x,a_z) \\ COV(a_y,x) & COV(a_y,y) & COV(a_y,z) & COV(a_y,V_x) & COV(a_y,V_y) & COV(a_y,V_z) & COV(a_y,a_x) & COV(a_y,a_y) & COV(a_y,a_z) \\ COV(a_z,x) & COV(a_z,y) & COV(a_z,z) & COV(a_z,V_x) & COV(a_z,V_y) & COV(a_z,V_z) & COV(a_z,a_x) & COV(a_z,a_y) & COV(a_z,a_z) \end{pmatrix} \tag{3.6}$$

The diagonal of the matrix in (3.6) simplifies to the variance of the state parameter as the covariance of a parameter with itself is the variance. The covariance between two-state parameters can be calculated using

$$COV(\mathbf{X}, \mathbf{Y}) = E[(\mathbf{X} - E[\mathbf{X}])(Y - E[\mathbf{Y}])] \tag{3.7}$$

where E is the expected value operator. The covariance of a variable with itself is

simplified to

$$COV(\mathbf{X}, \mathbf{X}) = E[(\mathbf{X} - E[\mathbf{X}])^2] = \sigma_x^2 \tag{3.8}$$

These concepts are fundamental to the Kalman filter as it is implemented in navigation applications. As result, the Kalman filter utilizes several matrices to model the state prediction and the covariance of the state parameters. In inertial navigation applications, the position is the state being predicted using a motion model and the measured acceleration from the IMU. The predicted position is then fused with the GPS measurement using the Kalman gain. An example of the uncertainty of the inputs into the Kalman filter is shown in Fig. 3.1. The figure illustrates the uncertainties and errors that are associated with the predicted location and the measured GPS position. The blue dots represent the possible GPS measurements that could be provided. Similarly, the orange shows the possible predictions provided from using a motion model and the IMU measurements. In this case, the GPS position provides a more precise measurement relative to the predicted location. This can be seen by the relative size of the GPS possible values compared to the size of the predicted values. In 3.1 precision of the measurement is proportional to the size of the point cloud and the smaller the point cloud means the more precise the measurement is. Regardless, both the predicted state and the GPS measurements are erroneous as indicated by the center of these point clouds being different from the true value.

Breaking the point clouds into a single dimension, the probability of the measurements can be represented as a histogram. The histogram shows the concentration or density of the point cloud and the width of the histogram is proportional to the uncertainty of the measurement. In Fig. 3.2, the histograms for the point cloud in 3.1 are depicted. It can be seen that the uncertainty of the GPS is less than the uncertainty of the predictions as indicated by the width of the histograms.

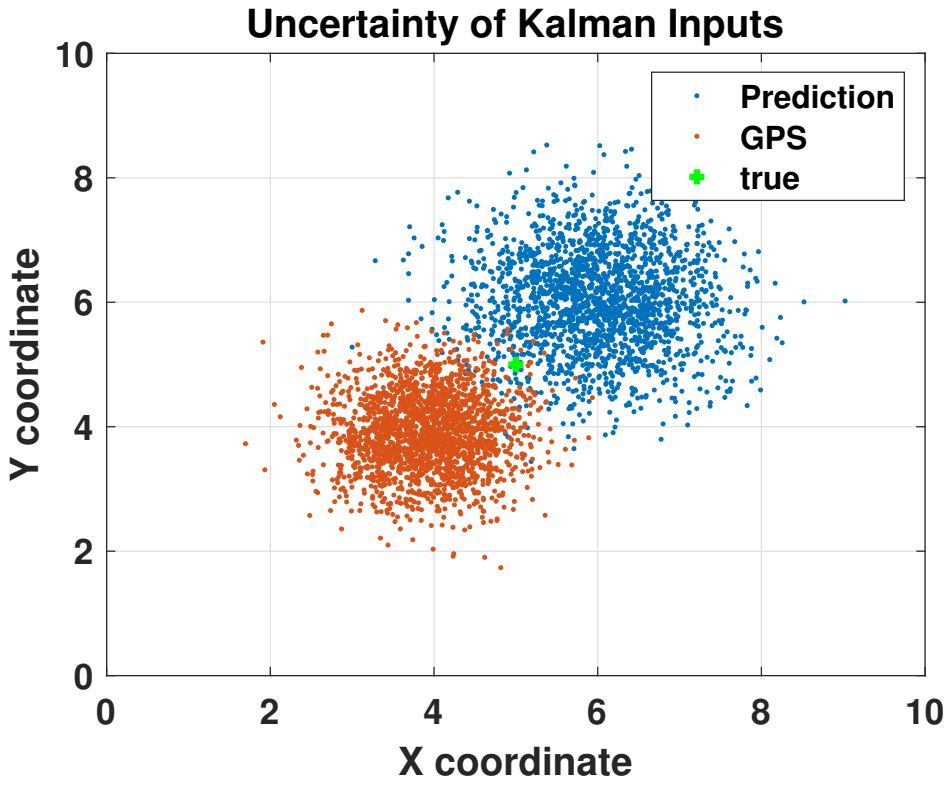

Figure 3.1: Image of the uncertainty of the inputs of the Kalman filter. The true X, Y coordinate is indicated as the green cross. The possible GPS measurements are shown in orange and the possible predicted values are shown in blue.

Generically, the Kalman filter recursively calculates the weighted average between the predicted positions, calculated from the IMU measurements, and the measured position from the GPS. The Kalman estimation of the final state can be seen in Fig. 3.2, where the estimate shown in green provides a more precise measurement. The increase in precision can be attributed to the Kalman gain causing the uncertainty to converge as shown in (3.4).

Implementation of the Kalman filter requires a prediction of the system position that is then fused with the measurement. The prediction requires the previously known position and the acceleration measured from the IMU. In addition, the covariance of the system state is also predicted according to the prediction model.

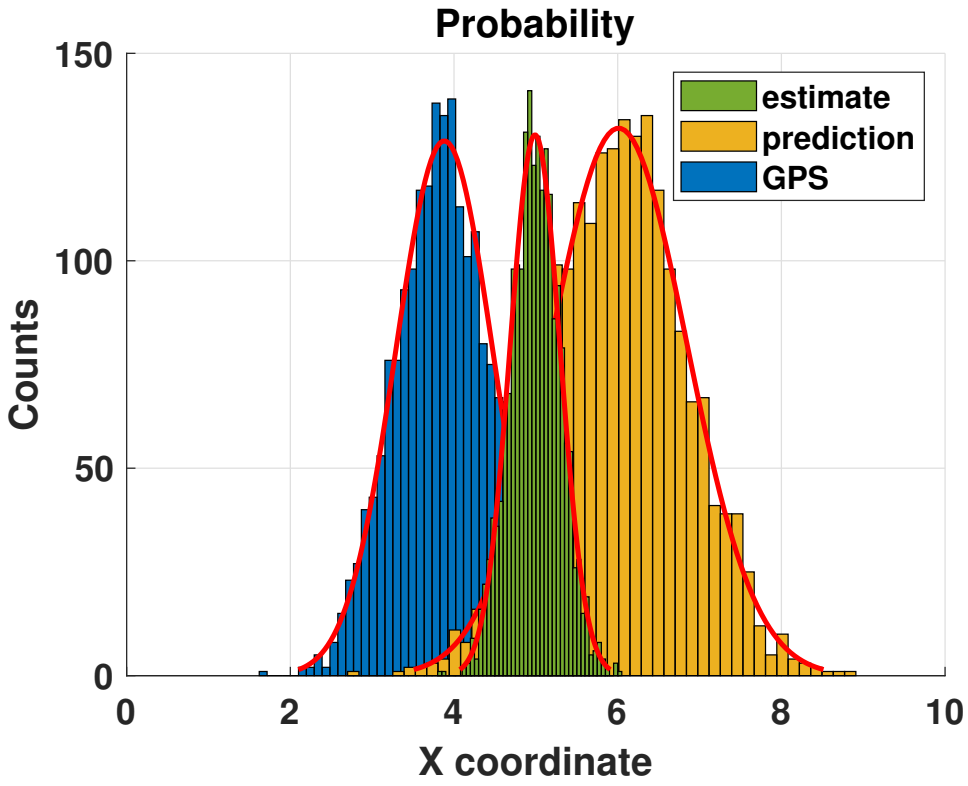

Figure 3.2: Probability density of a 1-dimensional Kalman fusion. The yellow histogram is the probability density of the prediction of the X coordinate. The blue histogram is the probability density of the GPS measurement. Lastly, the green histogram is the probability density of the final estimate of the X coordinate from the Kalman filter.

The Kalman gain is then calculated using the measurement covariance and the predicted state covariance. Lastly, the final state estimation is calculated using the calculated Kalman gain and the final state covariance is updated. Implementation of the Kalman filter is broken into two stages: the prediction stage and the update stage.

Prediction In the prediction stage, a prediction of where the measurement should be is calculated using a mathematical model of the system. In addition, given the error covariance of the system, the Kalman filter will also predict the covariance of

the predicted measurement. The result of the prediction stage is an expected value and the variance of the measurement is calculated. The equation for the prediction step of the Kalman filter is shown in (3.9),

$$\hat{\mathbf{X}}_{\mathbf{k}} = \mathbf{F}\mathbf{x}_{\mathbf{k-1}} + \mathbf{B}\mathbf{u}_{\mathbf{k}} \tag{3.9}$$

where $\hat{\mathbf{X}}_{\mathbf{k}}$ is the position estimated by the mathematical model, $\mathbf{F}$ is the state transition matrix, $\mathbf{x}_{\mathbf{k-1}}$ is the estimation in the previous time step, $\mathbf{B}$ is the control vector, and $\mathbf{u}_{\mathbf{k}}$ is the system influence matrix. For example, a GPS and IMU implementation can be modeled by (2.46) and (2.47) for position and velocity respectively. In order to represent the GPS and IMU system in the Kalman filter, (3.9) will need to be expanded to contain position velocity in the x, y, and z dimensions in the Earth-centered inertial (ECI) frame. Equations (2.46) and (2.47) can be transformed into the following form to match the form in (3.9). The resulting form of the Kalman filter prediction is shown in (3.10).

$$\begin{bmatrix} p_k \\ v_k \end{bmatrix} = \begin{bmatrix} 1 & \delta t \\ 0 & 1 \end{bmatrix} \begin{bmatrix} p_{k-1} \\ v_{k-1} \end{bmatrix} + \begin{bmatrix} \frac{1}{2}\delta t^2 \\ \delta t \end{bmatrix} \begin{bmatrix} a_k \end{bmatrix} \tag{3.10}$$

From equations (3.9) and (3.10), the following can be defined $\hat{\mathbf{X}}_{\mathbf{k}} = \left[\begin{smallmatrix} p_k \\ v_k \end{smallmatrix}\right]$, $\mathbf{F} = \left[\begin{smallmatrix} 1 & \delta t \\ 0 & 1 \end{smallmatrix}\right]$, $\mathbf{x}_{\mathbf{k-1}} = \left[\begin{smallmatrix} p_{k-1} \\ v_{k-1} \end{smallmatrix}\right]$, and $\mathbf{B} = \left[\begin{smallmatrix} 0.5\delta t^2 \\ \delta t \end{smallmatrix}\right]$. The Kalman filter can now take acceleration ($\mathbf{a}_{\mathbf{k}}$) measurements from the IMU and estimate the next position by taking the velocity and position from the previous estimate or time step. In addition to the prediction of the expected value of the measurement, the prediction step also predicts the new covariance based on the state transition matrix given. The equation for the prediction of the covariance matrix is given by (3.11)

$$\mathbf{P}_{\mathbf{k}} = \mathbf{F}\mathbf{P}_{\mathbf{k-1}}\mathbf{F}^T + \mathbf{Q}_{\mathbf{k}} \tag{3.11}$$

where $\mathbf{P_k}$ is the new covariance, and $\mathbf{P_{k-1}}$ is the covariance of the previous time step. In equation (3.11), $\mathbf{P_k}$ and $\mathbf{P_{k-1}}$ are the covariances of the $\hat{\mathbf{X}}_\mathbf{k}$ and $\mathbf{x_{k-1}}$ in (3.9) respectively and $\mathbf{Q_k}$ is the process noise.

Update In the update step, the Kalman filter takes the measurement produced by the sensor and fuses it with the estimated measurement. The fusion happens by first calculating the covariance of the measured value based on the specified noise of the sensor. The Kalman filter then determines the probability that the measurement from the sensor is the truth value. The final value produced by the Kalman filter is the estimation from the math model corrected by the sensor compensated by a factor of confidence known as the Kalman gain. The factor of confidence is calculated based on the mean and variance of the measurement. The equations to calculate the update step are shown in (3.12) through (3.15).

$$\mathbf{S_k} = \mathbf{H_k}\mathbf{P_{k-1}}\mathbf{H_k}^T + \mathbf{R_k} \tag{3.12}$$

$$\mathbf{K_k} = \hat{\mathbf{P}}_\mathbf{k}\mathbf{H_k}^T(\mathbf{S_k})^{-1} \tag{3.13}$$

$$\mathbf{X_k} = \hat{\mathbf{X}}_\mathbf{k} + \mathbf{K_k}(\mathbf{y_k} - \mathbf{H_k}\hat{\mathbf{X}}_\mathbf{k}) \tag{3.14}$$

$$\mathbf{P_k} = \hat{\mathbf{P}}_\mathbf{k} - \mathbf{K_k}\mathbf{H_k}\hat{\mathbf{P}}_\mathbf{k} \tag{3.15}$$

Equation (3.12) defines $\mathbf{H_k}$ as the measurement matrix and $\mathbf{R_k}$ as the measurement noise variance. For the IMU and GPS application the measurement matrix $\mathbf{H_k} = \begin{bmatrix} 1 & 0 \end{bmatrix}$ since the measurement given to the Kalman filter is the GPS position measurement and does not include velocity. In addition, $\hat{\mathbf{P}}_\mathbf{k}$ is the estimation of the covariance calculated in the prediction step. $\hat{\mathbf{X}}_\mathbf{k}$ is the predicted measurement calculated in the prediction step. Equation (3.13) is the confidence factor, also known as the Kalman gain, that determines how much of the measurement is incorporated

into the final estimate of the Kalman filter. In equation (3.14), the final corrected estimate is calculated by adding the difference of the measurement $\mathbf{y_k}$ and the estimate calculated in the prediction step, scaled by the Kalman gain. The final result contains a combination of the data obtained by the IMU and the GPS calculated by the Kalman filter. Lastly, (3.15) calculates the covariance of the fused result given the Kalman gain and the covariance estimated by the prediction step.

The results of the Kalman filter can be fed back into the algorithm as the estimate for the previous time step ($\mathbf{x_{k-1}}$) allowing the Kalman algorithm to be executed recursively to produce a fusion of two sensors at every time step. In the GPS and IMU application, the Kalman filter algorithm was used only when a GPS measurement was present. For instance, the GPS position is fused with the most recent estimated position to provide a more precise position estimate. In between the GPS position updates, the prediction state of the Kalman filter was calculated for every data point of the IMU. As the GPS measurement became available, the fusion via the update step of the Kalman filter was utilized to incorporate the GPS values into the new prediction. The product of the Kalman filter fusion created an aided Inertial Navigation System (INS) solution capable of producing position estimations when the GPS sensor is unavailable.

It should be noted that the Kalman filter is limited to linear systems with White Gaussian noise. In order to address non-linear systems, different flavors of the Kalman filter have been presented in literature [41, 42, 47, 68]. The most common flavor are the extended Kalman filter and unscented Kalman filter which addresses the linear systems limitation of the Kalman filter[34, 56, 58, 69, 70]. The particle filter is shown to have the capabilities of outperforming the Kalman filter in many applications [3]. The particle filter also has different flavors such as the unscented particle filter [48] to address different limitations of multiple model filters and also

show the particle filter can outperform the Kalman filter. In literature the particle filter has been shown to provide better results than the flavors of Kalman filter [4]. For this reason the flavors of the Kalman filter are not analyzed in this dissertation.

3.2 Particle Filter

The particle filter is another method of fusing data measurements and has drawn increasing attention during recent years because of its superior ability to deal with processes that have non-linear models and contain non-Gaussian noise sources [3, 17, 21, 22, 77]. The method has been proven to produce superior results in the application of fusing IMU and GPS measurements [9]. The navigation application does not guarantee the noise sources are non-linear and non-Gaussian in nature. The particle filter is a sequential Monte Carlo method based on Bayesian theory, for instance [14, 22, 23, 51] and others. The idea is to calculate several possible outcomes for each state of the system. The number of possible outcomes is represented as a cloud of particles. At each state, every value of the particle cloud is propagated to the next state. In doing so, a Monte Carlo method is sequentially implemented at each state. The particle cloud is meant to represent the distribution of the estimated system state. In propagating the particle cloud, the posterior probability distribution of the system state is estimated. The state estimation is then done by taking the sample mean of the particle cloud as the sample representation of the posterior distribution. The posterior distribution is then recalculated given a new measurement of the system state. The recalculation of the posterior distribution is done using a concept known as *resampling*. The concept of resampling requires each sample of the particle cloud to be weighted with an importance value. The importance value represents how likely the particle is representative of the true posterior distribution. The particle cloud is then resampled where the particles with higher weights are drawn more often to replace the unlikely particles in the cloud. As a result, the new particle cloud is more representative of the true posterior distribution of the system state. As more measurements are observed, the representation of the posterior distribution becomes increasingly accurate. As a result, the final estimation

of the system state is estimated from a more accurate probability distribution which directly translates to a more accurate system state estimation.

The particle filter estimates the system state from a representation of the posterior distribution. The representation is not restricted to any one distribution and allows for the filter to be flexible and accurate regardless of the true distribution. In addition, particle filters are capable of handling large systems as the filter does not require the covariance of each system state to be estimated and modeled. This is a byproduct of the particle filter performing state estimations from the posterior distribution directly. As a result, the estimations are not altered given the covariance of the measurements. As shown by (3.6) the covariance matrix increases with the number of state variables being estimated. Particle filters can be applied in remote sensing applications to perform tasks such as object and target tracking [6, 79, 81], and have been used to fuse data from multiple sensors to track target location over a sensor network that covers an area of interest [80]. Moreover, particle filters can be used in conjunction with inertial sensors for motion tracking applications as described in [65] where fused data from visual sensors and an inertial sensor are used to track the motion of a robotic arm. Lastly, the authors in [7] implemented a hybrid approach using a particle filter and Kalman filter to produce accurate navigation solutions during GPS outages.

While the particle filter can be used to fuse the GPS and IMU data to provide a highly-precise (high-frequency applicable) and long-term PNT solution, the update rate of the said data will be limited by the highest PRF sensor.

Consider a system where position (p_k) and velocity (v_k) at state k are modeled by two non-linear functions given by

$$p_k = F(x) + Q_k \tag{3.16}$$

and

$$v_k = G(x) + R_k \ , \tag{3.17}$$

where $F(x)$ and $G(x)$ are non-linear functions, Q_k is the process noise, and R_k is the measurement noise. Applying Bayes' theorem, given by

$$P(A|B) = \frac{P(B|A)P(A)}{P(B)} \tag{3.18}$$

in conjunction with the law of probability given by

$$P(B) = \sum P(B|A)P(A) \tag{3.19}$$

, shows that Bayes' theorem may be extended to represent the posterior distribution by

$$P(A|B) = \frac{P(B|A)P(A)}{\sum_{\mathrm{i=1}}^{i=N} P(B|A)P(A)} \ . \tag{3.20}$$

Combining (3.16), (3.17), and (3.20) allows for the posterior distribution of the non-linear system be modeled as

$$P(\mathbf{p}_{0:\mathrm{k}}|\mathbf{v}_{1:\mathrm{k}}) = \frac{P(\mathbf{v}_{1:\mathrm{k}}|\mathbf{p}_{0:\mathrm{k}})P(\mathbf{p}_{0:\mathrm{k}})}{\sum_{\mathrm{i=1}}^{i=N} P(\mathbf{v}_{1:\mathrm{k}}|\mathbf{p}_{0:\mathrm{k}})P(\mathbf{p}_{0:\mathrm{k}})} \ . \tag{3.21}$$

Particle filters utilize the importance sampling concept, as discussed previously in [20], where each particle in the cloud is assigned a weight, as our team has successfully demonstrated in the past [76, 81–83]. The weights need to be normalized when used in the importance sampling which can be accomplished using

$$w_{\mathrm{k}}^i = w_{\mathrm{k-1}}^i \frac{P(\mathbf{v}_k|\mathbf{p}_k^i)P(\mathbf{p}_k^i|\mathbf{p}_{\mathrm{k-1}}^i)}{\rho(\mathbf{p}_k^i|\mathbf{p}_{0:\mathrm{k}}^i, \mathbf{v}_{1:\mathrm{k}})} \tag{3.22}$$

where w_{k}^i is the weight for sample i and $\rho(\mathbf{p}_k^i|\mathbf{p}_{0:\mathrm{k}}^i, \mathbf{v}_{1:\mathrm{k}})$ is the proposal probability

function. The proposal probability function is the joint probability of the position at state k, given the previous positions and velocity. As a result, the calculated weights are normalized to represent a probability bound by the proposal probability function. The weights are used to estimate the posterior distribution of the estimated position and velocity. Lastly, the posterior particles for position and velocity are drawn from the posterior distribution of position and velocity, respectively. An implementation and derivation of the particle filter are described in [78].

The particle filter is broken down into multiple steps. The first step initializes a particle cloud with an expected value equal to the initial position of the platform. The second step moves the point cloud by the motion model of the system described by (2.53), (2.55), and (2.59). The third step re-samples the values in the point cloud and the last step produces the position estimate by calculating the expected value of the re-sampled point cloud. The re-sampling step is required to remove samples in the point cloud that are the least likely to be the true position while maintaining an appropriate number of particles in the point cloud. An example of the effects of re-sampling is shown in Fig, 3.3. Removing samples with the least likelihood of being the true position allows for the particle filter to converge to the true position. As a result, the particle cloud begins to converge the true value. In Fig.3.3, the orange cloud is fed forward to the next re-sampling iteration to be re-sampled given a new measured value. In addition, the measurements produced should be within the black ring representing the measurement uncertainty. It can be seen that the estimation from the particle filter increases with accuracy as more measurements are provided and the particle cloud is re-sampled repeatedly. However, If the re-sampling technique is not effectively implemented, the particle cloud could degenerate as described in [50], meaning the particle cloud will produce erroneous predictions. The degeneration is caused by the loss of diversity in the particle

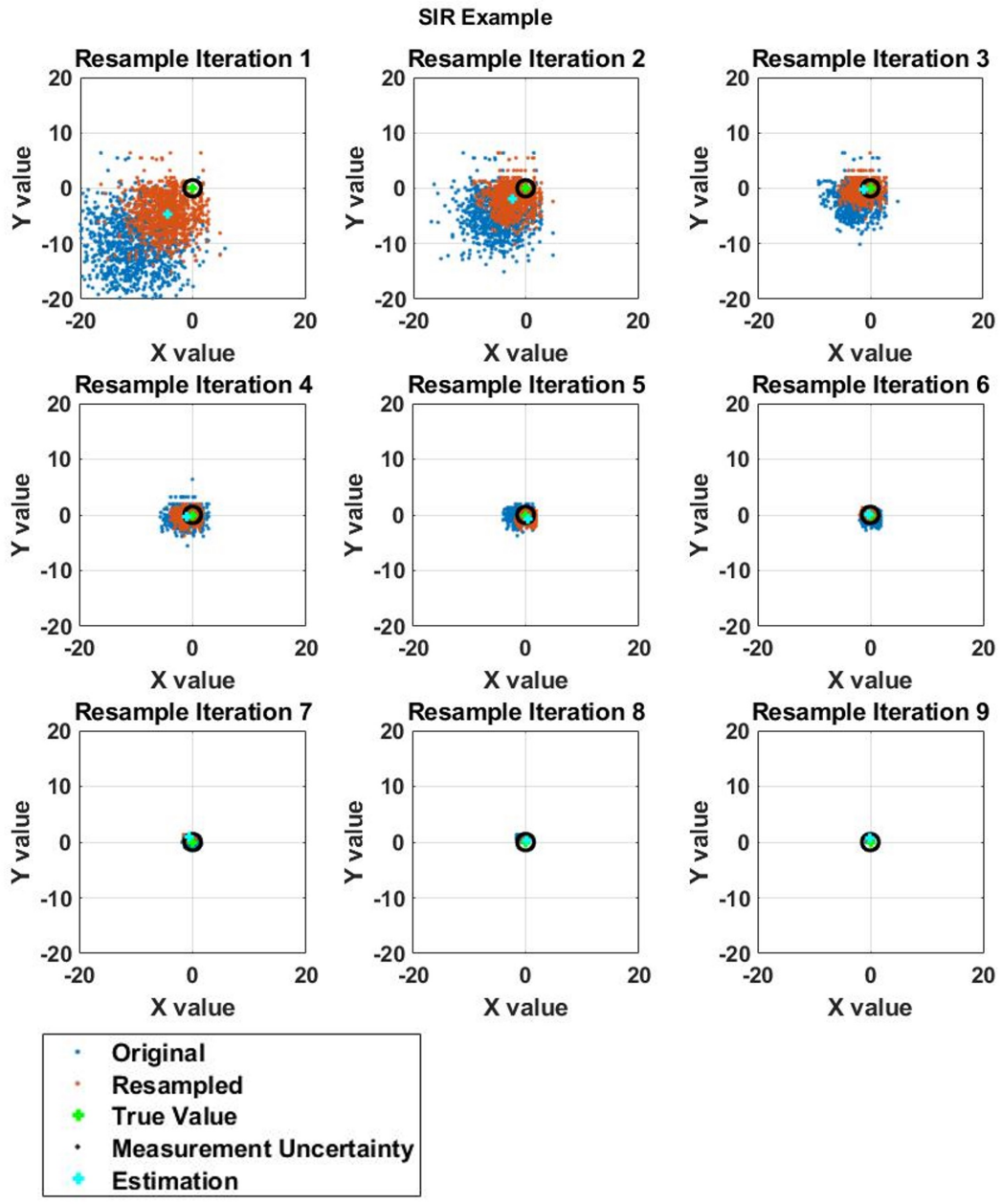

Figure 3.3: The effects of re-sampling. The blue cloud shows the particle cloud before the re-sampling is done. the orange cloud shows the re-sampled particles. The true value of the state being estimated is shown by the green cross and the uncertainty of the measurements is shown by the black ring. Lastly, the particle filter estimation is shown by the cyan cross.

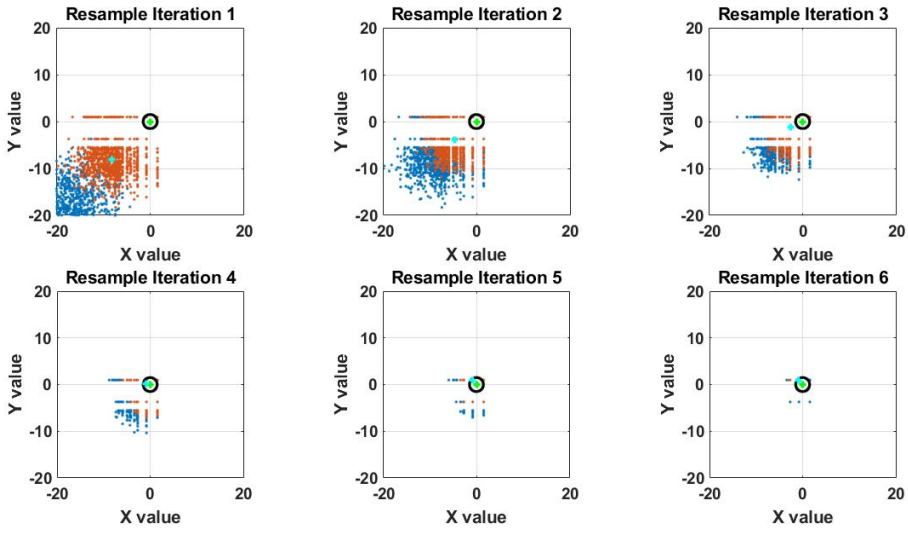

Figure 3.4: The degenerative effects of re-sampling. The colors represent the same values as described by Fig. 3.3. It can be seen that the diversity of the particle cloud is lost resulting in an erroneous estimate from the particle filter.

cloud. This happens when the number of likely particles diminishes. As a result, the particle cloud becomes multiple copies of the same value in the worst case. The particle state estimate becomes the value of the particle which can be erroneous if the particle cloud had not converged to the true value. An example of this is shown in Fig. 3.4 where it can be seen that the diversity of the particle cloud quickly diminishes due to re-sampling. In Iteration 6, the particle cloud has been reduced to multiple copies of a few samples. As a result, the particle estimation is erroneous as the particles are poorly representing the posterior distribution causing the state estimation to be inaccurate. However, re-sampling introduces variance into the filter results and in practice, it is best to limit the number of times a particle cloud is re-sampled[75].

Particle filters allow for a distribution to be proposed in providing a position estimation. Assuming the samples within the particle cloud are independent, the expected value of the particle cloud will be an unbiased estimate of position. Fur-

thermore, the law of large numbers shows that the position estimates from the particle filter will converge to the true position [51]. Using particle filters, the posterior position estimate can be calculated using

$$\mathbf{p_k} = \frac{1}{N}\sum_{\mathrm{i}=1}^{N}\mathbf{F}(\mathbf{x}^i)\omega(\mathbf{x}^i) \ , \tag{3.23}$$

where p_k is the posterior distribution at time k, $\omega(\mathbf{x}^i) = \frac{f_x(\mathbf{x})}{q(\mathbf{x})}$ and $f_x(x)$ is the true probability distribution function (PDF) of the position measurements and $q(\mathbf{x})$ is the PDF of the particle cloud. This feature allows for the particle filter to use and estimate distributions that are not Gaussian and is the distinct advantage over the Kalman filter. An example of the re-sampling using a uniform distribution is shown in Fig. 3.5 where the proposal distribution is a uniform distribution. Since the weights of each particle are calculated based on the proposal distribution, the posterior distribution represented by the particles is also uniform. In this way, particle filters are capable of modeling multi-model distributions and can provide the a set of most likely outcomes of the estimated state. This phenomenon is leveraged in simultaneous location and mapping applications (SLAM) as demonstrated in [10].

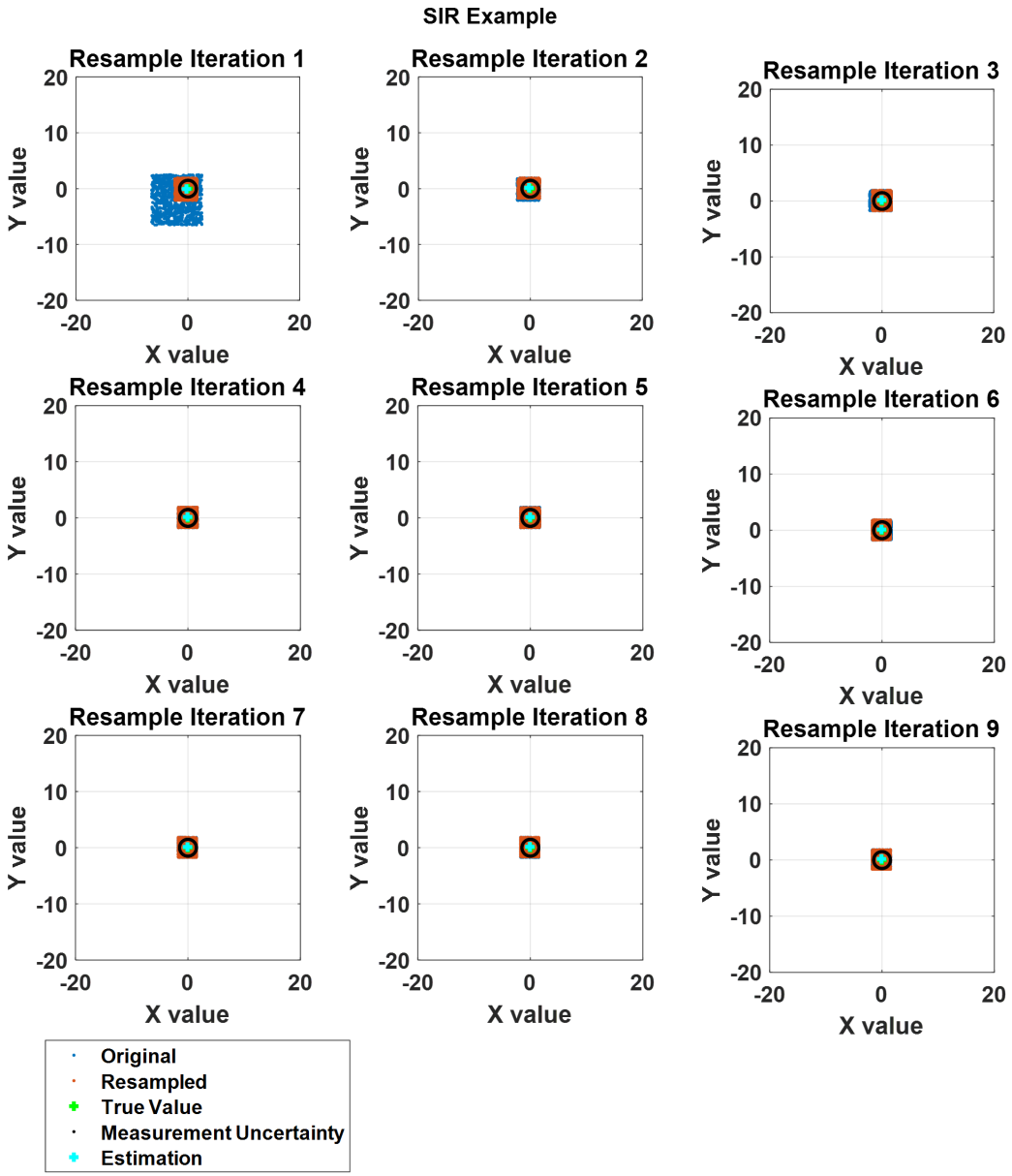

Figure 3.5: The re-sampling technique using a uniform distribution. The colors represent the same values as described by Fig. 3.3. It can be seen that the distribution of the particle cloud is a 2-dimensional uniform distribution.

3.3 Interpolation

As previously mentioned, in SAR applications, it is ideal for the update rate of the PNT data to match the PRF of the radar system such that the relative position of the moving platform to some reference point of the observed scene could be precisely known on a pulse-by-pulse basis. As reported by Llaveria et al. in [40], data coming from gyroscopes can be linearly interpolated to improve the temporal resolution as long as the change in angular velocity of the platform is minimal at each time step. As a result, the improvement in image quality was always better when the interpolation was utilized. For airborne SAR imaging applications, the goal is to minimize angular velocity (i.e. keep the platform wings parallel to the Earth) and fly straight at a constant altitude. Thus, it is hypothesized that this temporally interpolated technique can be applied to the IMU data, which utilizes a series of gyroscope and accelerometer sensors to produce its position estimate and increase overall image quality.

The data was processed using two methods; the first is aiding without the Kalman filter. The aiding method involved predicting the next location based on the acceleration values in each direction. When a GPS position becomes available, the current position is set equal to the GPS value at the time step. The method used provided a sawtooth-like estimation. The sawtooth pattern is caused by the uncertainty in the IMU data contributing to the estimated position. The position is then aided with the GPS position which corrects for the uncertainty in the IMU data. The results of the aided algorithm are displayed in Fig. 3.6. In order to show the resulting accuracy, Fig. 3.6 is zoomed to a subset of the route taken. The results show that the algorithm predicts position given the acceleration measured by the IMU. However, the variance of the position estimated is large due to the sawtooth pattern of the estimated patterns. The variance being large shows that the system is uncertain that

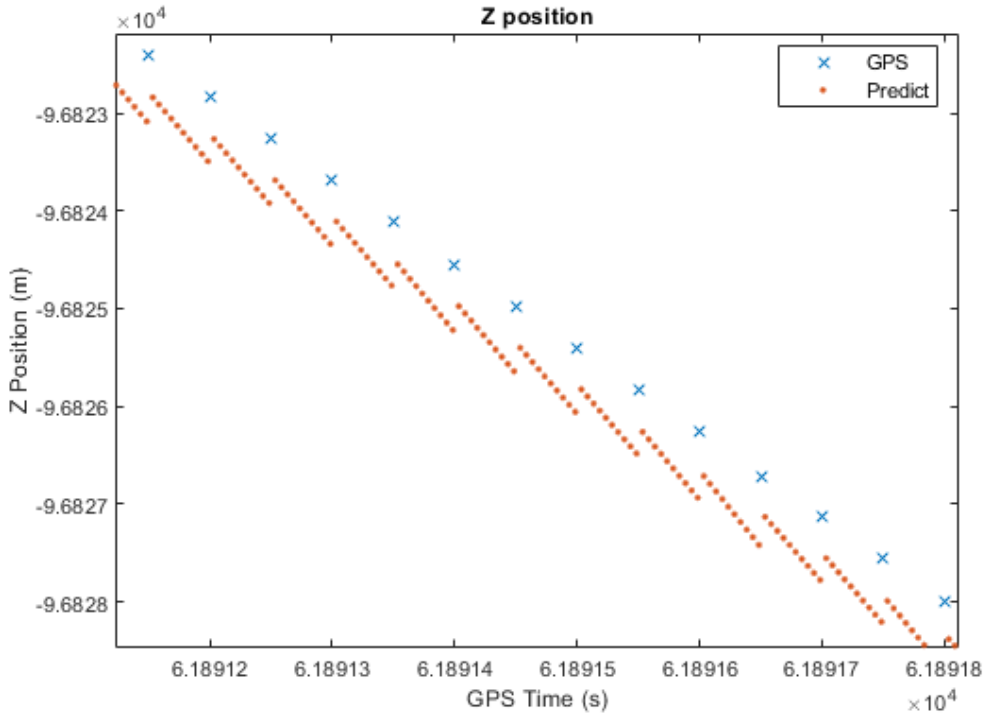

Figure 3.6: Results of the aided algorithm without the Kalman filter

the position estimated is the true position. In addition, the difference between the estimated position before the correction and the value of the GPS position used for correction is significantly large which creates the sawtooth pattern. It is preferred to have a smoother position pattern from one GPS time to the next. In addition, the position estimate needs to be consistent and the drift in error must be minimized in order to reduce the variance or uncertainty of the position estimate. The results of the aided method without the Kalman filter are already drifting at 0.05 seconds or 20 Hz, meaning the algorithm is not suitable for having large outages of the GPS sensor. The Kalman filter is needed to improve the drift rate of the aided IMU and GPS. The results of the Kalman filter fusion algorithm are shown in Fig. 3.7.

It can be seen that compared to the aided method the Kalman filter smoothed the estimated position pattern and controls the drift of the IMU sensor estimations. The

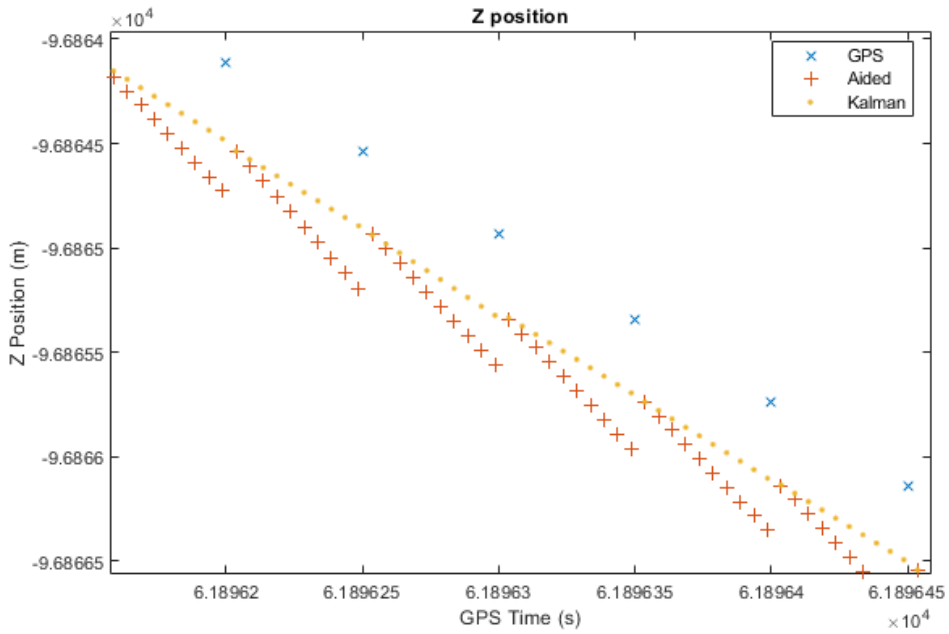

Figure 3.7: Results of the aided algorithm with the Kalman filter

position estimates using the Kalman filter do not provide drastic corrections and do not produce the sawtooth pattern of the position estimates. The estimated positions from both the aided without the Kalman filter and the Kalman filter method have a slight bias. The algorithms implemented did not currently account for biases. The final result with the GPS solution, aided method, and Kalman filter is shown in Fig. 3.8. The estimated results of the whole route traveled show that the algorithms are all very similar in the position estimate. More details on the issues that arise from interpolation are detailed by [63].

In the NovAtel SPAN system, the GPS is updated at a rate of 20 Hz whereas the IMU is updated at a faster rate of 200 Hz; therefore, on average, ten IMU measurements are made between any two GPS position measurements. The IMU measurements provide acceleration of the navigation body in the Cartesian coordinate system where the origin of this system is centered on the navigating body's

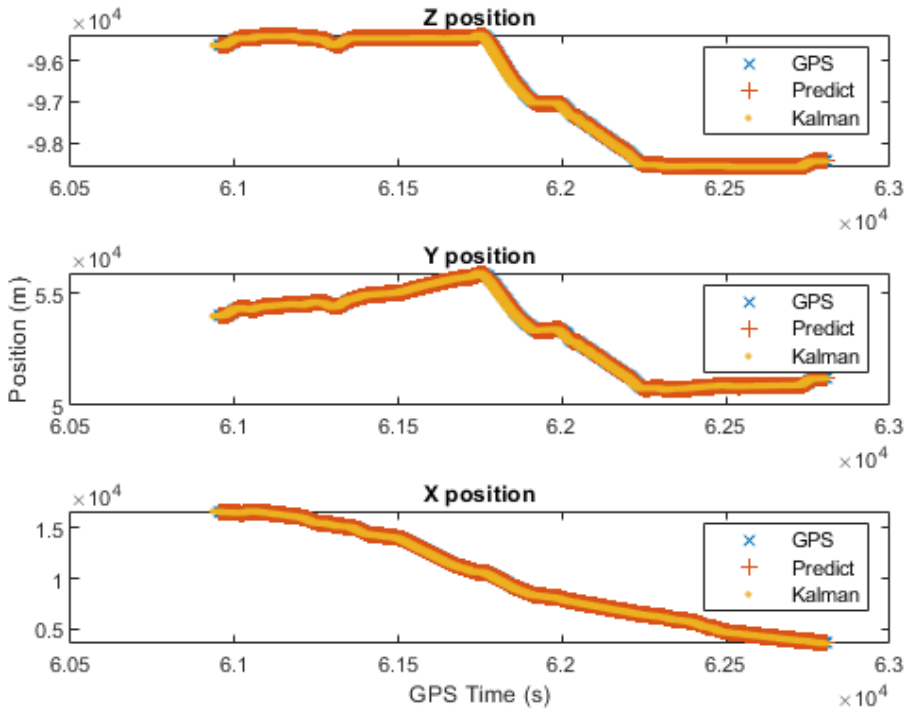

Figure 3.8: Results of the GPS positions and the results of both algorithms

center of gravity. The position and velocity of the navigating body can be estimated from the IMU measurements using the system model in (3.10).

As previously mentioned, radar applications require a faster rate of producing accurate data measurements. Radars detect moving targets by utilizing a fast sampling rate to increase velocity resolution. Typically, radars sample at rates on the order of kHz to achieve the desired velocity resolution. One method of increasing the resolution of the position estimates provided by the INS system is to interpolate the time vector used to estimate the position updates. The interpolated time vector is then used to estimate positions more frequently. This proposed method up-samples the position solutions, given by the INS, by applying a linear interpolation in time to produce time epochs at the desired resolution. In this dissertation, two estimation methods are implemented that utilize an up-sampled time vector to achieve finer

resolution position estimates as discussed in the next two sub-sections.

3.4 Kalman Filter Interpolation

The Kalman filter implemented in this paper uses the interpolated time vector and the most recent position, velocity, and acceleration to model the position at each time step. The Kalman filter then estimates the position at each up-sampled time epoch using the model described in (3.10) and fuses the estimates with the GPS sensor provided solutions. The model estimates are used to provide position estimates at a more frequent rate while the fusion technique minimizes the drift of the model estimates. The result is position updates that occur on the specified time resolution.

The algorithm uses the latest acceleration data from the IMU with the previous position, p_{k-1}, to estimate the new position, p_k. The last known IMU measurement is used to predict the next position until a new IMU measurement is provided. The algorithm detects if a new measurement is available by comparing the next time epoch (k) to the timestamp of the latest acquired IMU data. The algorithm continues to predict positions during the up-sampled time epochs. The IMU measurements are only updated when the up-sampled time epoch aligns with the next IMU measurement's timestamp. The estimated position is fused via the Kalman filter with GPS to produce a position update accurate with GPS data. The flow chart for the described algorithm is shown in Fig. 3.9.

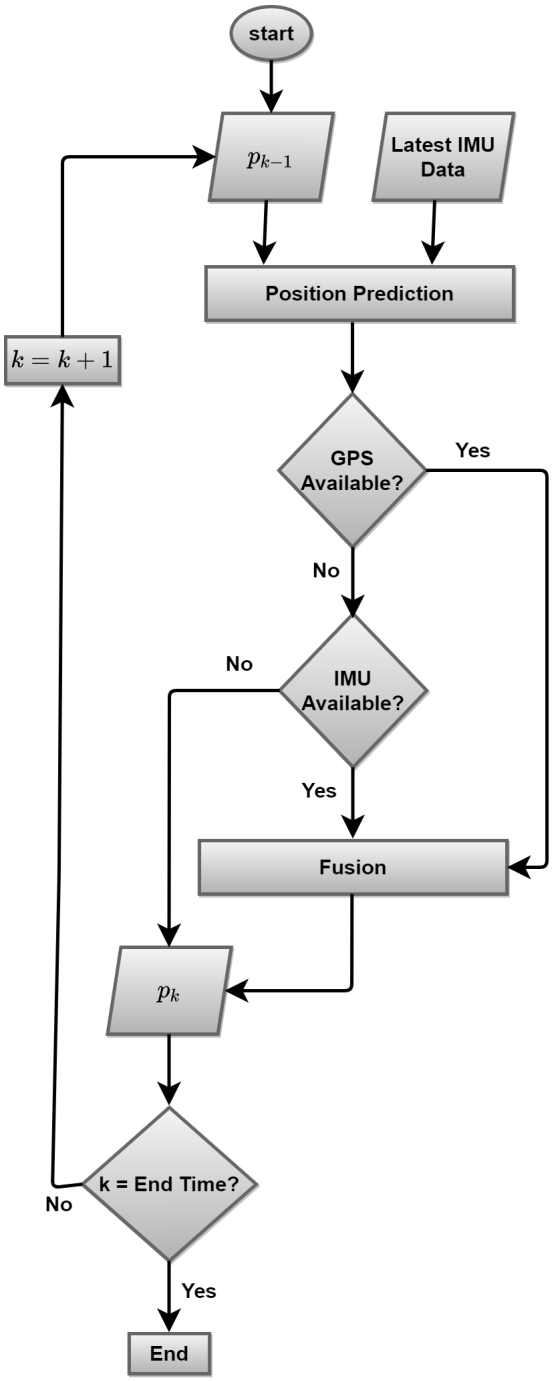

Figure 3.9: Flowchart for the proposed up-sampled algorithm. The latest IMU data is used to propagate the previous position p_{k-1} as a prediction for the next state. If a GPS measurement is available, it is fused with the prediction to produce the new position p_k. The latest IMU measurement is used to predict the next position at the up-sampled time epochs.

3.5 Up-sampled Particle Filter (UPF)

The particle filter implementation utilizes the same up-sampled time vector and the latest IMU values to propagate the particle cloud to the next position. The process for the UPF is the same as the flowchart shown in Fig. 3.9 where each sample in the particle cloud is propagated to the next position using (3.10). In this implementation, the proposed distribution is Gaussian with a variance equal to the variance in GPS measurements when the platform is stationary. The particle cloud is initialized with the proposed distribution with an expected value equal to the first GPS measurement. Each time the particle filter is propagated, a small amount of process noise is added to incorporate compounding errors. The weighting function used to determine the importance of each sample is the probability density function of a normal distribution shown in (3.24) as

$$f(x) = \frac{1}{\sqrt{2\pi\sigma^2}} e^{-\frac{(x-\mu)^2}{2\sigma^2}} \tag{3.24}$$

where σ is the standard deviation and μ is the mean. This equation is used to calculate how likely it is to receive the GPS measurement given that each particle position is assumed to be correct. As a result, the weights will be smaller for particles farther away from the GPS measurement and larger for the particles closer to the GPS measurement. The process allows for the possibility of non-Gaussian distributions in the particle cloud as the weights can cause the particles to converge to multiple values before finally converging to the true value. This concept is demonstrated in the simultaneous location and mapping (SLAM) algorithm used in autonomous navigation [10]. The weight values are then used to re-sample the particle cloud. The re-sampling algorithm randomly samples the point cloud based on the cumulative sum of the weighting values. This technique allows for values that have a larger

likelihood of being correct to be chosen and allows the algorithm to converge on the true value over time. The re-sampling step is done only when a measurement based on sensor data is available. Re-sampling the particle cloud when there is GPS data available allows for the cloud to converge towards the true position. An example of the particle cloud compared to the GPS measurement is shown in Fig. 3.10.

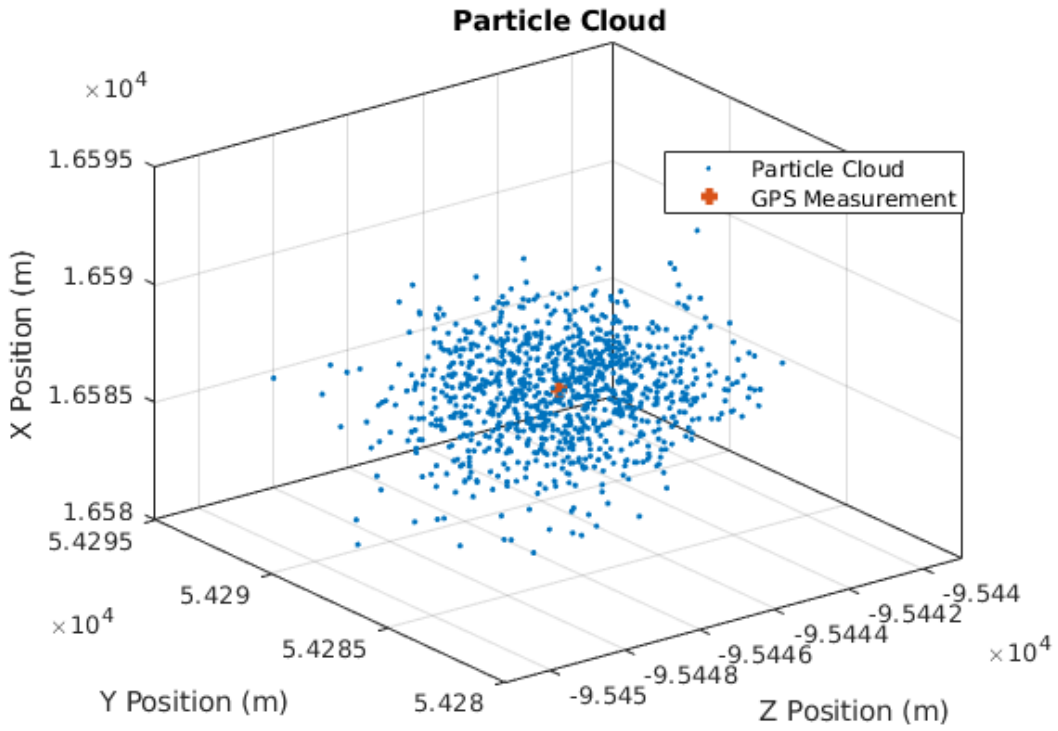

Figure 3.10: Example of a particle cloud. This is a particle cloud of 2×10^3 particles with a mean close to the GPS measurement.

3.6 Summary

Techniques used to overcome the challenges presented by the utilizing any one sensor are described in this chapter. The Kalman filter is a tried and true technique that leverages the assumptions of Gaussian sensor noise and linear models. The technique utilizes a weighted average of the predicted location and each GPS sensor measurement. The weighted average is calculated based on the covariance of the state space vector and results in an intelligently fused combination of the predicted and the measured positions to provide highly likely position solutions.

This chapter also presents the increasingly popular particle filter which creates a sample representation of the posterior distribution of the position estimates. The sample representation is refined using the measured positions from GPS. The idea is the positional accuracy increases proportionally with the accuracy of the sample representation of the positions solution.

Although these techniques allow for accurate positional estimates and are effective in overcoming the challenges provided by the sensors, increasing the frequency of which these positions are provided are helpful in the SAR application. Interpolation methods applied to these algorithms are applied to both methods and are effective in increasing the frequency of positional solutions. The increased frequency of the positional solutions is critical for the SAR application. In the next chapter, the basics of SAR are described and the effects of positional inaccuracies on the SAR product are presented.

4 SAR Basics

In this chapter, the signal model and the effects of position perturbations on the final SAR product is discussed. The basics of SAR including the advantages and motivation of SAR are presented. Furthermore, the SAR processing technique utilized in this dissertation is the backprojection algorithm. The backprojection algorithm is described in brief to provide background on how the images are formed. Additionally, the effects of position perturbations are universal regardless of the algorithm used as the effects largely impact the signal received and will need to be compensated for.

Synthetic aperture radar (SAR) is a radar signal processing technique to form images from successive radar pulses. The technique utilizes a mobile radar to generate a synthetic aperture that allows for increased spatial resolution as compared to non-mobile radar techniques. In general, the larger the synthetic aperture the finer the spatial resolution of the final image is. The core concept of SAR is that mobile radar projects radio frequency (RF) energy with successive pulses of the radar. The energy reflected from a scatterer of each pulse is then processed in a way such that the effects from the motion of the radar are removed. As a result, the energy from any specific scatterer is focused on a single-pixel representing the location of the scatterer. This process is done for each pulse transmitted during the aperture and the result is an image of all the scatterers illuminated during the aperture. In order to accurately focus the image, the location of the radar must be intimately known for each pulse transmitted to accurately combine the energy reflected from the scatterers. If the position of the radar is not accurately known, the energy reflected from the scatterer could span multiple pixels which results in a blurred image of the target scene. An example of the SAR collection geometry is shown in Fig. 4.1.

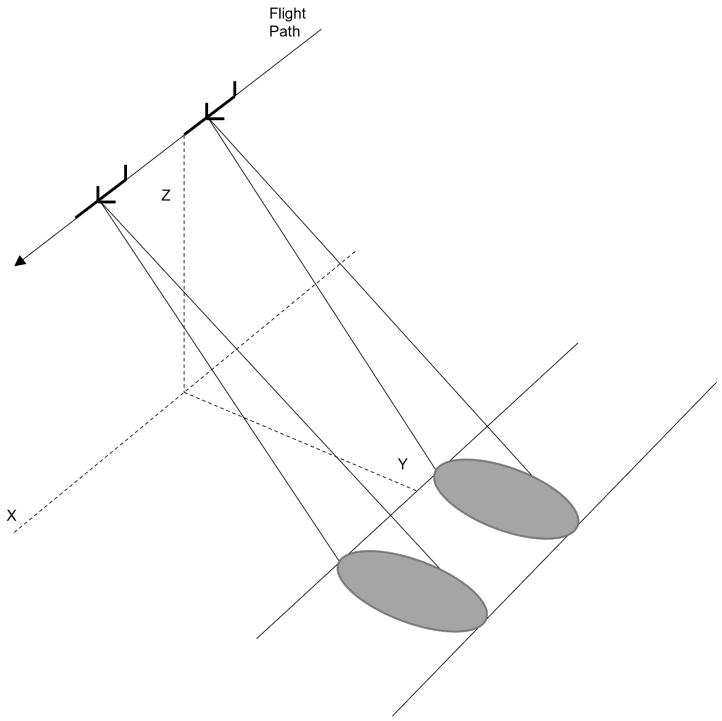

Figure 4.1: A picture of the SAR concept where multiple pulses are transmitted as the radar moves. In doing so, the scene is illuminated as depicted by the gray ovals. In addition, the distance between the minimum range and the maximum range illuminated is known as the swath.

In general, radars detect the distance a target is from the radar by transmitting an electromagnetic pulse and listening for the reflection of the pulse from the target. The range to the target is extracted by measuring the time between the end of the transmitted pulse to when the reflected pulse is received [61]. In doing so the range to the target is extracted by

$$R = \frac{c(\tau)}{2} \tag{4.1}$$

where τ is the measured time from transmission to receipt of the reflected pulse. The range is calculated using the measured time that is representative of the two-way transmission and is divided in half and multiplied with the velocity of the

transmitted signal is the speed of light c. Equation (4.1) is known as the cross-track resolution defined as the resolution perpendicular to the motion path. In applications where the radar is measuring the distance from the radar along a Cartesian axis with the radar at the origin, the cross-track resolution can be directly calculated using equation (4.1) [49]. However, the cross-track resolution is different in applications, such as side looking airborne radar (SLAR), where the radar is imaging the ground at an angle. As shown by Fig. 4.2, the ranges from each end of the swath will produce a different return based on the incident angle.

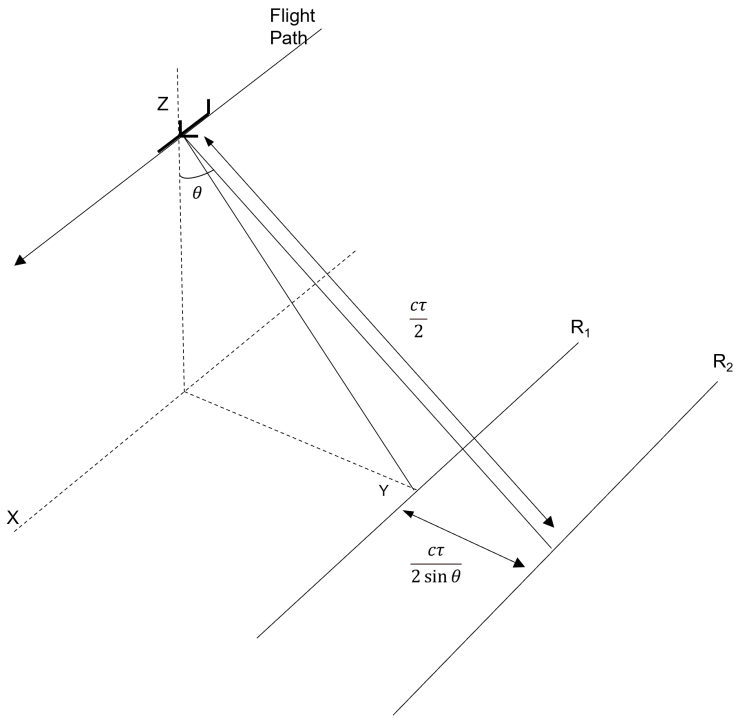

Figure 4.2: A picture of the effects of changing the incident angle of the radar in ground imaging applications. The detection of R_1 will be different than the detection at R_2.

As a result, the resolution in cross track becomes

$$\triangle R_c = \frac{c(\tau)}{2\sin\theta} \tag{4.2}$$

where $\triangle R_c$ is the cross-track resolution and θ is the incident angle used in the ground imaging radar or SLAR applications. From equation (4.2), the range resolution becomes equation (4.1) as the incident angle becomes broadside or $\theta = 90°$.

The cross track resolution can be increased by using the *pulse compression* concept where the relationship of the bandwidth and pulse width is exploited to increase the energy on target. The relationship between bandwidth and pulse width, τ is defined by

$$B = \frac{1}{\tau} \ . \tag{4.3}$$

In non-modulated scenarios, the length of the pulse is increased in order to increase the amount of energy on the target. With an increased amount of energy, the resolution is increased as evident by equation (4.1). Pulse compression utilizes equation (4.3) to trade length of the pulse for bandwidth. As a result, the resolution in the cross-track dimension described by equation (4.2) can be transformed and expressed by

$$\triangle R_c = \frac{c}{2B\sin\theta} \ . \tag{4.4}$$

As shown by equation (4.4), the increase in bandwidth directly translates to a increase in resolution that can be resolved by the radar. The pulse compression technique modulates a waveform to increase the bandwidth while maintaining a short pulse length and the most common waveform utilized is the linear frequency modulated (LFM) waveform also known as a "chirp". The LFM waveform is aptly named as it linearly increases the frequency throughout the pulse length and is shown in Fig. 4.3.

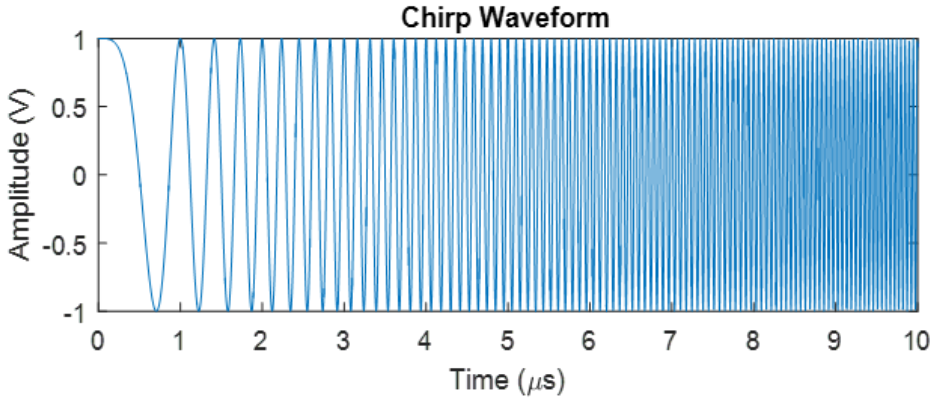

Figure 4.3: A Linear Frequency Modulated Signal (Chirp)

The equation for the LFM pulse can be tuned to increase and decrease bandwidth by changing the chirp rate of the waveform. The chirp rate at which the frequency changes in the waveform. The mathematical representation of the LFM pulse is represented by

$$a(t) = A\mathrm{e}^{j\pi BTt^2} \tag{4.5}$$

where A is the amplitude of the waveform, T is the pulse width and t is the time vector. The pulse compression technique is realized by processing the received signal using the *matched filter* concept. Matched filtering is conducted by first taking the time reversed complex conjugate of the transmitted signal. The time reversed complex conjugate is then convolved with the received signal.

In terms of radar, the larger the antenna means the larger the aperture, and the more information obtained by the radar. The increase in information provides a proportional increase in resolution. For airborne radars, a challenge of flying large antennas arise and systems have to trade-off between resolution and physical aperture size. The resolution obtained by physical aperture antennas are dependent on the beam width of the antenna, β. The resolution in the along track dimension, or

the resolution parallel to the direction of motion, can be calculated by

$$\triangle R_a = \beta R \tag{4.6}$$

where R_a is the along track resolution, β is the azimuth 3-dB beam width of the physical aperture and R is the range calculated by equation (4.1). For physical antenna apertures the 3-dB beam width can be estimated using the physical dimensions of the antennae. The estimation for beam width is

$$\beta = \lambda / D \tag{4.7}$$

where λ is the wavelength of the transmitted signal and D is the azimuth dimension of the physical antenna. Combining equations (4.6) and (4.7). The along-track resolution is expressed by

$$\triangle R_a = \frac{\lambda R}{D} \ . \tag{4.8}$$

In SAR, the aperture of the system is not acquired by increasing the physical size of the radiating and receiving antennas. Instead, the aperture is created by moving a physically smaller antenna and using signal processing to synthetically create a bigger aperture by combining the information such that the results are similar to a larger physical antenna. In this way, a larger aperture is *synthesized*. The increased aperture increases the spatial resolution in the image axis that coincides with the axis of motion, also known as the along-track dimension, and is the x-axis in Fig. 4.1. The introduction of SAR solves the issue and allows airborne systems to maintain resolution while flying small antennas.

In order to accomplish higher resolution in the along track dimension using smaller physical antennas requires the exploitation of the Doppler effects on the received reflection from the target scene. The Doppler shift created by the motion

of the radar allows for the signals to distinguish targets between pulses within the aperture. As a result, the azimuth resolution is directly coupled with the amount of Doppler shift that can be distinguished by the system. A detailed introduction to SAR signal processing is presented by [11]. In short, the frequency shift introduced by the motion of the radar is calculated by

$$\triangle f_d = \frac{v \triangle R_a}{R\lambda} \sin\theta \tag{4.9}$$

where $\triangle f_d$ is the differential frequency, θ is the squint angle or the beam width, and v is the velocity of the platform. Understanding the differential Doppler frequency $\triangle f_d$ drives a requirement of sampling for a time approximately to $T \approx 1/\triangle f_d$ yields the aperture length, L, to be calculated by

$$L = \frac{v}{\triangle f_d} = \frac{R\lambda}{\triangle R_a \sin\theta} \ . \tag{4.10}$$

Solving for $\triangle R_a$ results in the azimuth resolution for SAR to be determined by

$$\triangle R_a = \frac{R\lambda}{L} \ . \tag{4.11}$$

As a result, the larger aperture increases the resolution in the along-track dimension which can be accomplished by moving a smaller physical aperture to achieve a larger synthetic aperture. It should be noted that the azimuth resolution $\triangle R_a$ is dependent on the line of sight range to the target scene R. As a result, the azimuth resolution needs to be determined by balancing the distance to the scene and the length of aperture flown to obtained the desired resolution.

4.1 Navigation effects

Capturing the precise motion of the radar is crucial in SAR applications in order to create a focused image of the target scene. Fundamentally, SAR requires coherent phase history from scatterers in the aperture on a pulse-by-pulse basis. These phase histories allow for the pulses to be coherently integrated after Doppler processing to form an image of the scatterers within the scene. Ideally, GPS and IMU systems are chosen that have the same, or similar, sampling rates as the PRF of the radar. This allows the radar pulses to be synchronized with the position estimates from the GPS and IMU. In general, this is most applicable if a pulsed-Doppler radar architecture is being used. This is not as critical for frequency modulated continuous wave (FMCW) radar architectures where the system is continuously transmitting and receiving. However, the use of FMCW radar architectures for SAR imaging has its complications such as intra-pulse range migration [54].

In addition to synchronization between the PNT solution and the radar, it is also critically important for the PNT data output to be incredibly accurate. If low-quality GPS and IMU sensors are used, techniques such as autofocus are often employed to compensate for the inaccuracies of the IMU and GPS systems. Autofocus algorithms estimate the phase errors caused by the SAR system, including the position measurement errors, and compensates for the errors when forming a SAR image [8, 26, 29, 67, 73]. For SAR systems that do not use autofocus algorithms as part of the motion compensation, the phase alignment is strictly accomplished by using the data output from the navigation system [36]. As a result, high-accuracy GPS and IMUs are required for most SAR applications [19]. The selection of high-accuracy navigation sensors are typically constrained by the available sampling frequency and the associated cost, size, weight, and power (C-SWaP) of these units. If C-SWaP is not a constraint, then the primary consideration is choosing a system that

can meet the desired sampling requirements. For the remainder of this paper, it is assumed that the C-SWaP of navigational-grade IMUs is not a factor, but the sampling frequency is significantly lower than the PRF of the system and autofocus techniques are not available.

To understand the impact of misaligned sampling frequencies between the GPS, IMU, and radar, it is important to understand how phase plays an important role in SAR image formation. The phase of a SAR waveform is affected by the modulation from the radar transmitter and the two-way free-space wave propagation to and from a scatterer. The total phase measured by a SAR system is calculated as

$$\phi(t) = \frac{4\pi}{\lambda} R(t) + \phi_T(t) \tag{4.12}$$

where $\phi_T(t)$ is the modulation caused by the transmitter and λ is the center frequency wavelength, and $R(t)$ is the range to the scatterer. In most SAR systems, $\phi_T(t)$ and λ are intimately known and the range to the scatterer is the parameter being estimated given the estimated relative position of the radar from the GPS/IMU. However, the sensitivity to phase accuracy increases with an increase in the radar carrier frequency as the radar wavelength proportionally decreases. From (4.12), as the wavelength decreases, the amount of phase change for a given range increases. Thus, any inaccuracies in the estimated range to the target will result in poor phase estimation, which becomes excessively large at high frequencies. Therefore, it is essential to use a high-quality GPS/IMU to ensure that the relative position of the radar platform is accurately defined such that phase errors are minimized and can be compensated during SAR processing. More specifically, the accuracy required to focus a SAR image requires the errors in range, $R(t)$ to be limited to $\lambda/16$. The

phase errors tolerable by the SAR system is estimated by

$$\phi(t) = \frac{4\pi}{\lambda}\frac{\lambda}{16} = \pi/4 \ . \tag{4.13}$$

Given the required range accuracy is limited by the carrier frequency wavelength, the tolerance for positional errors is increasingly smaller as the carrier wavelength is increases. This is a fundamental constraint for high frequency SAR systems as highly accurate position solutions become increasingly harder to obtain. The desire to increase frequency of SAR radars is driven by the ability to miniaturize physical apertures and components of the system.

However, a SAR system with error-free position solutions can still have issues creating a focused image if the sampling rate of the positions is not synchronized with the SAR PRF. While the above equation allows for the calculation of the total phase change on a single pulse, the radar will transmit and receive several pulses throughout the coherent processing interval (CPI), and thus the range from the radar platform to any given scatterer will change on a pulse-by-pulse basis. Before Doppler processing in traditional SAR algorithms, the individual phase histories, correlated to the range profiles of each scatterer, are aligned along the slow-time radar data such that all the power will compress into a single range bin after Doppler processing. This "alignment" is accomplished by slightly increasing or decreasing the phase change of each fast-time radar data set, which can be precisely determined if the position of the radar platform is known on each pulse of the radar throughout the CPI. This is why it is important for the PNT solution to be accurate but also produce position estimates at the same rate as the radar. If the position estimation data is not available for each radar pulse, the phase for each fast-time radar data set cannot be adequately compensated for and the resulting SAR image will look blurry as the power will smear across multiple bins after Doppler processing

instead of being “focused” into a single bin.

As a result, popular interpolation techniques have been introduced in scenarios like this to estimate the position at the radar PRF between GPS/IMU data samples. However, if the data GPS/IMU data samples are too spread apart temporally, techniques such as the linear or spline interpolation are inadequate in SAR imaging applications. The primary reason these interpolation techniques are insufficient is that they are polynomial interpolations and do not capture the external forces acting on the radar. As a result, the interpolation introduces its own phases errors rather than compensating for them. In order to provide a position solution capable of coherently integrating the phase histories from a SAR scene, an interpolation technique is required that accurately estimates the position of the radar when GPS/IMU data is not available. Such a technique would allow for pulsed SAR systems to no longer be constrained by the sampling rates of the IMU and GPS systems.

4.2 Backprojection

In order to synthesize a larger aperture, the signals received for each location of the SAR system need to be processed in such a way that energy reflected by targets is coherently added. The additive combination of the reflected energy simulates the additional energy that would be received from a physically larger aperture. However, the challenge is the motion of the SAR system adds variation to the information that causes the reflected energy to misalign. In addition, the physical position of the receiving antenna changes meaning the range to a scatterer is not necessarily directly the same as the range detected in other pulses. These errors need to be corrected and compensated for so that the received data to correctly synthesize a single aperture.

One method of correcting for these errors is an algorithm known as *backpro-*

jection. The backprojection method works by first defining a grid with each space associated with specific locations within the area of interest. The grid serves as the image representation of the area illuminated by the radar and is predefined. Each received pulse is interpolated to the ranges represented in the grid [2]. For each space in this grid, the phase of the range profiles is corrected based on the distance between the radar. The correction is done for every pulse within the aperture and the resulting image produced by each pulse is summed. As a result, the effects of motion are corrected for each pulse so that when summed the targets illuminated in the scene coherently sum to produce a high intensity in the final image. Conversely, pixels representing a space with no targets do not coherently sum and result in a low intensity in the final image. When the pixels are displayed as an intensity map, an image of the illuminated scene can be seen. As the backprojection algorithm processes each pixel of the image for every pulse in the aperture it is flexible to different motion paths and SAR modes. Additionally, the method allows for flexibility in the size and resolution of the image formed as shown in [15]. A more in-depth derivation of the backprojection algorithm is given in [18][25].

4.3 Summary

In this chapter, an introduction to SAR signal model and the methodology of producing an image from the SAR data is presented. The effects of phase errors caused by inaccurate position solutions are mathematically shown. Additionally, the concept of SAR is described where an aperture is physically synthesized by intelligently processing echoes from a smaller moving aperture. In short, the concept of SAR relies on the Doppler shift introduced by radar motion to distinguish targets between echos. In doing so the radar is able to coherently combine the energy reflected by a target to synthesize the behavior of a larger physical aperture. The result is a higher spatial resolution in the produced SAR image. It is established that this resolution requires the Doppler error caused by range to be limited to $\lambda/16$. With such a constraint, the importance of an accurate position solution from the PNT system is emphasized. The backprojection algorithm is presented as a popular method of processing the data obtained by the SAR technique in order to produce an image. As a result, the algorithm depends on accurate position solutions in order to correctly account for the SAR signal properties in order to produce a 2-dimensional reconstruction of the illuminated scene. Furthermore, the effects of positional inaccuracies are also presented in this chapter. In the next chapter, an approach to overcoming the challenge large, accurate INS systems pose when miniaturizing the SAR system is described.

5 Multi-IMU Fusion

This chapter presents an approach to addressing the second challenge of providing accurate positional accuracy for SAR. Additionally, the technique utilizes the benefits of data fusion to also minimize the C-SWAP required to provide the required positional accuracy. This method is counter intuitive as it requires the addition of sensors in order to decrease C-SWAP. Simulations used to validate the method are also described. Furthermore, the simulations used to validate the interpolation methods presented in previous chapters is also shown. Finally, the instrumented setup used to verify the techniques during ground tests and flight tests are presented along with the results validating the methods. The results in this chapter allow for the confidence to move forward with the next step of utilizing the methods in a SAR system.

The multi-IMU fusion method combines the particle clouds from multiple particle filters each propagated from different sensor measurements. The particle filter is chosen for its ability to scale to additional sensors without increasing the complexity in the algorithm as discussed by [43]. Unlike the Kalman filter, the particle filter does not rely on a covariance estimation between the additional sensors and is ideal for this application of adding additional IMUs to the system. A block diagram of the algorithm is shown in Fig. 5.1. The proposed method uses sequential importance sampling principles and the performance is evaluated based on the mean squared error (MSE). Sequential importance resampling is used to increase the accuracy of the sample representation of the particle filter. In doing so, the samples that are the most likely are weighted based on an observed measurement. The weights are then used to draw samples and replace the unlikely samples within the particle cloud. The logical idea is that the measurements provide observed changes in motion experienced by the platform and the measurements are used to increase

the accuracy of the final position estimate. In addition, the particle clouds are synthetic sample representations of the posterior probability distribution. According to the sampling theorem more samples allow for a more accurate PDF of the measured variable. The additional measurements act as additional observed samples used to represent the probability distribution accurately. In addition, the particle filter is a sequential Monte Carlo technique which allows for more accurate state estimations as the number of Monte Carlo simulations are increased [59]. Utilizing this principle, the core of the multi-IMU measurements is to incorporate more observations of the physical motion changes experienced by the platform in order to more accurately represent the posterior distribution of the platform position. The proposed method is compared to the traditional method of combining measurements, such as taking the mean of the particle filter estimations, to directly compare performance accuracy of the two different methods. As a result, the true value of the measured state can be more accurately estimated. More specifically, the proposed method uses each sensor measurement as additional samples to more accurately estimate the measured acceleration and ultimately position of the platform.

The method of utilizing multiple particle filters in navigation applications is growing where additional particle filters are used to correct for errors [44]. This technique utilizes the second particle filter to estimate the most likely correction value to be applied to the original particle filter. In this way, the two particle filters estimate different parameters of the navigational platform. The first particle filter estimates the position of the platform by performing data fusion on the sensor information obtained and the second particle filter estimates a correction factor given a corrected GNSS solution. The work presented in this dissertation differs where the first particle filter estimates the position solution from each individual IMU and GPS to address the sensor drift from each IMU. The SIR method is then used to

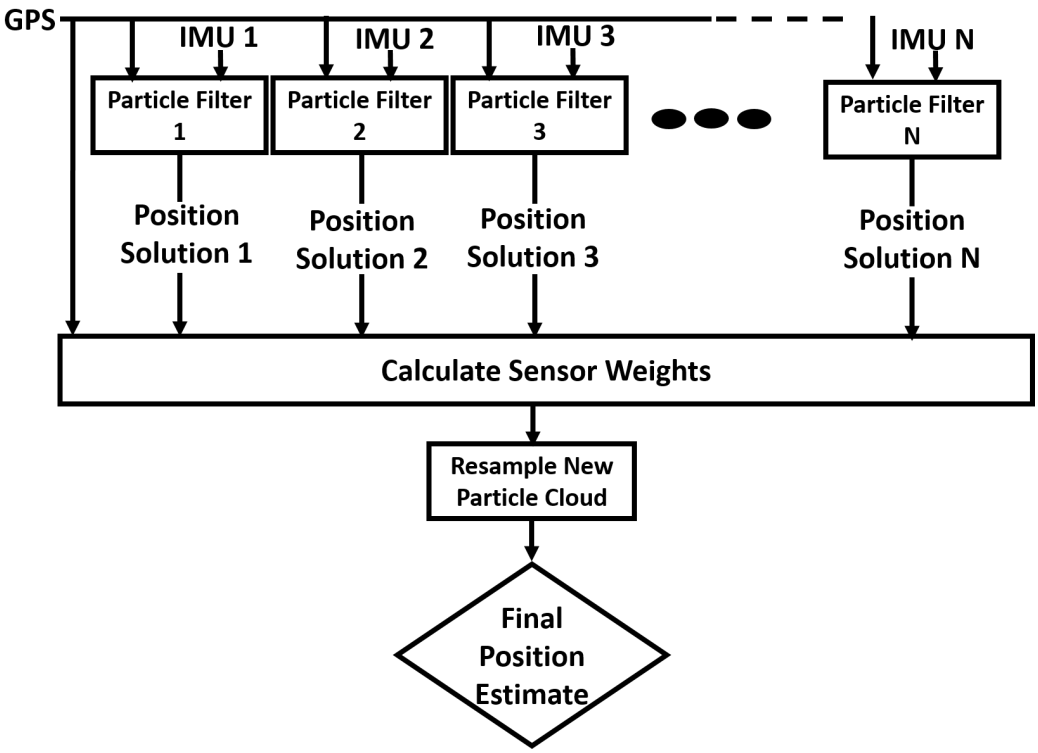

Figure 5.1: Block diagram of the proposed algorithm. To begin, GPS measurements are fed to each sensor particle filter and the sequential importance resampling technique. Each sensor weight is calculated based on the likelihood that the sensor is accurate compared to GPS. The weights are then normalized using (5.3). The final position is calculated using (3.23).

evaluate the accuracy of these solutions to better represent the posterior distribution of the platform position. In this work, the particle filters are not estimating any correction factors and is instead evaluating the likelihood of the positional solutions provided by each sensor. From these likelihood, the posterior distribution of the platform position can be more accurately estimated which increases the final estimate of the position solution for the platform.

The increased accuracy provided by the algorithm allows for smaller and lower-grade IMUs to be used to achieve better accuracy than a single IMU of similar quality. This feature can be used to utilize multiple lower-grade IMUs to match the

positional accuracy of a larger higher-grade sensor. As a result, the low C-SWAP of lower-grade sensors can be leveraged without sacrificing the accuracy provided by higher-grade sensors. The proposed method is inspired by the sequential importance resampling (SIR) principle where weights are assigned to each of the particles and then used to re-sample a set of new particles comprised of more highly weighted particles. The proposed method applies the same methodology by assigning weights to the outcomes of each sensor estimation. The sensor weights do not take into account the particle weights computed by the particle filter. The sensor weights are a measure of how accurate the particle filter solution is for that sensor are not dependent on the particles that were used to compute the estimation. The sensor weights can be calculated similarly to the particle weights calculated in the particle filter as the principles still apply. In this paper, the particle filters used 1000 particles to resolve the position solution for each sensor. The weighted estimations are then used as the proposal distribution for a new particle filter, which then draws a set of particles from the proposal distribution according to the weighted sensor estimations. A new estimate is then calculated by taking the expected value of the new particle cloud and the weights are calculated using (3.22). The new particle cloud collects several samples ($N = 50$) from the weights and the respective sensor estimation is used as part of the new particle cloud. By doing so, the sensor with the highest weight is selected more often during the creation of the new particle cloud.

The pseudo-code for the implemented algorithm is illustrated as Algorithm 1. The algorithm first resolves each of the sensor measurements using a particle filter. The results of each of the particle filters are then fused. The method used to fuse each sensor output is based on the re-sample step in particle filtering, where a weight is assigned to each sensor measurement calculated based on the likelihood of the position solution compared to a GPS solution. The sensor weights are then used

Algorithm 1: Implemented Algorithm.

```
   // Initialize cloud with N number of particles
1  for Each Sensor do
2      InitializeCloud(mean,variance,N)
3      Set N_th; // Set threshold of Effective particles
   // For Each Sensor Measurement, Propagate the
      respective cloud by motion model
4  for Each State(k) do
5      for Each Sensor do
6          for Each Particle do
               // p_{k-1} is the previous position
7              Propagate(p_{k-1},dt,SensorMeasurement)
8              CalculateParticleWeights(cloud)
9              NormalizeParticleWeights; CalculateNeffective(w_k^i)
10             if N_effective < N_th then
11                 Resample(cloud)
12         CalculateEstimation
13     Calculate sensor weights
14     Normalize sensor weights
15     for i=1:N do
16         CombinedCloud(i) = Draw particles from sensor proposal
17     FinalMeasurement p_k = E[CombinedCloud]
```

to produce several samples according to the weighted sensor outputs. The expected value of the samples is then used as the final position estimate for the navigating body.

5.1 Cramer Rao Lower Bound

The sensor weights are normalized and can be used to estimate an effective number of independent samples. The sample space is given by each of the sensor outputs as defined by

$$x_1, x_2, x_3, ..., x_s \tag{5.1}$$

where s is the number of sensor outputs. When using SIR to resample the sensor spaces given a set of weights the sample space is given by

$$x_1, x_2, x_3, ..., x_N \tag{5.2}$$

where N is now the number of samples drawn from the sample space S. As a result, the sensor weights can be used to calculate the effective samples (N_s). The weights correspond to $w_s(1 \leq s \leq N)$ and the normalized form becomes

$$\hat{w_s} = \frac{w_s}{\sum_{\mathrm{s=1}}^{N} w_s}. \tag{5.3}$$

The effective independent samples are then calculated by

$$N_s = \frac{1}{\sum_{\mathrm{s=1}}^{N} \hat{w_s}^2} \tag{5.4}$$

where N_s is bound by $1 \leq N_s \leq N$ showing that resampling the sensor outputs using sensor weights do not introduce a dependency between sensors. Furthermore, resampling produces independent, identically distributed (i.i.d) samples that are drawn from a discrete density as explained by [3]. As a result, the independent samples drawn from the sensor measurement can be applied to the central limit theorem (CLT). The CLT states that the normalized sum of independent samples can be approximated as a normal probability distribution with a fixed mean and variance. This assumption allows for the use of the simplified Gaussian form of the Cramer Rao lower bound (CRLB)[35].

The CRLB establishes the lowest amount of variance of an unbiased estimator. Applied to the proposed algorithm the CRLB expresses the lowest amount of variance that is expected in the navigation solution when fusing multiple sensors [39].

The Cramer Rao lower bound calculated using

$$CRLB = \frac{1}{-\mathbf{E}\left(\frac{d^2 \ln(p(x;\mu))}{d\mu}\right)\Big|_{\mu=true}} \tag{5.5}$$

where the denominator is the Fisher information matrix. The sensors in a navigation platform produce independent samples of the platform position and the SIR method uses the principle of weighted sampling described by 5.4, where the solution from each sensor is represented as

$$\hat{x[n]} = x + w[n] \ . \tag{5.6}$$

In equation (5.6), x is the true position of the platform and $w[n]$ is white Gaussian noise with a given variance σ^2. Given the sensors are independent, identically Gaussian distributed with the expected value being the true platform position then the probability distribution for the sensor estimates can be expressed by

$$\begin{aligned} P(\hat{x};x) &= \prod_{k=1}^{N-1} \frac{1}{\sqrt{2\pi\sigma^2}} e^{-\frac{1}{2\sigma^2}(\hat{x[k]}-x)^2} \\ &= \frac{1}{(\sqrt{2\pi\sigma^2})^{N/2}} e^{-\frac{1}{2\sigma^2}\sum_{k=0}^{N-1}(\hat{x[k]}-x)^2} \end{aligned} \tag{5.7}$$

where N is the number of sensor solutions. The first step in evaluating the Fisher information matrix is taking the first derivative of the natural log of equation (5.7). The result can be shown by

$$\frac{\partial \ln(p(\hat{x};x)}{\partial x} = \frac{\partial}{\partial x}\left(- ln((2\pi\sigma^2)^{N/2}) - \frac{1}{2\sigma^2}\sum_{k=0}^{N-1}(\hat{x[k]}-x)^2 \right) \tag{5.8}$$

$$= \frac{1}{\sigma^2}\sum_{k=0}^{N-1}(\hat{x[k]}-x) \tag{5.9}$$

Evaluating the summation and taking the second derivative simplifies the solution

in equation (5.8) as demonstrated by

$$= \frac{1}{\sigma^2} \sum_{k=0}^{N-1} (\hat{x[k]} - x) \tag{5.10}$$

$$= \frac{N}{\sigma^2} (\hat{(x)} - x) \tag{5.11}$$

$$\frac{\partial \frac{N}{\sigma^2} (\hat{x} - x)}{\partial x} = -\frac{N}{\sigma^2} \tag{5.12}$$

Combining the solution obtained in equation (5.10) with the definition of the CRLB expressed in equation (5.5) allows for the CRLB to be

$$Var\{\hat{x}\} \geq \frac{\sigma^2}{N} \ . \tag{5.13}$$

Equation (5.13) establishes the variances of the positional estimates from each sensor is bound by a single sensors positional variance divided by the number of sensors used. Although this is applicable to a single time step and can be used for a back of the envelope calculation for the number of sensors needed.

For the SIR method, the CRLB is insufficient in estimating the variance because the method is recursively used to represent the posterior distribution. As a result, the CRLB for a single time step only provides a first order approximation of the positional accuracy of the SIR method. In order to more accurately approximate the SIR method, the variance can be of the estimator using the sequential Monte Carlo where the variance of the Monte Carlo solution cam be estimated using

$$Var\{\hat{x}\} \approx \frac{n}{N} \left[\int \frac{\pi_n^2(\hat{x_1})}{q_1(\hat{x_1})} \partial \hat{x_1} - 1 + \sum_{k=2}^{K} \int \frac{\pi_n^2(\hat{x_k})}{q_k(\hat{x_k})} \partial \hat{x_k} - 1 \right] \ . \tag{5.14}$$

In equation (5.14), the probability density of the sensor estimates is represented by $\pi_n(\hat{x_k})$ where n is the sensor and k is the time step. Furthermore, the proposal distribution is represented $q_k(\hat{X}_k)$ and is the distribution used to calculate the weights

of each sample during the SIR process. Equation (5.14) captures the recursive nature of the SIR method where the first time-step, $\int \frac{\pi_k^2(\hat{x_1})}{q_1(\hat{x_1})}\partial\hat{x_1} - 1$, is distinguished from the future time steps, $\sum_{k=2}^{K}\int \frac{\pi_k^2(\hat{x_k})}{q_k(\hat{x_k})}\partial\hat{x_k} - 1$. This distinction allows for the distribution of the previous time step to be utilized as the proposal distribution in the next time step. The proposal distribution for time steps 2 through N are described by

$$q_k(\hat{x_k}) = \pi_{k-1}(x_{1:\hat{k-1}})q_k(x_{1:\hat{k-1}}) \ . \tag{5.15}$$

A full derivation of the sequential Monte Carlo variance is presented in [24]. In the multi-IMU fusion technique q_k is used to calculate the sensor weights and is a distribution representing the GPS sensor. Furthermore, $\pi_n(\hat{x_k})$ is a distribution representing the positional solutions from the IMUs. As a result, solving equation (5.14) for N gives an estimate of the number of sensors needed to accomplish a desired positional accuracy $Var\{\hat{X}\}$ and the desired number of time steps k.

In order to both calculate the CRLB or the sequential Monte Carlo a distribution for the IMU sensors needs to be represented. Assuming the distribution can be model by an expected value and variance, the variance of the positional solution needs to be estimated. The expected value can be assumed to be the true position of the platform. The variance of the positional solution can be viewed as the errors in the position estimates from the IMUs. In this case, the positional errors are caused by integrating the errors from the accelerometers, the initialization error in velocity, and the initial position error, calculated by

$$P_e(t) = \iint_{\tau=0}^{t} a_e(\tau)d\tau d\tau + \int_{\tau=0}^{t} v_e(0)d\tau + P_e(0). \tag{5.16}$$

The errors in the acceleration measurement from the IMUs can be calculated by accounting for the errors in measured acceleration, the errors in rotating the measured

accelerations to the right coordinate frame, and the errors in the gravity and earth rotation models.

$$a_e(t) = R_t(t)a_e^{'}(t) + R_e^{'}(t)\big(a_t^{'}(t) - a_g^{'}(t) - a_r^{'}(t)\big) + R_e(t)a_r^{'}(t) + R_e^{'}(t)a_g^{'}(t) \tag{5.17}$$

In equation 5.17, $R_t(t)a_e^{'}(t)$ is the errors in the measured acceleration where $R_t(t)$ represents the true rotation matrix for rotating the accelerations to the correct coordinate frame. To represent misalignment, or errors in rotation, $R_e^{'}(t)(a_t^{'}(t) - a_g^{'}(t) - a_r^{'}(t))$ is the errors caused by rotating the true accelerations ($a_t^{'}(t)$), gravity ($a_g^{'}(t)$) and earth rotation ($a_r^{'}(t)$) to the desired coordinate frame with the misaligned rotation matrix ($R_e^{'}(t)$). Lastly, the errors in rotating the estimated earth rotation rate, $R_e(t)a_r^{'}(t)$ and estimated gravity $R_e^{'}(t)a_g^{'}(t)$ are all combined to estimate acceleration errors. The errors caused by angular random walk are accounted for in the rotation errors $R_e^{'}(t)$ and is represented in

$$R_e^{'}(t) = \begin{bmatrix} 0 & \theta_{z,e}(t) & -\theta_{y,e}(t) \\ \theta_{z,e}(t) & 0 & \theta_{x,e}(t) \\ \theta_{y,e}(t) & \theta_{x,e}(t) & 0 \end{bmatrix} \tag{5.18}$$

where $\theta_{x,e}, \theta_{y,e}, \theta_{z,e}$ are the errors in the estimated x, y, and z errors of the attitude of the platform, respectively. The error effects from the IMU can be estimated from the specification provided by the manufacturer of the sensors. In equation 5.17 the scale factor errors at a give acceleration, $B(a_t)$, are combined with the misalignment, θ_m, and non-orthogonality, θ_n. In addition, bias instability, b, white noise, N, and random walk, $RW(f) = K^2/(2\pi f)^2$ are also contributing factors to

errors from the IMU.

$$a_e^{'}(t) = B(a_t) + \sin(\theta_m + \theta_n) + b + N^2 + K^2/(2\pi f)^2 \tag{5.19}$$

Lastly, the IMU errors can be used with the true acceleration, a_t, and the duration, T, in which the acceleration is experienced to calculate the positional standard deviation calculated by

$$\sigma^2 = a_t(\frac{T^2}{2})a_e^{'}(t) \tag{5.20}$$

Using equation 5.13, and equation 5.20, the variance of the fusion solution can be calculated to have a lower bound of $\frac{\sigma^2}{N}$. As a result, the effects of the additional sensors can be estimated. Given a variance in the positional accuracy of all the sensors used, the number N can be varied to achieve the desired positional accuracy needed for the desired application. This can be used as a design tool to understand and select the appropriate sensors in order to satisfy the C-SWAP and accuracy constraints in estimating the position of a navigational platform. A simulation of 1000 measurements for a single time step are simulated and resampled using the SIR technique with a variable number of sensors. The sample variance of the position solution using is calculated across the sensors. The results were compared against sample variance of a single sensor divided by the number of sensors used in the SIR technique and shown in Fig. 5.2. As a result, the plot shows great agreement between the results of the SIR technique and the theoretical estimation using equation (5.13).

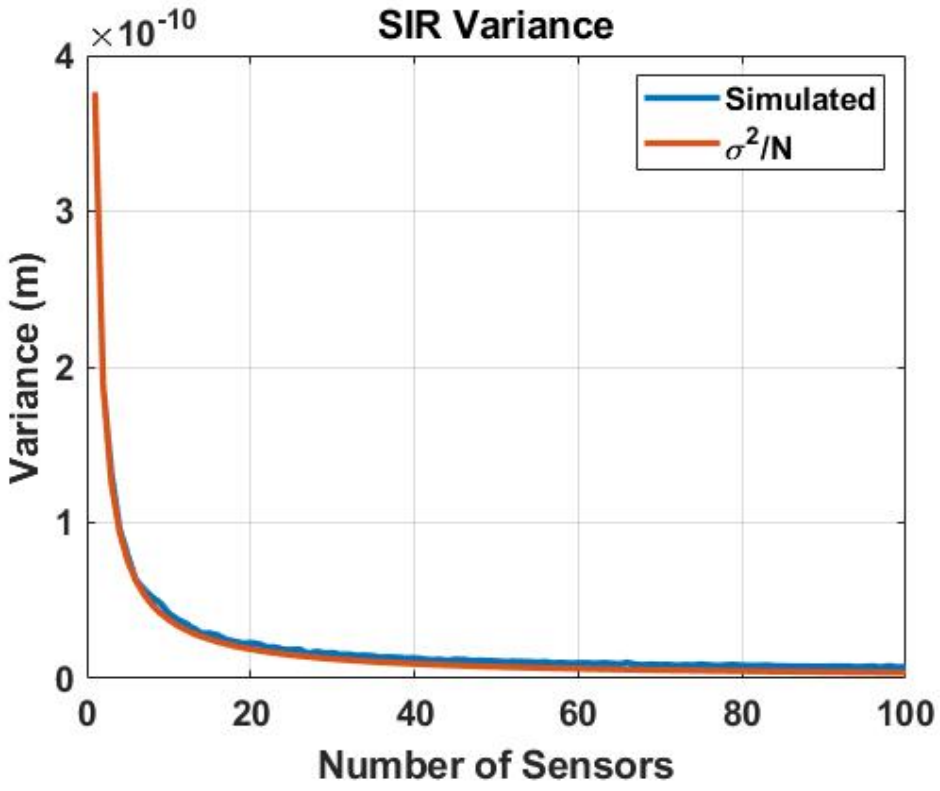

Figure 5.2: The variance of the Multi-IMU fusion method compared to the simulated sample variance for a single time step. The blue line is the variance across the 1000 position solutions created by the SIR technique. The orange is the sample variance of a single sensor divided by N sensors.

Additionally, the mean squared error of the SIR technique as compared to GPS is shown in Fig 5.3. It can be seen that the addition of more sensors results in a decrease in MSE compared to the error of the GPS measurement used to calculate the sensor weights. As more additional sensors are added the solution begins to converge to the GPS measurement. As the particle filter predicts and resamples more the MSE will continue to decrease. In Fig 5.3, the results are for a single time step and it is illustrated that the accuracy for a single timestep can be greatly increased given the addition of sensors and the SIR technique.

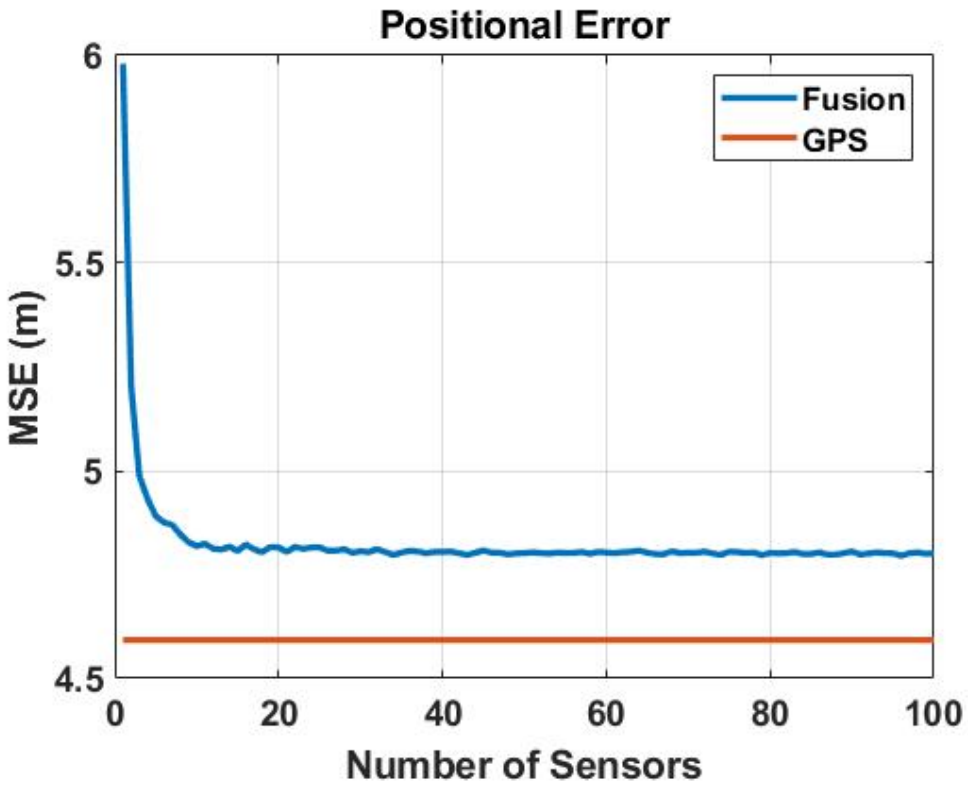

Figure 5.3: MSE of the SIR solution as compared to the GPS measurement error. The blue line represents the MSE achieved by the SIR technique for a single time step. The orange line is the error of the GPS measurement used for this single time step.

In Fig. 5.3, the error from the fusion technique is improved as sensors are added, however, the MSE does not converge to GPS completely because the MSE is only shown for a single time step. As a result, the sequential benefits of the SIR technique are not displayed. It should be noted that the law of diminishing returns is likely to contribute to designing multi-IMU navigational systems using the proposed method. As shown by Fig. 5.3 and Fig. 5.2, the benefits of adding additional sensors exponentially decrease with each sensor added. However, there is a point where the additional sensors do not provide a significant accuracy increase to the

final position estimated. In general, at some point, it will become unfeasible to add additional sensors due to other constraints in the desired application. Using the CRLB to estimate the number of sensors required to achieve a specific accuracy also allows for an estimation of C-SWAP required for the multi-IMU navigation system. As a result, the estimations allow designers to quickly determine if the chosen sensors are a benefit in decreasing C-SWAP while obtaining the positional accuracy desired. Other considerations also apply to the design of multi-IMU navigation systems such as the computational bandwidth and storage to be able to collect the additional data from the added sensors plays a significant factor in the number of sensors that can be added. In addition, the computational time to achieve a positional solution may be unfeasible for the intended applications. Space constraints may also be another factor in the design of a multi-IMU system as the constraint for lower C-SWAP may be based on limitations in the platform size.

5.2 Limitations

Although the Multi-IMU fusion method provides results on par with a higher grade IMU there are limitations of the fusion method. The first limitation is that there is an exponential decay in the benefits added with each additional IMU. In general, the accuracy of the position solution does not continually increase as more IMUs are added. In addition, the benefits gained in C-SWAP are minimized with the addition of each sensor. As a result, the positional accuracy desired may require several sensors that negate the benefits gained in C-SWAP. As a result, a trade-off between C-SWAP and accuracy exists when using lower grade IMUs that require a significantly large number of sensors in order to achieve the desired positional accuracy.

Furthermore, the addition of more sensors equates to a proportional increase in processing complexity required to obtain a positional estimate. The implemented algorithm utilizes the particle filter to fuse the GPS measurements with the each IMU. As a result, a complete particle filter implementation is added with each additional IMU. In addition to the additional particle filter, the weight for each additional sensor is required to be calculated based on the GPS measurement. The additional weight calculation proportionally increases the computation required for the SIR step.

Another limitation is the weights for each sensor are calculated based on the GPS measurements received. This causes the weights to be reliant on the accuracy of the GPS measurement and assumes that the GPS measurement is highly accurate. As a result, the accuracy of the state estimation is limited by the accuracy of the GPS measurements. In a scenario where the GPS measurements are highly inaccurate, the IMU weights are calculated from the erroneous measurement and result in IMUs that are proportionally inaccurate based on the GPS are sampled more during the

SIR step. This equates to the final state estimation because the basis on which the final particle cloud is used to estimate the state contains inaccuracies that are biased towards the GPS measurements.

5.3 Simulations

To validate the proposed algorithm's ability to accurately estimate position, two three-dimensional paths of a navigating body are simulated. The first simulated path is calculated using

$$\begin{bmatrix} x \\ y \\ z \end{bmatrix} = \begin{bmatrix} \frac{1}{10}t\cos\left(\frac{1}{4}t\right) \\ 10t\sin\left(\frac{1}{5}t\right) \\ 10t \end{bmatrix} \tag{5.21}$$

and is shown in Fig. 5.4. The sensor measurements of the path are simulated by corrupting the position with three different sets of randomly generated Gaussian noise with standard deviations shown in Table 5.1. The calculated error between the algorithm's estimated position and the actual simulated path of each sensor is shown in Fig. 5.5 as a function of time. It should be noted that the error portrayed in Fig. 5.5 represents the error in position estimates of each sensor after using a particle filter. This simulation shows the process noise introduced by the particle filter as represented by the blue line. Each subsequent line shows the errors caused by having sensors with different variances after being processed by the particle filter. As expected, the sensor error is proportional to the variance of the sensor measurements. In other words, if a single sensor is to be used for position estimation (brute force method), an ultra-low bias sensor such as a navigational grade IMU should be used for best results.

Table 5.1: Noise standard deviation values for three different simulated sensors.

Sensor Number	**Noise Standard Deviation (m)**
1	0.50
2	1.00
3	0.10

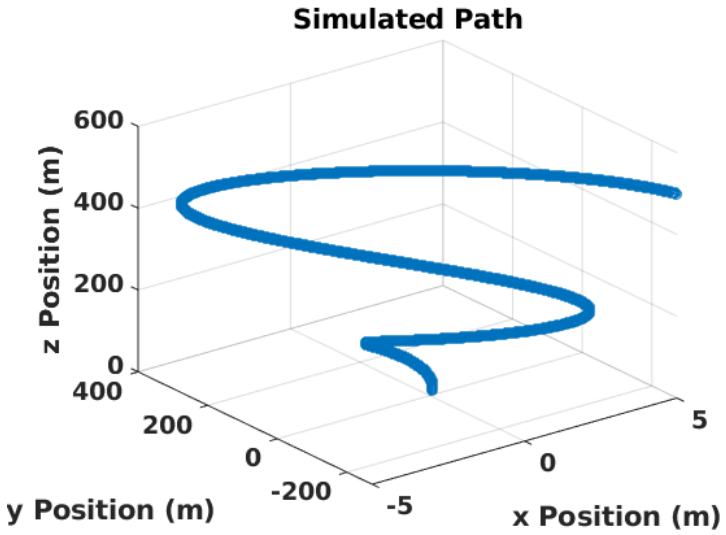

Figure 5.4: Simulated path of a navigating body. The acceleration values were calculated by calculating velocity in x, y, and z and then calculating acceleration.

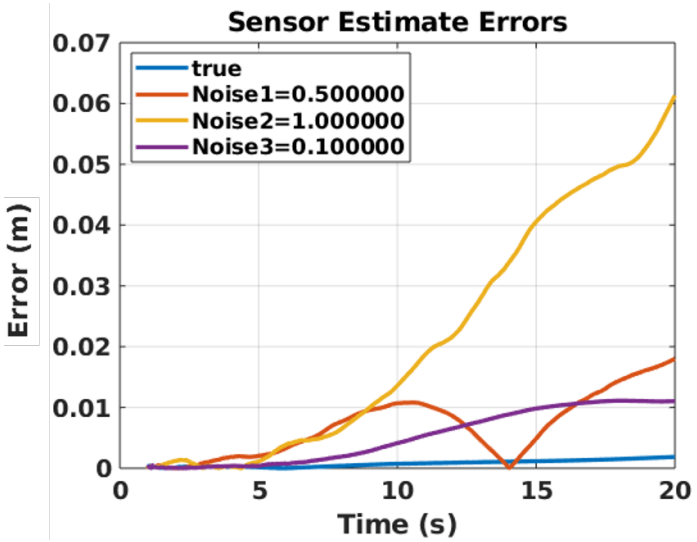

Figure 5.5: Root mean squared error of noisy sensor estimates. The blue line represents the output of the particle filter being fed with true sensor measurements. The other lines represent the output of the same particle filter being fed with noisy sensor measurements with different noise variations.

5.4 IMU Simulations

The proposed fine resolution position estimation algorithms are evaluated against simulated GPS and IMU measurements to validate the concept. The simulation

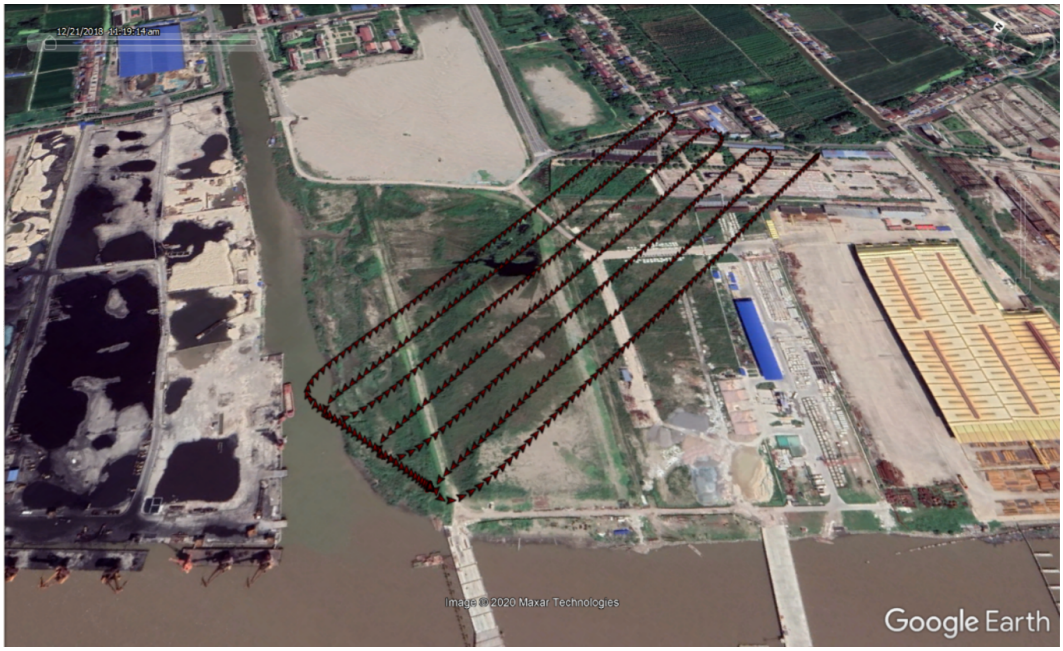

Figure 5.6: Graphical overlay of the flight path simulated by Acienna. The path included an initial rise to altitude and then has several switchbacks. This path is simulated based on a series of defined change rates and duration values. This map was obtained using Google Earth.

Table 5.2: NovAtel IMU-ISA-100C Specifications

Parameter	**Value**
Gyro Bias	0.0 deg/hr
Gyro Angle Random Walk	$0.012\ \mathrm{deg}/\sqrt{\mathrm{hr}}$
Gyro Bias Stability	0.5 deg/hr
Accelerometer Bias	$0.0\ \mathrm{m/s^2}$
Accelerometer Velocity Random Walk	$100\ \mu\mathrm{g}/\sqrt{\mathrm{hr}}$
Accelerometer Bias Stability	$1250\ \mu\mathrm{g}$

leveraged the open-source GNSS-INS-Simulator developed by Aceinna [1], and a path was simulated as shown in Fig. 5.6. The simulator also generated the truth and measured values for the gyroscope and accelerometer. Similarly, the simulator produces the true path and the measured GPS values for position and velocity. The simulator produced IMU measurements utilizing the characteristics of the NovAtel IMU and is shown in Table 5.2. The simulator also provided true attitude determi-

nations for each sample in time. The Kalman and the particle filter interpolation methods are applied to the measurements produced by the simulator and the accuracy of each method is calculated. Just like the NovAtel unit, the IMU acceleration values produced by the simulator are rotated using the matrix shown in (2.34) and processed in the NED coordinate frame. The results of the processed simulation values are shown in Fig 5.7 and show that the estimated path (est) closely follows

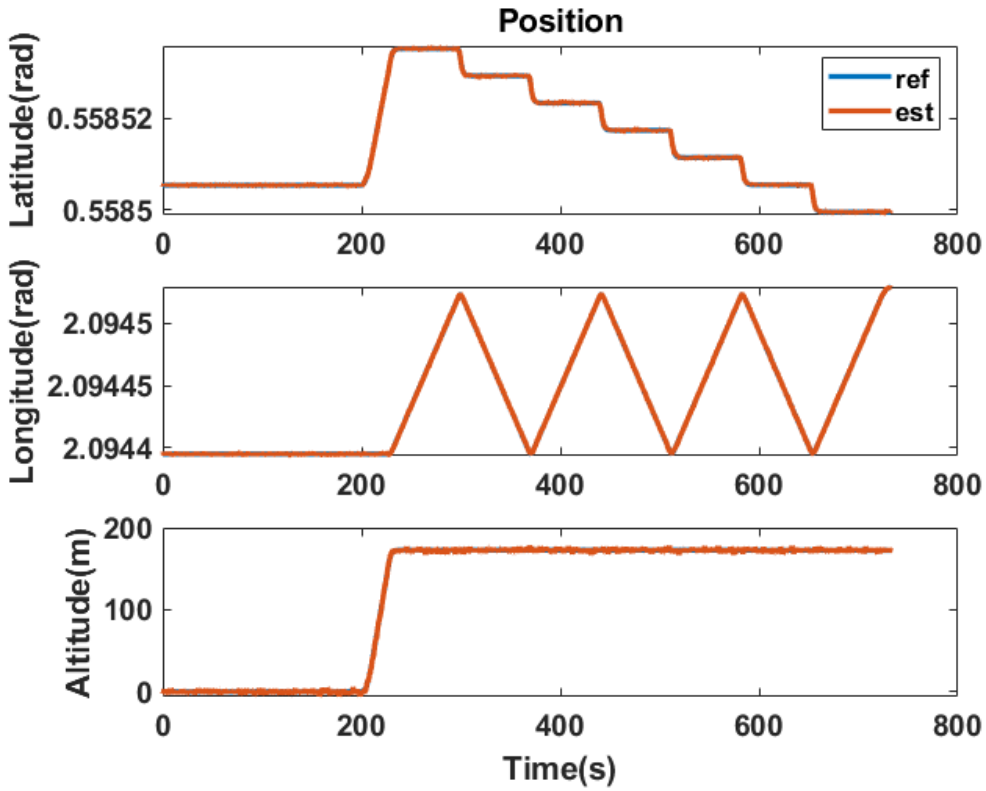

Figure 5.7: Results of simulated values. The results are produced using the simulated measured values. The reference path, shown in blue, is the true path generated by the simulator. The estimated path, shown in orange, is the path calculated by the algorithm.

the true path (ref) over an extended period.

A performance baseline for both the Kalman and particle filter method, without the proposed interpolation, are obtained using the simulated data values. As a result, the MSE of the longitude is shown in Fig.5.8 to illustrate the performance baseline

of the Kalman and particle filter independently. In the same way, the performance

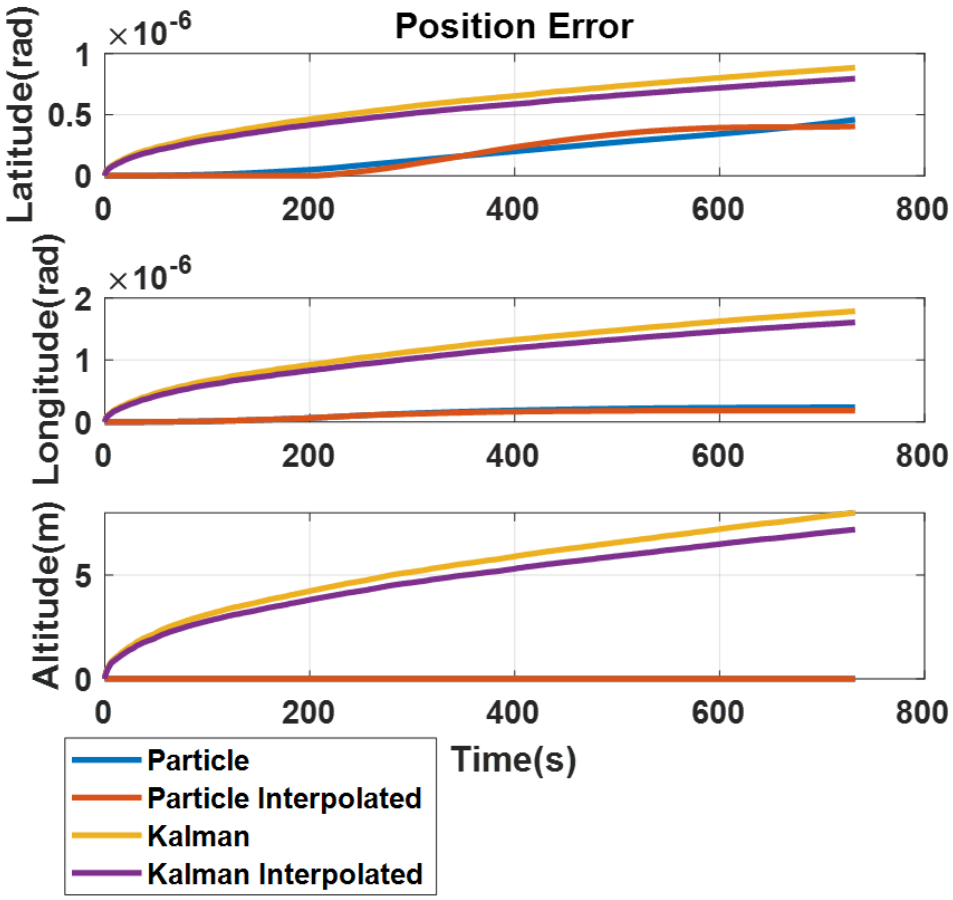

Figure 5.8: Latitude and longitude positional errors, in radians, and altitude errors in meters, of the simulated values without interpolation technique. The blue line shows the particle filter results compared to the simulated true path. The yellow line represents Kalman results compared with the simulated true path. The interpolated results for both particle and Kalman are shown in orange and purple respectively.

of the proposed interpolated Kalman and particle filter algorithms are obtained by using the same simulated data set and the longitude MSE is again calculated and shown in Fig. 5.8. It is readily seen that the particle filter outperforms the Kalman filter in terms of accuracy. Furthermore, the interpolated algorithm provides a slight increase in positional estimation accuracy; however, the major advantage here is the increased temporal resolution of the interpolated output. It should be noted that

the particle filter does require an increase in computational complexity and thus processing time. The focus of this paper is on maximizing the accuracy of the computed results while increasing the temporal resolution of the output; therefore, the in-depth computational requirements are left for future evaluation.

For quick reference though, the implemented algorithm performance times are noted in Table 5.3. These performance times indicate that the particle filter does

Table 5.3: Performance of implemented algorithms

Algorithm	**Time for 1 iteration**
Kalman	0.1 ms
Kalman Interpolated	0.1 ms
Particle	0.5 ms
Particle Interpolated	0.5 ms

require an additional computational burden. The times reported are for a single time step and can be used to approximate the total execution time for data of arbitrary lengths. It should be noted that the implemented algorithms were written in MATLAB and are not optimized for performance; thus, the reported times are a testament, not to the implemented algorithms not the true performance that can be achieved with optimized algorithms. In addition, for this initial study, the position estimates are not required to be done in real-time and therefore the implemented algorithms are used to post-process collected data from the IMU easing. Overall, the simulated IMU values give promising results for the interpolated Kalman and particle filter algorithms. These results show that the interpolation method will produce fine resolution position estimations at the rates required for SAR applications.

5.5 Multi-IMU Simulations

In order to emulate a more realistic navigation scenario, the second path is shown in Fig. 5.9, simulated using three IMUs integrated with a GPS solution. The

Table 5.4: Analog Devices ADIS16465 Specifications

Parameter	**Value**
Gyro Bias	0.0 deg/hr
Gyro Angle Random Walk	0.15 deg/$\sqrt{\text{hr}}$
Gyro Bias Stability	2.0 deg/hr
Accelerometer Bias	0.0 m/s^2
Accelerometer Velocity Random Walk	0.012 m/s/$\sqrt{\text{hr}}$
Accelerometer Bias Stability	$3.6e^{-3}$ m/s^2

IMU parameters used to simulate the scenario are derived from the Analog Devices ADIS16465 precision IMU are specified in Table 5.4.

For this simulation, each particle filter was initialized to the starting position and velocity of the navigating body with the variance of the particle cloud equal to the uncertainties of the Analog Devices IMU. These uncertainties are derived from the IMU specifications. Each IMU measurement is transformed into the local navigation frame (North, East, and Down) using measured gyro angular rotation rates. In addition, acceleration values from the IMUs were used to resolve the velocity of the body in the local navigation frame. The velocity was then used to update the position in geodetic coordinates (latitude, longitude, and altitude). The error between the algorithm's predicted position based on defined IMU characteristics and the actual simulated path is calculated for each sensor independently and is shown in Fig. 5.10 as a function of time. Note that the three IMUs used in this simulation had the same noise and biasing characteristics, but yielded different error values. This shows that the inaccuracies of an IMU are not deterministic even if the IMU specs are the same. Therefore, the individual IMUs can be treated as independent samples, which is required by the fusion algorithm. The positions are resolved using a particle filter fused with simulated GPS measurements.

As previously mentioned, the errors in the estimated positions from sensors with the same specifications are different. Each IMU produces statistically independent

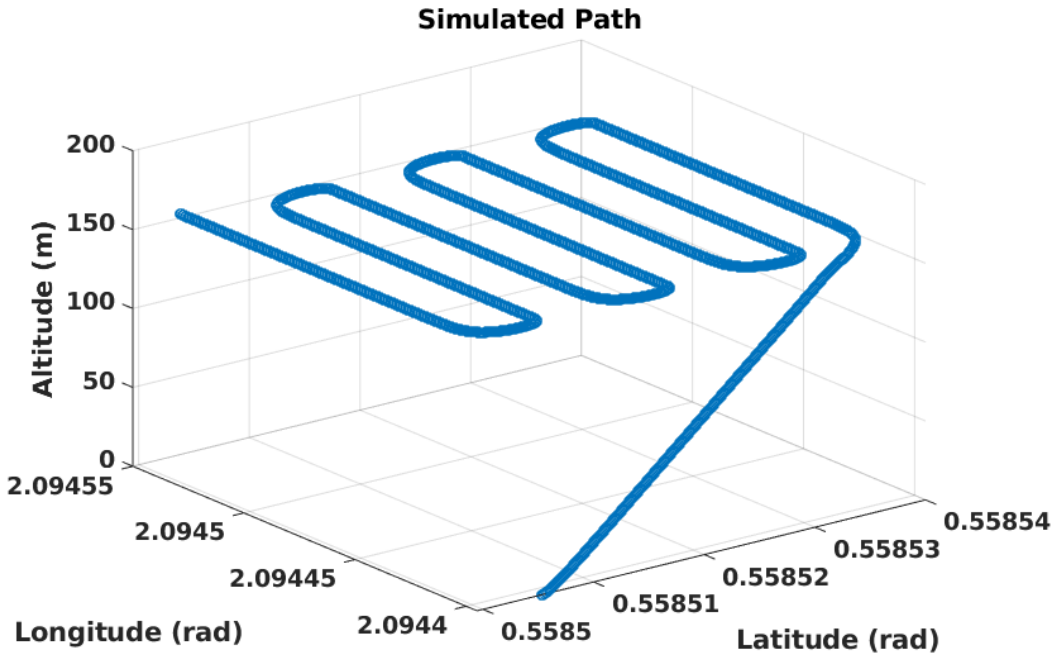

Figure 5.9: Simulated path for the three IMU scenario. The path is generated using Acienna's gnss-ins-sim python library. This path simulates a more complex path that has changes in latitude, longitude, and altitude. The python library simulates the gyroscope measurements as well as the accelerometer measurements to fully simulate measurements from an IMU.

samples of the position of the navigating body. Therefore, these statistically independent samples are much like the particles in a particle filter and can be re-sampled like those in a particle filter to converge on the true position. Each traditional particle filter result is fused using the proposed algorithm and compared to the truth positions pulled directly from the simulated path.

$$error = \sqrt{\frac{1}{N}\sum_{i=1}^{N}(x_i(k) - x_t(k))^2}\ , \tag{5.22}$$

where $x_i(k)$ are the particles at state k and $x_t(k)$ is the simulated true path with no noise corruption at state k. In the previous section, two different flight paths are de-

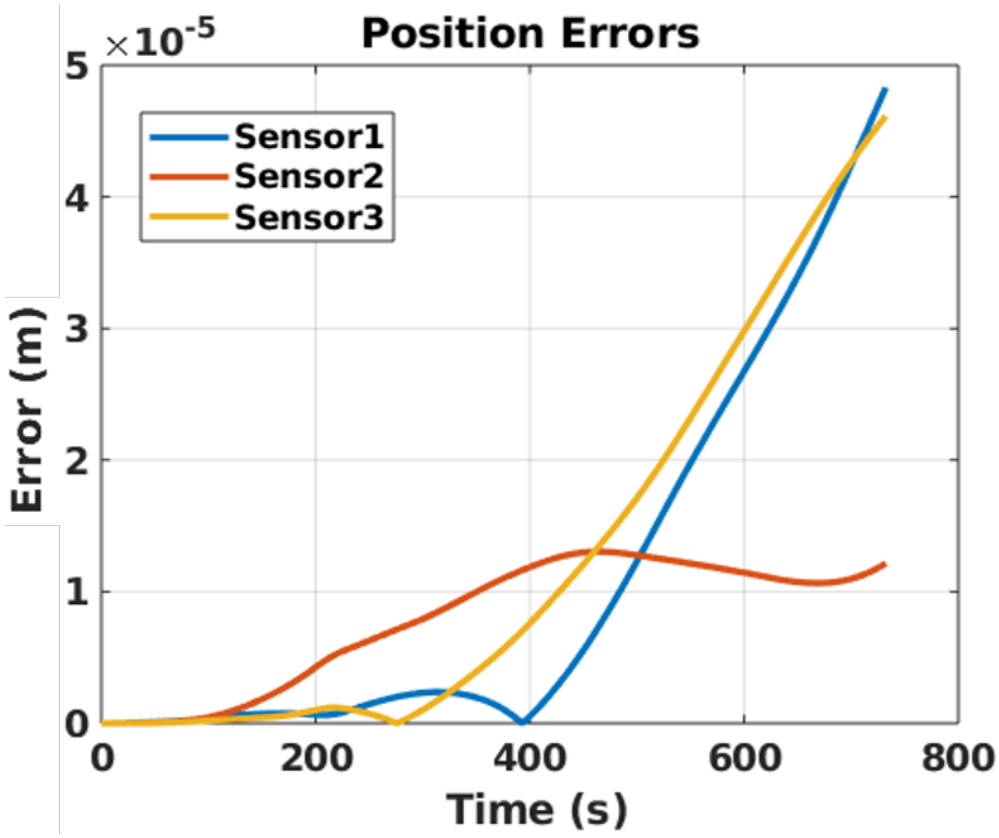

Figure 5.10: Mean squared error of three ADIS16465 sensor simulations.

fined and individual sensor capabilities to estimate position are investigated. Here, the individual sensor results, for each simulated path respectively, are fused using the proposed algorithm. The error is calculated between the simulated ”truth” position and the estimated position from the proposed fusion algorithm. Furthermore, the same error calculation is done with the position estimations from a ”traditional” fusion method of taking a normal average of the multiple sensor estimations. This not only allows a direct comparison of the enhanced positional estimation between the proposed algorithm compared to individual sensor estimations but also allows a direct comparison between the proposed algorithm and a more traditional averaging fusion method as disclosed in [31].

The error of the traditional and proposed fusion method is shown in Fig. 5.11

for the first simulated path and associated sensors. Note that the traditional fusion provides a substantial reduction in positional error compared to Fig. 5.5, as to be expected, but the proposed fusion method is approximately three times more accurate than the traditional method. The same comparison is shown in Fig. 5.12 for the second simulated flight path and the associated Analog Devices IMUs. Again, there is a significant reduction in error using a traditional fusion method (almost five times reduction), but the proposed fusion algorithm provides approximately an additional two times improvement. Based on the results in Fig. 5.11 and Fig. 5.12 , the proposed fusion algorithm is shown to provide excellent position estimations of a navigating body compared to individual sensor capabilities and traditional averaging fusion algorithms. The error calculated between the proposed method and the traditional method highlights the performance differences of each method.

Given the proposed algorithms´ excellent ability to estimate position, the final task is to compare the performance between a single navigational grade IMU and the fused output of the three precision MEMS grade Analog Devices IMU modules. Given the increased C-SWAP of navigational grade IMUs, their usability in C-SWAP constrained environments, such as airborne platforms, is drastically limited. Therefore, the position, navigation, and timing (PNT) module could be greatly limited in these situations to smaller, lower quality IMU modules. However, the position estimation accuracy of the system will more than likely need to be maintained albeit these constraints, and the use of multiple reduced C-SWAP (quality) IMUs with the proposed fusion algorithm could be an ideal solution.

The navigational grade IMU chosen for this comparison is the NovAtel IMU-ISA-100C and its specifications are shown in Table 5.2. While the biasing and error characteristics of the NovAtel unit are significantly smaller, the unit has an increased order of magnitude in cost, size, and power consumption and is three

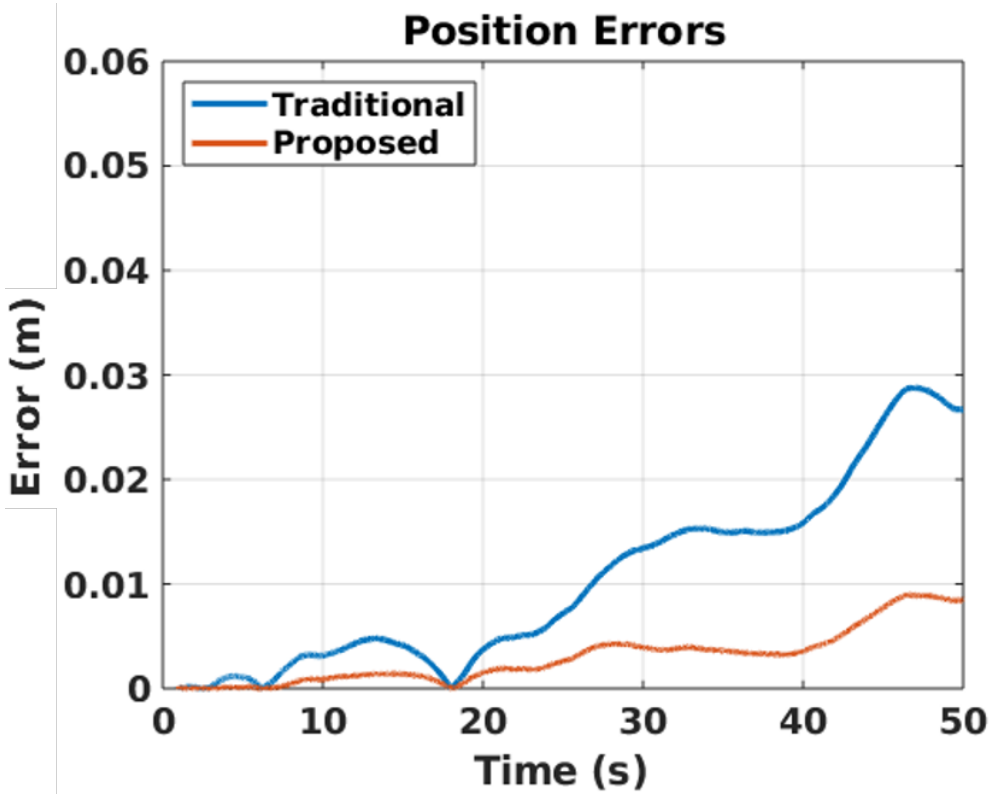

Figure 5.11: Error of both algorithms calculated by (5.22). The blue line is the traditional method of taking the mean and the red line shows the results for the SIR method of fusing multiple IMUs.

and a half times heavier compared to the multi-IMU solution with three Analog Devices IMUs. Therefore, it is clear that there is a C-SWAP vs. performance trade-off between the different position, navigation, timing (PNT) solutions.

The second flight path is simulated with the single NovAtel IMU and a GPS solution, and the data from each are fused with a particle filter to yield the estimated position. Next, the positional error between the simulated true path and the estimated path by the fused GPS/navigational grade IMU is calculated as a function of time and shown in Fig.5.13. The error for a single ADIS16465 and three ADIS16465 IMUs are shown as well. The single navigational grade IMU (NovAtel) has a lower error when compared to the precision MEMS grade Analog Devices

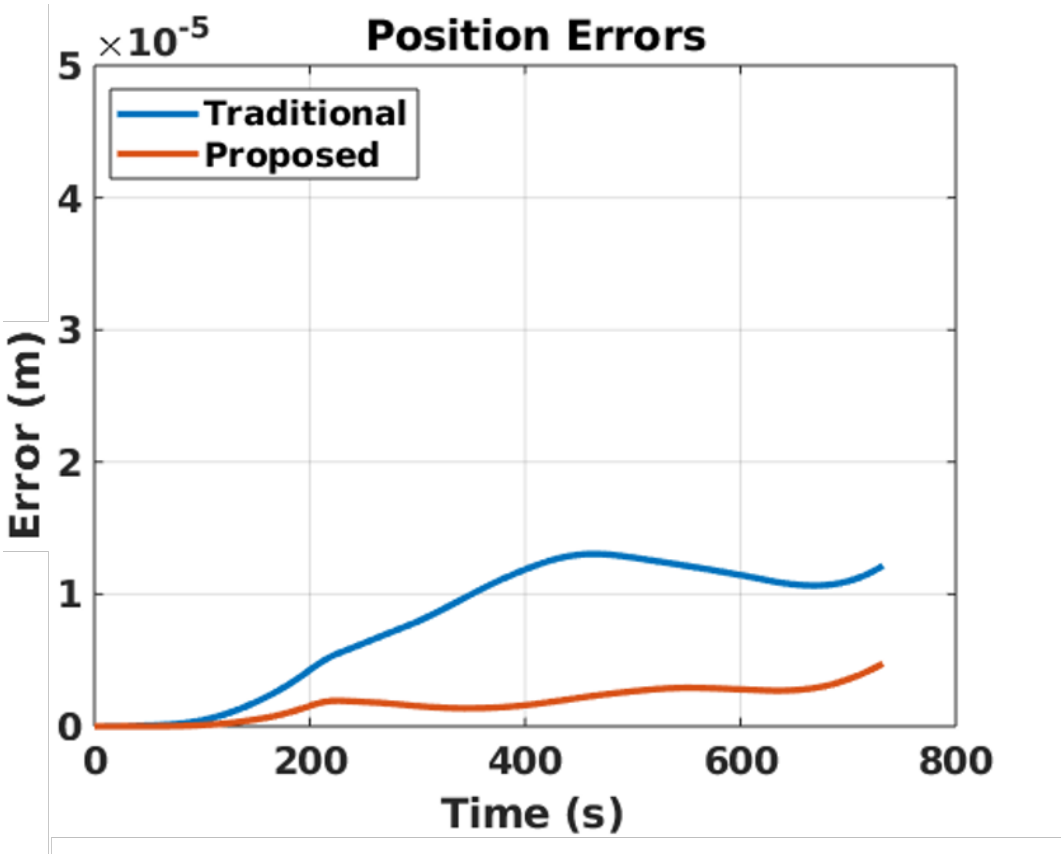

Figure 5.12: Error of the three IMU scenario calculated by (5.22). The blue line represents the traditional method of taking the mean and the red line shows the results for the SIR method of fusing multiple IMUs.

IMU. However, the three ADIS16465 IMU fused solution results in an error that is on par with the NovAtel unit. This indicates that a highly precise PNT solution can indeed be achieved by fusing multiple lower grade IMUs using the proposed fusion algorithm.

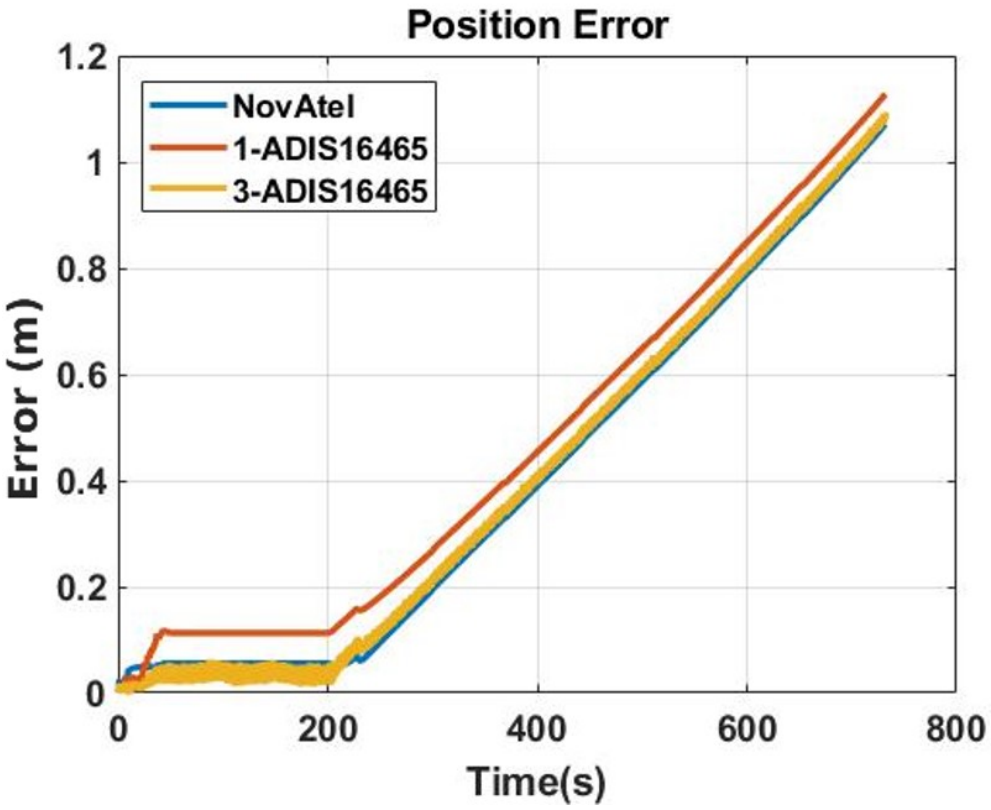

Figure 5.13: Error of NovAtel unit compared to the ADIS16465 IMUs calculated by (5.22). The blue line represents the NovAtel unit and the red line represents the ADIS16465 position solution. The yellow line represents the 3 ADIS16465 IMUs fused using the proposed method.

5.6 Instrumentation

The system obtained is the NovAtel Synchronous Position, Attitude and Navigation (SPAN) IMU-ISA-100C system utilizing the ProPak6™ interface shown in Fig. 5.14. The system provides a GPS position at a rate of 20 Hz and an IMU measurement at a rate of 200 Hz. The system is comprised of a ProPak6™ receiver, a GPS antenna, and the IMU unit. The system contains a high-performance IMU that utilizes low noise optical gyroscopes and Micro-Electro-Mechanical Systems (MEMS) accelerometers. The ProPack6 receiver allows for the user to connect via

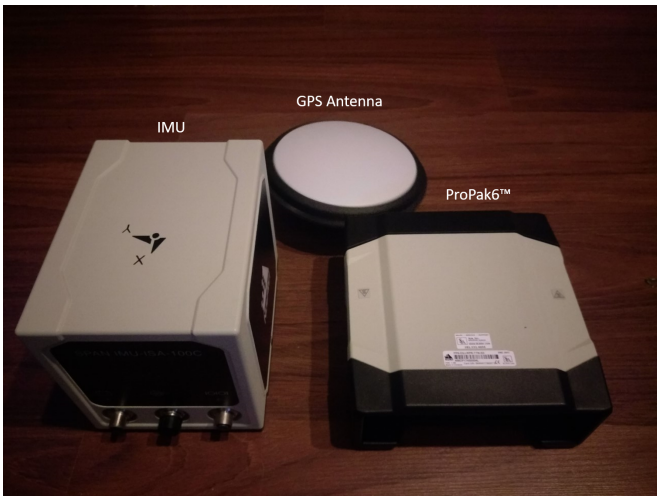

Figure 5.14: The NovAtel SPAN System

an Ethernet cable. The user can then use the NovAtel connect application to control and configure the system for data capture. The application allows a user to monitor the GPS satellite constellation as well as signal strength along with other diagnostics information. The user can also configure what logs are saved to the disk. The logs contain a variety of different information pertaining to GPS and IMU measurements. In addition, the NovAtel connect application provides flexibility in what information is logged. The logs chosen contained the navigation body's latitude, longitude, and altitude from the GPS sensor. In addition, the accelerometer

and gyroscope readings were recorded. Each log entry from both sensors is marked by a GPS timestamp. The final log was encoded as ASCII and saved as a text file. The file was then parsed into a table with columns containing: the GPS timestamp, latitude, longitude, height, accelerometer, and gyroscope data.

The NovAtel Span system was instrumented on a vehicle and driven around Oklahoma City, Oklahoma. The GPS antenna was mounted in an open sunroof and the IMU was placed near the center of the vehicle. The ProPak6™ unit was placed in the passenger seat of the vehicle. The ProPak6™ unit was connected via an Ethernet crossover cable to a laptop that recorded the data. The drive took roughly 30 minutes and included stopping at stoplights as well as highway travel. The path taken is shown in Fig.5.15 where the latitude, longitude, and height have been converted to the earth-centered earth fixed Cartesian representation of the positions.

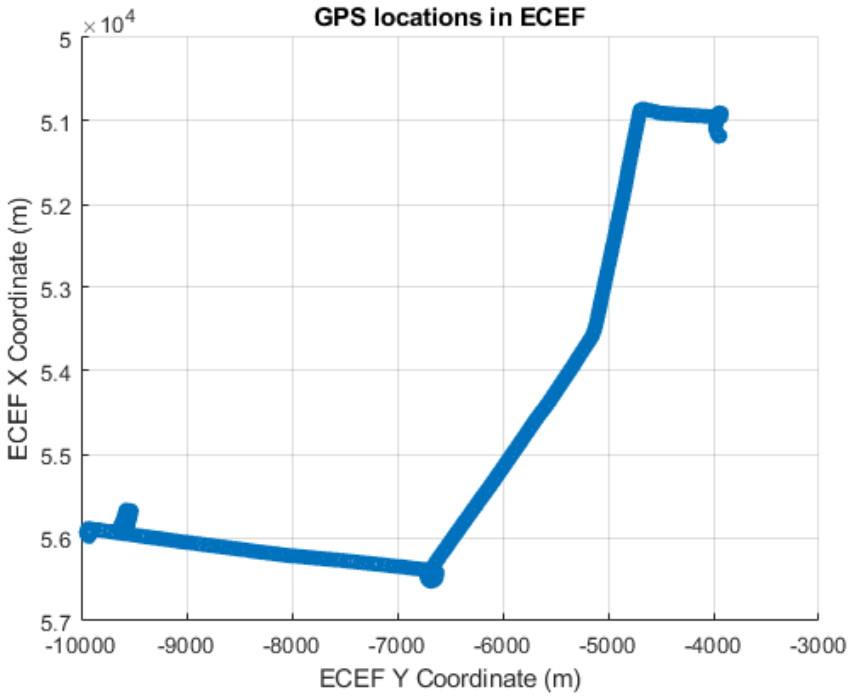

Figure 5.15: Route taken in ECEF Cartesian coordinates

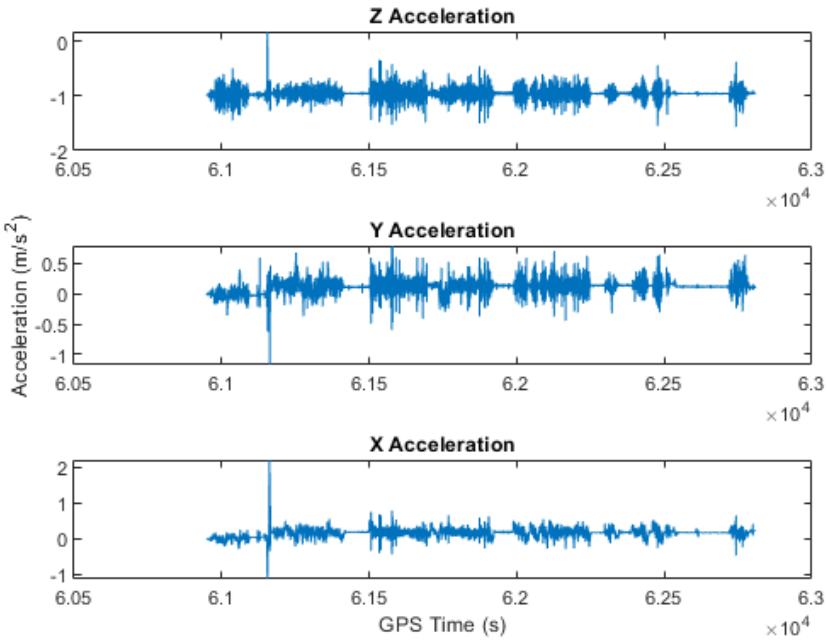

Figure 5.16: IMU Acceleration values

The accelerometer values measured from the route taken are shown in Fig.5.16. Validating the proposed up-sampled algorithms in simulations is crucial since the simulator provides an absolute "truth" position that allows for mathematical comparisons to the algorithm's estimated positions. However, it is also crucial to validate the fusion method in an actual instrumented test setup. The NovAtel Span system is instrumented on a vehicle and driven around Oklahoma City, Oklahoma where the GPS antenna was mounted in an open sunroof and the IMU was placed near the center of the vehicle. The ProPak6™ unit was placed in the center console of the vehicle and connected via an Ethernet crossover cable to a laptop that recorded the data. The NovAtel system performs a kinematic alignment to initialize the orientation of the IMU. The kinematic alignment method uses the GPS velocity vector to determine the heading. For the implemented algorithms, the heading was

initialized to true north. This was achieved by turning the vehicle until the NovAtel GUI indicated that the vehicle was facing north and the kinematic alignment was initiated. Data for the traversed path was only captured after the alignment and initialization process was complete. The paths were then processed with both the Kalman and particle filters, with and without the interpolation method proposed, and are shown in the following subsections. In general, the path taken is shown in Fig. 5.17 as geodetic coordinates overlaid on a Google Earth image.

Figure 5.17: Route taken in geodetic coordinates. The path is a low-speed drive around a neighborhood. The distance traveled is half a mile. This map was obtained using Google Earth.

Measuring the performance of the instrumented system is more difficult than the method used in the simulated results as the absolute true path is not captured. While GPS could be used as the "truth" path traversed, GPS itself has some inherent noise (position error) that would bias the calculated MSE. In order to remedy this

issue and evaluate the accuracy of the algorithms, a real time kinematic (RTK) differential GPS with centimeter accuracy instrumented with the NovAtel system was used. The RTK system is the ArduSimple simpleRTK2B kit and consisted of a base station and a rover receiver. The system is capable of producing cm-level position solutions. The base station was stationary and communicates with the rover receiver using a pair of Xbee radio transceivers. In addition, the base station is then set up prior to the test to allow for the system to determine an accurate location of the base station. The algorithmś position results are compared to the RTK collected path. The MSE of each algorithm compared to the RTK solution is calculated and shown in Fig. 5.18. The implemented particle filter produced results that were closer to the RTK's cm-level accuracy than the implemented Kalman filter. To show the performance of the up-sampled algorithms, the estimated paths are overlay-ed on Google Earth images and shown in the next two subsections.

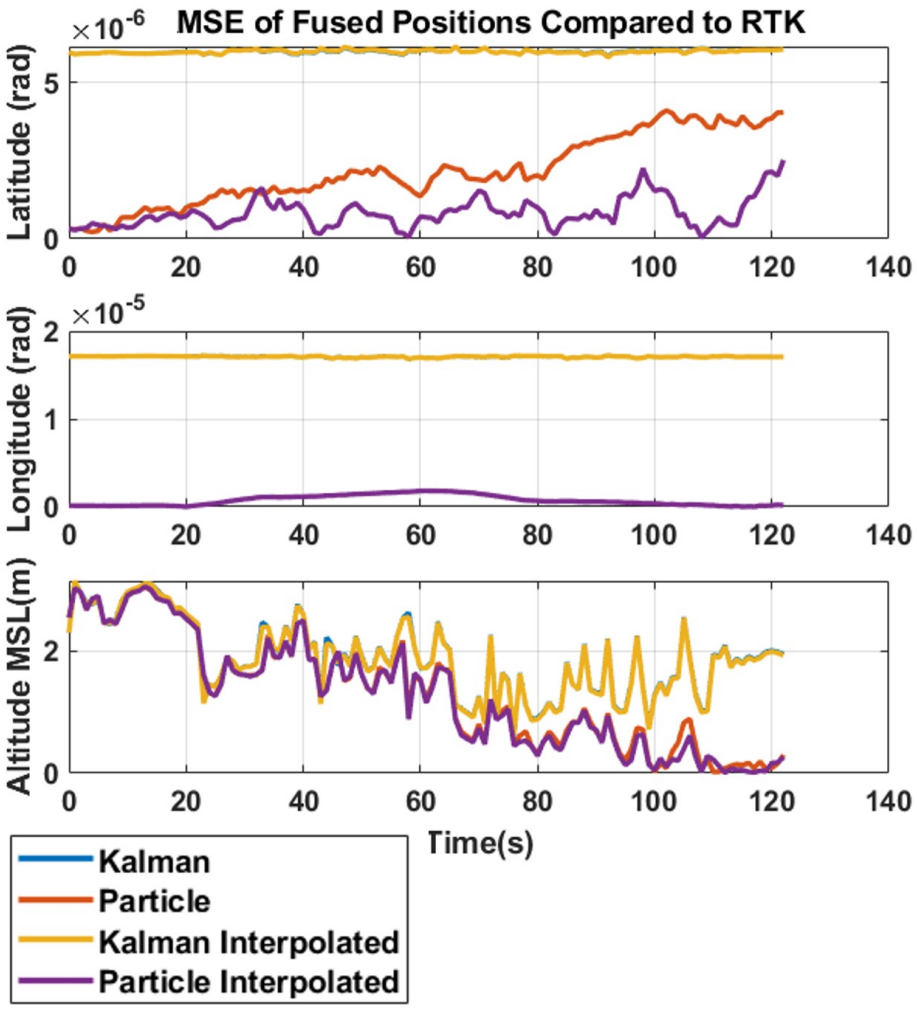

Figure 5.18: MSE of the particle filter and Kalman filter compared to RTK GPS.

5.7 Kalman Results

The instrumented data are processed using both the regular Kalman filter and the interpolated Kalman filter. The results from both algorithms are shown in Fig. 5.19. The results show that the algorithm accurately predicts position given the acceleration measured by the IMU. The fine resolution method described in Section

3.3 produced position estimates at a higher frequency than the output of the GPS and IMU. More specifically, the algorithm up-sampled the 200 Hz update rate of the IMU to a faster rate of 3 kHz, or 15 times faster providing 15 times the temporal resolution. Furthermore, the higher frequency positions agree with the values produced by the NovAtel system as well as the GPS coordinates and did not introduce additional errors when producing higher frequency position estimations. By using a Kalman filter to fuse sensor positions with the up-sampled predictions, the algorithm preserves the benefits of drift correction provided by the Kalman filter while providing faster position updates. Furthermore, the positional solution provided is based on measured physical state changes in the navigational body. As a result, the interpolation captures behavior of the system that is not apparent to traditional polynomial interpolation techniques.

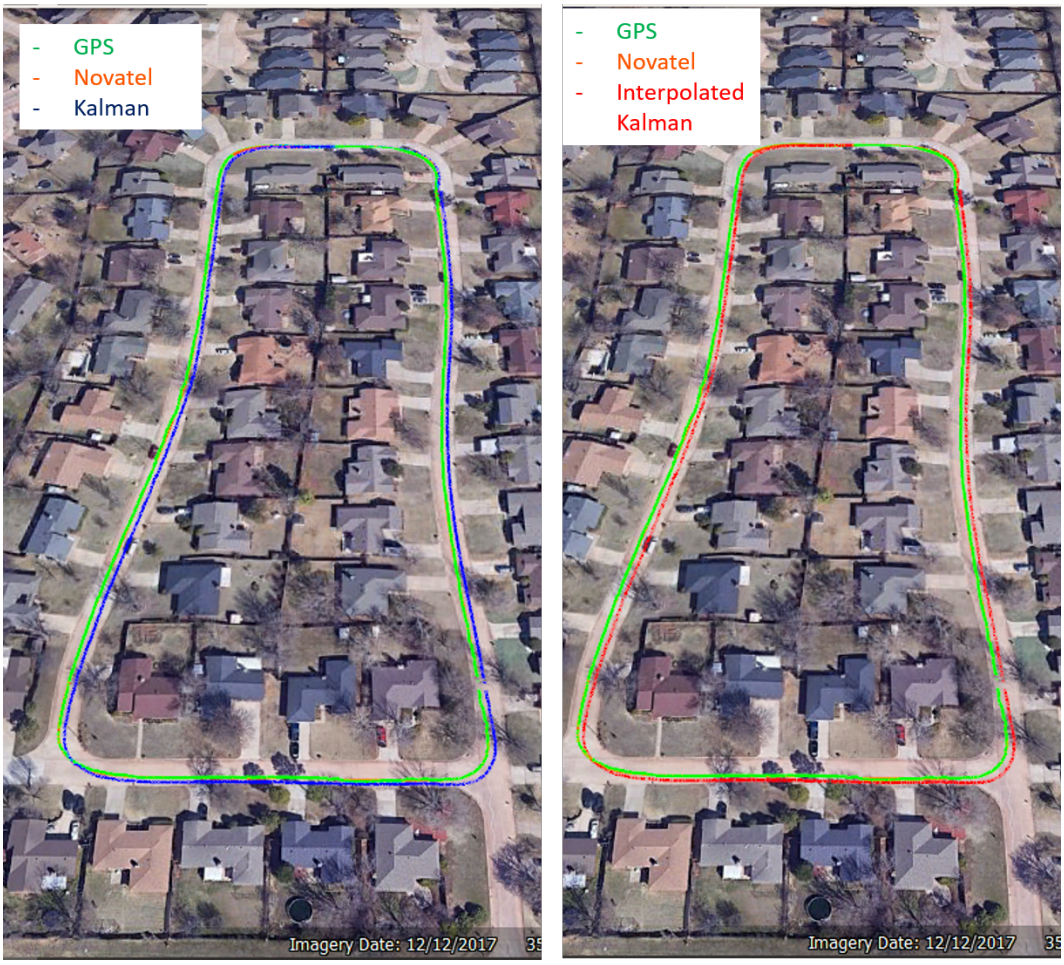

Figure 5.19: Kalman algorithm results. The left image shows the Kalman results plotted on top of the GPS coordinates and the navigation solution given by the NovAtel system. The right image shows the Kalman interpolated results plotted on top of GPS and NovAtel coordinates. These maps are obtained using Google Earth.

5.8 UPF Results

Similar to the interpolation results obtained by the upsampled Kalman filter, the same data collected from the instrumented NovAtel system is processed using the presented UPF method. The results of the UPF are plotted on top of the GPS measurements and shown in Fig. 5.20.

Figure 5.20: Results of the GPS positions and the results of particle filter algorithms. These maps were obtained using Google Earth.

The particle filter provided a similar solution to the Kalman method and, in general, the position estimates are accurate and aligned with the GPS measurements. The proposed normal distribution is sufficient in allowing the particle filter to converge on the GPS measured values. The results of the particle filter presented utilized a particle cloud with 2×10^3 samples and are resampled based on the method described in Section 3.2. The evolution of the particle cloud distribution over time is shown in Fig. 5.21.

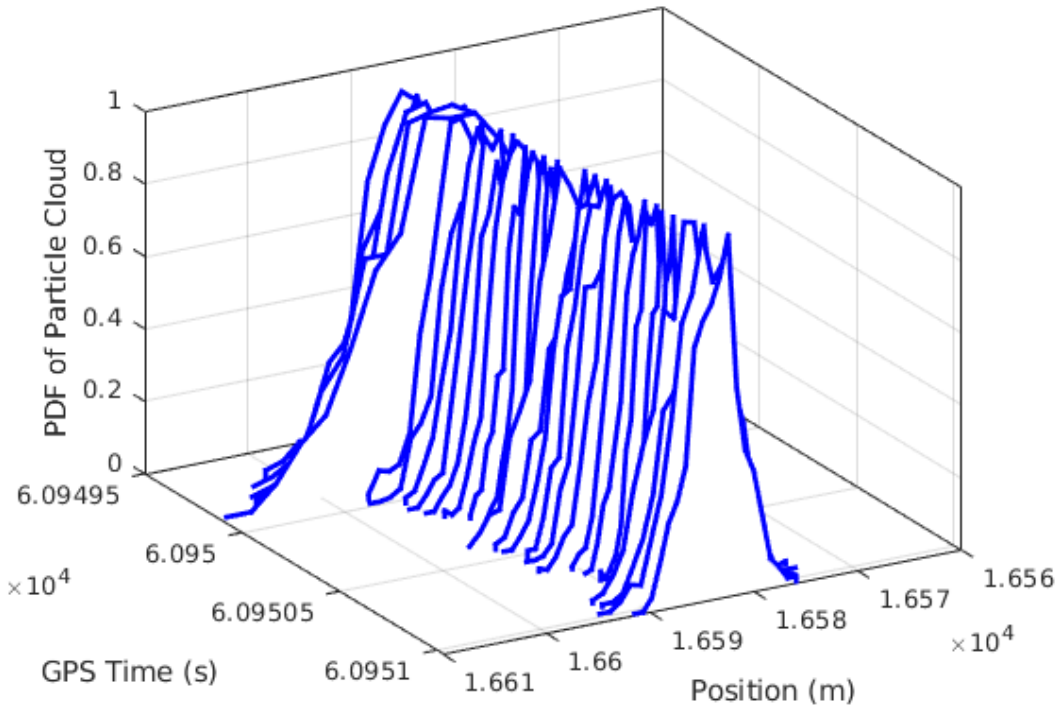

Figure 5.21: PDF evolution of the particle filter over time. The variance of the particle cloud distribution shrinks with every resample of the cloud. As a result, the cloud converges to an answer closer and closer to the true value.

Notice that the distribution of the particle cloud initially has a large variance, but as the particle filter transitions in states and is resampled, the variance of the particle cloud decreases. As the variance decreases, the mean of the particle cloud becomes more accurate and can be used as a more accurate estimated position at each time step. The particle filter is also modified to produce finer resolution position estimates, as described in Section 3.5, which successfully up-sampled the temporal resolution to 3 kHz providing position estimates 15 times faster than the IMU sampling speed.

5.9 Muti-IMU

The multi-IMU method is verified by using the same radar configuration and a similar ground experiment to the one shown in Fig. 6.4. The multi-IMU system with the ARENA control and timing unit (CTU) is instrumented directly on the NovAtel system to directly compare the images focused by each navigational solution. The ARENA CTU is utilized to capture the data from each of the low-grade IMUs. In addition, the CTU provides a timestamp for each of the captured IMU measurements. Each IMU is connected to the CTU by a ribbon cable the CTU provides the power and clock signal required by the IMUs. The measurements are streamed to the CTU via the Serial Peripheral Interface (SPI) communication protocol. As a result, the CTU is responsible for the data acquisition of the IMU data and is synonymous with the NovAtel receiver. In the instrumented setup, the IMUs were pre configured using the evaluation board compatible with the IMUs. The configuration uploaded allowed for an external clock to be utilized. A synchronous external clock is useful for attributing coherent timestamps to the measurements from the IMU. The coherent timestamps are crucial to the alignment of the data in the fusion algorithm and are described in chapter 3.3. Furthermore, the configuration set the sampling rate to 100 samples per second in order to prevent the CTU buffers from overflowing. An image of the instrumented multi-IMU system mounted on the NovAtel IMU is shown in Fig. 5.22. The NovAtel receiver and IMU are visibly larger than the multi-IMU system. As a result, the weight of the multi-IMU solution weighs significantly less than NovAtel IMU thus, decreasing the C-SWAP for the navigational system.

Figure 5.22: An image of the multi-IMU instrumentation setup. The gold box mounted on the NovAtel IMU is the ARENA CTU and the silver boxes with the ribbon cables are the 3 ADIS-16465 IMUs.

Similar to the NovAtel system, the multi-IMU is connected to a computer via Ethernet where the data from each IMU is buffered to respective files within the computer file system. The GPS measurements are recorded independently from the multi-IMU. As a result, the NovAtel GPS measurements are currently being used for both the multi-IMU solution and the NovAtel solution. Additionally, this allows for the errors caused by GPS to be the same for both solutions and allows for a more direct comparison between the multi-IMU alternative and the single high-quality IMU approach.

In order to validate the simulated results, an experiment deployed instrumenta-

tion of the NovAtel system and three ADIS 16465 to a vehicle. The vehicle drove through an urban environment and the results of the NovAtel system are directly compared to the fusion of the three ADIS IMUs using the proposed method. The instrumented system collects GPS latitude, longitude, and altitude from the NovAtel system. In addition, the angular velocities and acceleration values from the NovAtel IMU-ISA-100C is collected from the NovAtel synchronized position attitude navigation (SPAN) receiver. The angular velocities and acceleration values from each of the three IMUs are collected using a control and timing unit (CTU) from Remote Sensing Solutions (RSS). The data collected from each sensor is timestamped from the CTU and the NovAtel SPAN receiver. The data from the NovAtel IMU is fused with the NovAtel GPS data using the traditional particle filter fusion method. In addition, the experiment also utilizes a real-time kinematic (RTK) GPS with centimeter-level accuracy to capture the path the vehicle traverses. The RTK measurements are used as a highly accurate third-party ground truth of the path traversed in order to measure the accuracy performance of each IMU configuration.

For a fair comparison, the three ADIS IMUs are also fused with the NovAtel GPS measurements using the proposed fusion method. Fusing each IMU configuration with the same GPS measurements allows for the uncertainty of the GPS measurements to affect all the IMU configurations equally. As a result, the differences in errors from each of the IMU configurations are largely sourced by the errors from the IMU and the fusion method. Using Fig 5.13, the simulations showed three ADIS 16465 IMUs can provide comparable performance to the NovAtel IMU. The experiment is designed to confirm these results from the simulation and three ADIS 16465 is used for direct comparison with the NovAtel system. The path traversed by the system is shown in Fig. 5.23.

The results of the experiment for a single ADIS 16465, the NovAtel system,

and the three ADIS 16465 system is shown in Fig. 5.24. The results are compared to the RTK GPS and the error of each of the IMU configurations are calculated. From Fig. 5.24, it can be seen that the three IMU configuration performs the best followed by the NovAtel and the single ADIS configuration respectively. These results are expected as the NovAtel system is a more accurate sensor compared to the single ADIS 16465. Similarly, the NovAtel system and the ADIS start with similar accuracy but the single ADIS solution begins to ”walk” 20 seconds faster than the higher quality NovAtel. The 3 IMU configuration with the proposed fusion method improves the initial accuracy of the navigational solution and minimizes the walking effects of the sensors.

Figure 5.23: The urban path traversed by the deployed NovAtel and ADIS 16465 system. This image is a screenshot from Google Earth.

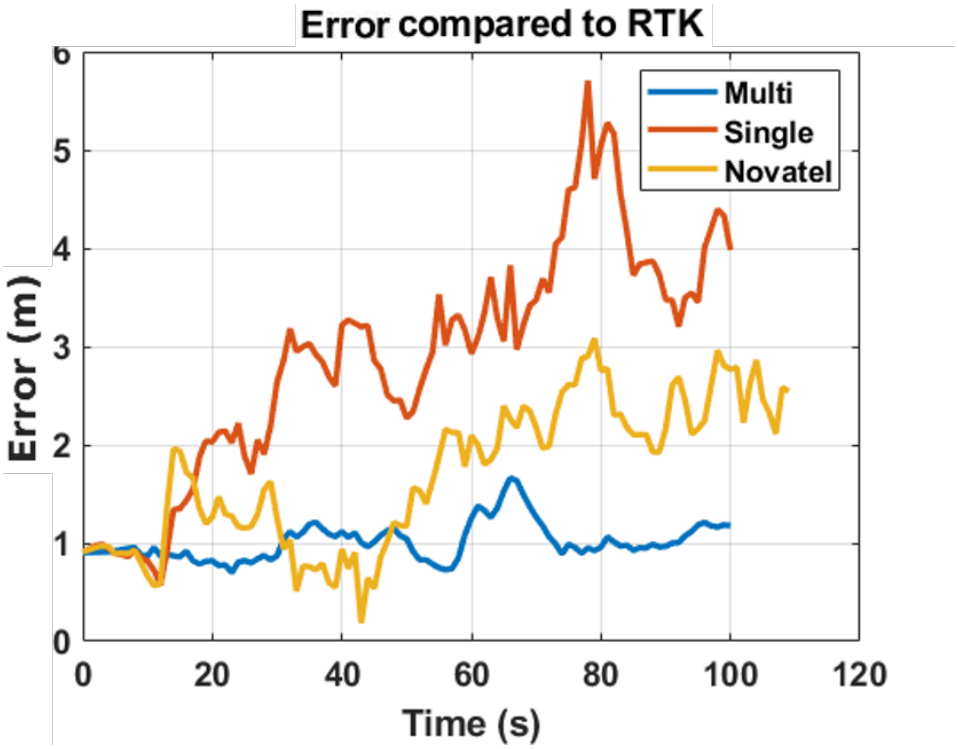

Figure 5.24: Error of 3-dimensional positional accuracy in meters. The blue line is the error of the fusion of 3 ADIS16465 IMUs. The red line is the error of a single ADIS16465 IMUs and the yellow line is the error of the NovAtel system.

5.10 Flight Test

In addition to ground-based testing, the NovAtel unit is instrumented within a small cargo bay of the Piper Warrior aircraft near its center of gravity, as shown in Fig. 2.4. The plane flew a test path, shown in Fig. 5.25, to evaluate the UPF algorithm on an airborne platform that possesses six degrees of freedom. The flight began in the upper-middle portion of the figure, then the aircraft flew in the southwest direction (lower-left portion). Next, the plane flew nearly due east and subsequently turned northeast. It executed a series of figure-eight maneuvers and racetrack maneuvers, then it finally flew in a northwest direction back to the airport. The duration of the flight was 3,591 seconds or approximately 1 hour. The path is selected since it included simple elevation maneuvers such as takeoff and landing, as well as more

complex maneuvers, such as figure-eights. The recorded flight path from the GPS unit (green curve) and the calculated position estimates of the UPF algorithm (red curve) are shown in Fig. 5.25.

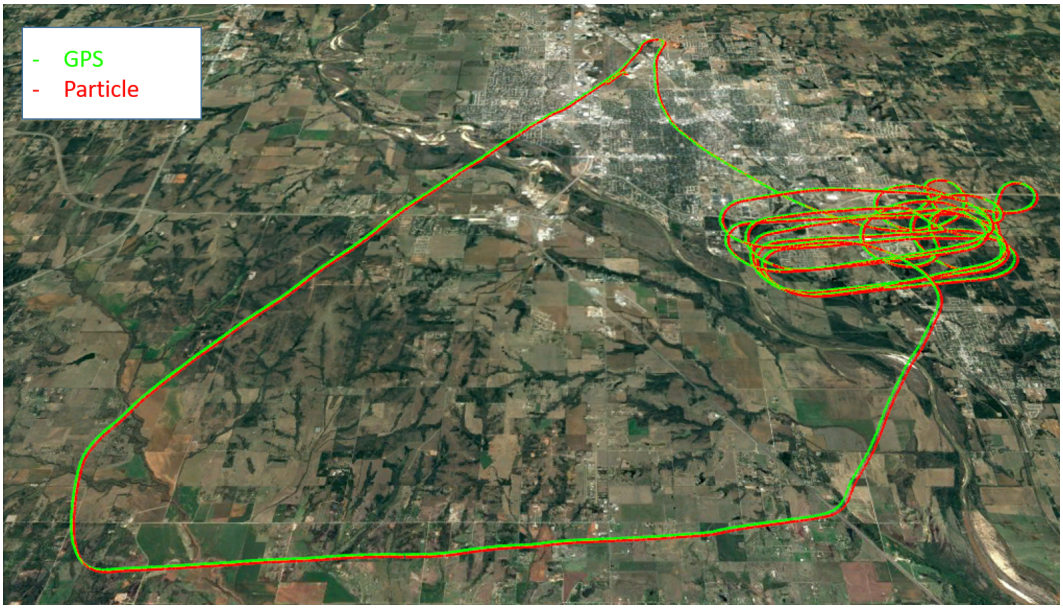

Figure 5.25: Map representation of GPS and UPF results of the flight path flown by the Piper Warrior aircraft. The green line represents the GPS measurements captured by the NovAtel unit. The red line represents the results of the proposed UPF algorithm. This map was obtained using Google Earth.

Fig. 5.26 depicts the normalized variance for the UPF cloud for the latitude, longitude, and altitude, respectively, versus time. The figure illustrates how the particle clouds for each of the position components decrease rapidly, which indicates a quick convergence to the optimal solution. The behavior of the variance is due to the re-sampling process which draws a new particle cloud based on the weights calculated by (3.22). These weights allowed for the unlikely particles to be removed from the cloud, which causes the variance to converge to the optimal solution.

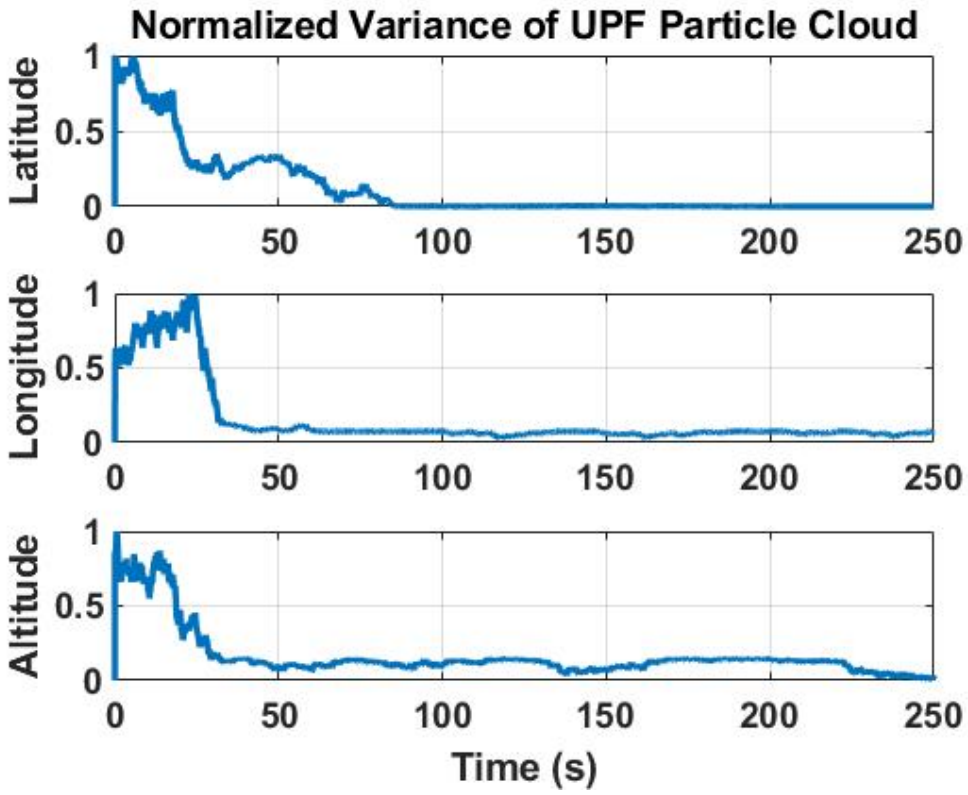

Figure 5.26: Variance of latitude, longitude, altitude particle clouds plotted against time. As shown, the variance of all three components converge to a solution. Each component was calculated from a particle cloud with 2000 particles.

Given that all particle filters converge rapidly (i.e. less than 75 seconds), the full flight can be studied. Consequently, Fig. 5.27 confirms that the proposed UPF algorithm functioned correctly since it tracked the GPS coordinates accurately from take-off to landing.

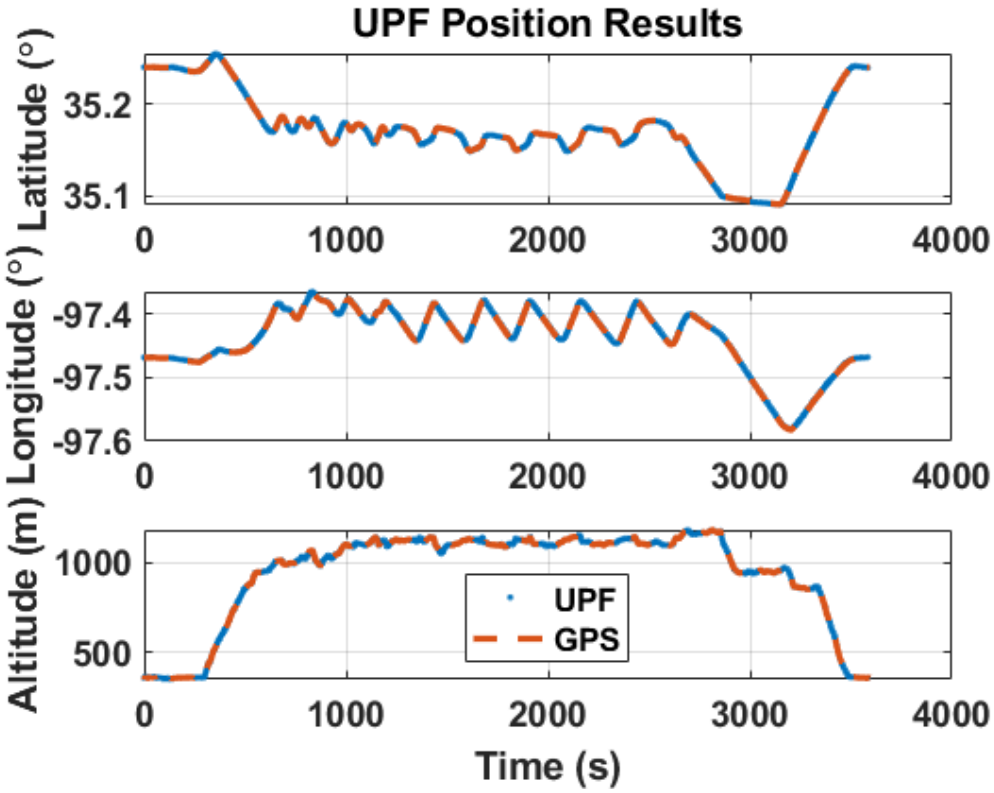

Figure 5.27: Latitude, longitude, and altitude of the flight test plotted against time. The UPF results are shown in blue and the GPS results are shown in orange. Total flight time was 3591 seconds.

Given the GPS measurements contain inherent errors, a direct error-level comparison is not warranted but was done to verify that the Euler rotation mathematics were implemented correctly to be able to accurately estimate the complex flight path flown. The calculation of the difference, or residuals, between GPS and the UPF algorithm can further confirm the algorithm functioned correctly and illustrate the algorithmś ability to track with GPS measurements. These residuals for each of the position components are shown in Fig. 5.28.

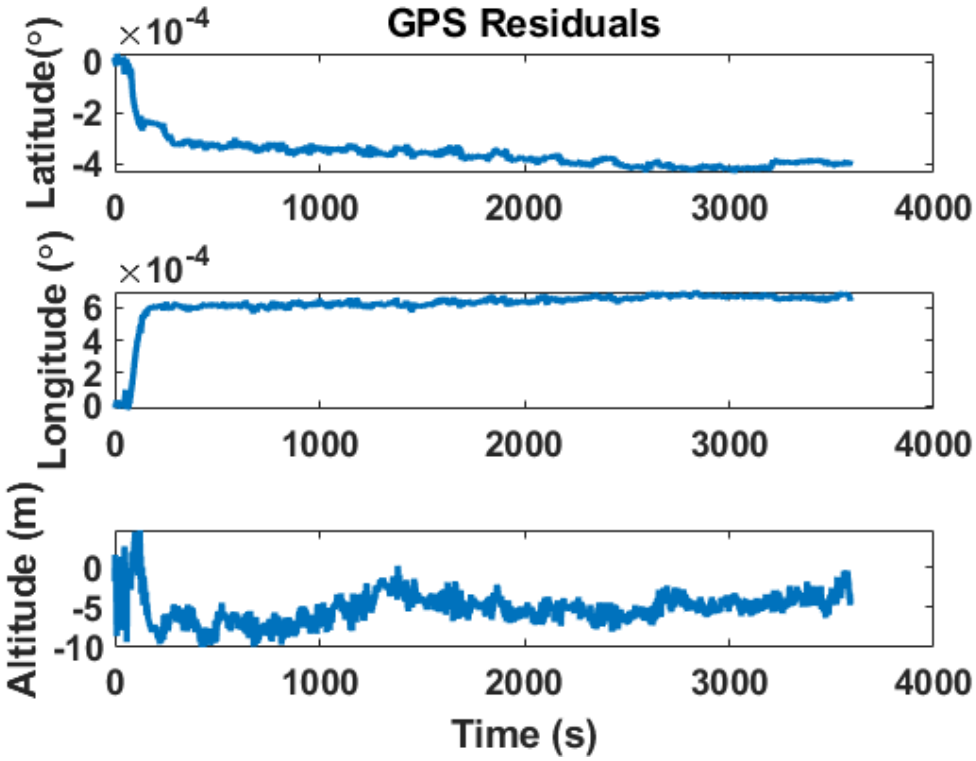

Figure 5.28: The residuals of the UPF position solutions compared to the GPS position solutions

5.11 Summary

In summary, this chapter presents an approach to miniaturizing the INS systems without compromising the accuracy of the positions provided. The technique requires leveraging the benefits of data fusion to obtain a higher accuracy solution and the use of multiple lower-quality IMUs. In doing so, lower C-SWAP sensors can be used to produce an INS system that is capable of providing accurate positional solutions capable for the SAR application.

Design tools to estimate the number of sensors to utilized in the technique is also described in this chapter. The tools allow for both a back of the envelope estimation of the number of sensors to utilize is presented. In addition, a higher fidelity estimation of the number of sensors needed in recursive applications is also presented. As a result, implementations of the multi-IMU fusion technique can be designed based on the design tools. These tools allow for engineers to evaluate the benefits of lower C-SWAP and the accuracy degeneration of the algorithm.

The multi-IMU approach is validated in simulations and further verified in instrumentation. The results from simulations of both interpolation techniques and the full multi-IMU techniques are detailed in this chapter. The simulations showed the proposed method of interpolation provides positional accuracy at the sampling frequency equal to the PRF of the SAR system. In addition, the interpolation method is validated through a flight test where the interpolation method provided adequate results at a higher frequency. Lastly, the result of the multi-IMU technique is also shown to provide better accuracy with lower C-SWAP components as compared to a high-grade, bulky INS system. With the results shown in this chapter, the interpolation technique paired with the multi-IMU fusion method is validated to successfully address the issues of providing accurate positional solutions at the rate equal to the PRF of SAR systems and the issues of minimizing C-SWAP without

compromising the accuracy of the positional solution. The techniques presented and validated in this chapter are the novel contribution of this dissertation. In the next chapter, the INS system utilizing the techniques explained in this dissertation are applied to a radar configured to capture data that can be processed to produce SAR images.

6 SAR Tests

In this chapter, methods are verified that the proposed algorithms may be used in a practical SAR imaging scenario. This is accomplished through a series of ground test performed using the NovAtel Span system in conjunction with a custom Ku-band pulse-Doppler radar system constructed at the University of Oklahoma. This ground test is performed by placing several targets within the main beam of the radar antennae and moving the radar on a cart perpendicular to the line-of-sight to the targets, generating a synthetic aperture. Measurements of the platform motion are taken by the NovAtel unit while the radar pulses, and the UPF and the interpolated Kalman filter are used to estimate the radar position at each pulse. By using the time interpolation inherent to each algorithm, the position can be estimated at a rate equivalent to the radar PRF of 3 kHz. The position estimates may then be fused with the range profiles produced by the radar using the backprojection algorithm to produce a 2-D image of the scene.

Additional to the interpolated methods, the system is also leveraged to compare the effects of the multi-IMU fusion technique and the traditional single IMU approach to SAR PNT. The utilization of multiple IMUs allow for a more accurate positional solution than what can be obtained with a single IMU. The fusion of 3 low-grade IMUs is directly compared to the position solution obtained by a single high-grade IMU. The effects of each PNT approach on the SAR images produced by the described SAR system is evaluated.

6.1 Radar Hardware

The radar system used in the test is a custom-built system designed by the University of Oklahoma [37]. Operating at a carrier frequency of 16.6 GHz, it is designed for use on a slow-moving aircraft and it pulses with a PRF of 3 kHz. The

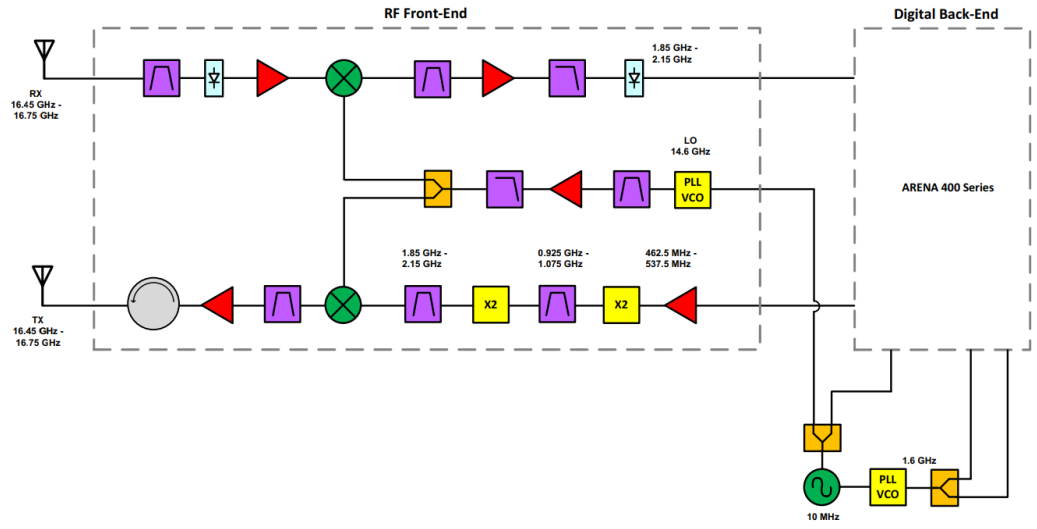

Figure 6.1: A block diagram of the radar system.

pulsed waveform is a linear frequency modulated (LFM) pulse with 300 MHz of bandwidth, giving a radial range resolution of 0.5 m after the pulse compression operation. To capture the radar data and provide pulse synchronization to the NovAtel unit, an ARENA413 software-defined radio (SDR) is used. A block diagram of the radar system is shown in Fig. 6.1.

6.2 Measurement Test Setup

In order to ensure an unambiguous imaging scene, three reflective metal targets were placed in a field 20 meters from the radar. A Google Earth view of this scene, including the radar location, is shown in Fig. 6.2. With the radar antennas pointed toward the targets, the radar and NovAtel were moved on a cart over a 10 m synthetic aperture and 10 s worth of data (30,000 pulses) was collected. After the data collection, the processed position data and the radar pulses are down-selected to 2000 pulses ($\sim$ 1 m aperture) to give azimuthal resolution on the same order as the range resolution. Images of the radar and the reflectors are shown in Fig. 6.2. The raw radar data was pulse compressed, and pulse-by-pulse radar position estimates

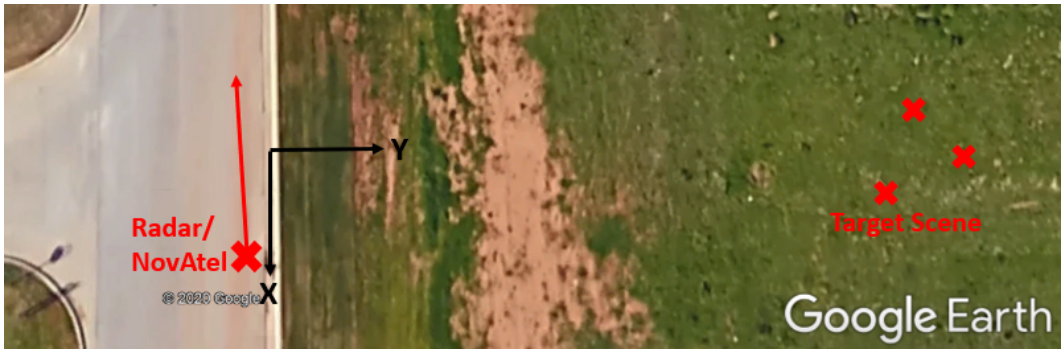

Figure 6.2: An image of the reflectors relative to the radar.This image was obtained using Google Earth.

were produced using the UPF and interpolated Kalman filter. The resulting range profiles were fused with the position estimates using the backprojection algorithm to form focused images of the scatterers in the scene.

6.3 Results

An image of the radar scene using the UPF is shown in Fig. 6.5. The three targets indicated in the scene in Fig. 6.2 are visible in this image and are in the correct relative locations. While typically a Hamming or Blackman window would be applied in range with the matched filter and azimuthally in the pulse dimension to suppress sidelobes, this was not done here since observation of the sidelobes is instructive on the quality of the image formed. Clearly, from Figure 6.5, it can be seen from the shape of the point targets and their sidelobes that the radar pulses combined with the position tracking provided by the UPF yield a near-ideal point spread response for each of the targets. Another image of the radar scene, formed using the interpolated Kalman filter, is shown in Fig. 6.6. While the targets are still easily visible in the same configuration as in Figs. 6.2 and 6.5, the targets are smeared compared to those in Fig. 6.5 and also undergo a translational shift, indicating the presence of large errors in the platform positioning. From these results,

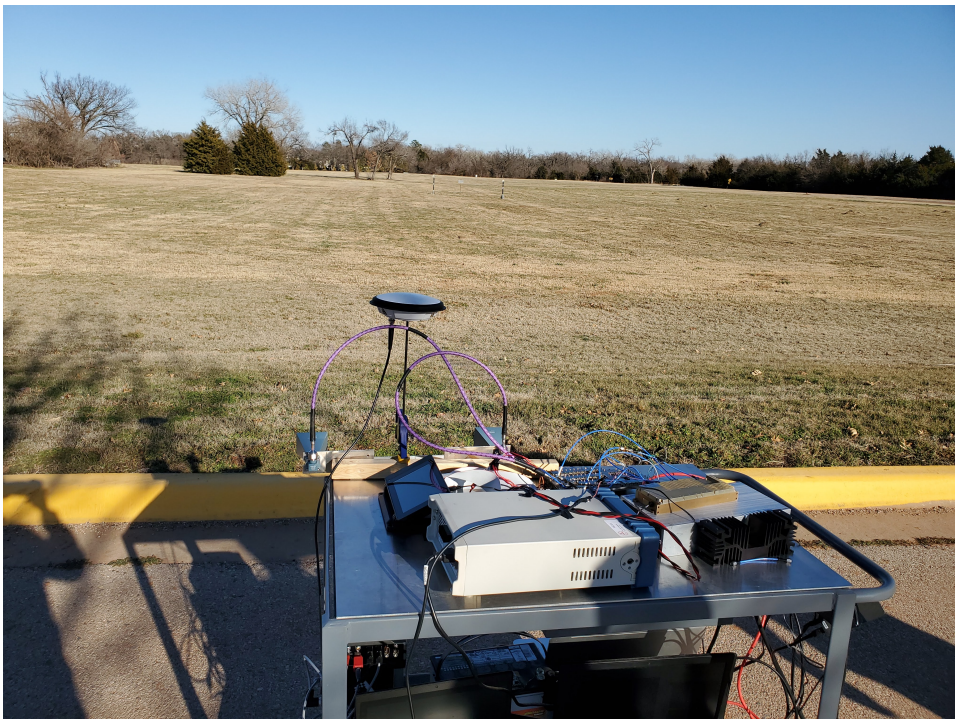

Figure 6.3: A image of the test setup utilized to capture the data.

Figure 6.4: The three targets placed in the target scene for the tests.

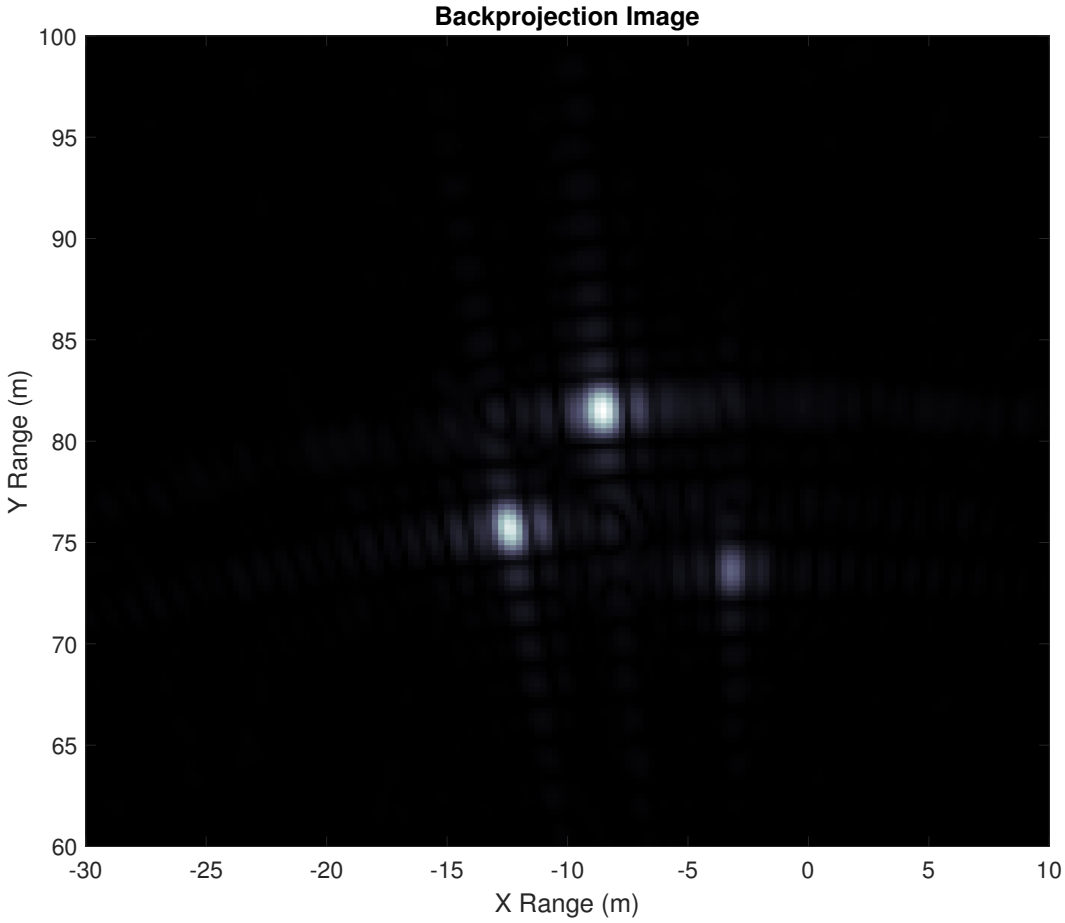

Figure 6.5: A SAR image of the target scene using the UPF to form the position estimates.

it is clear that while both algorithms may be used to produce quality SAR images, the UPF exhibits better performance. An image of the radar scene created using the UPF is shown in Fig. 6.5.

Comparing Figs. 6.5 and 6.6, it is apparent that the SAR image created using the proposed UPF is much more focused than the image created using the upsampled Kalman filter. This is unsurprising considering the results from Fig. 5.18, which clearly show that the UPF produces position estimates that are in general much more accurate than the upsampled Kalman filter. Therefore, it is expected that the phase alignment process, as part of the backprojection algorithm, will be more accurate

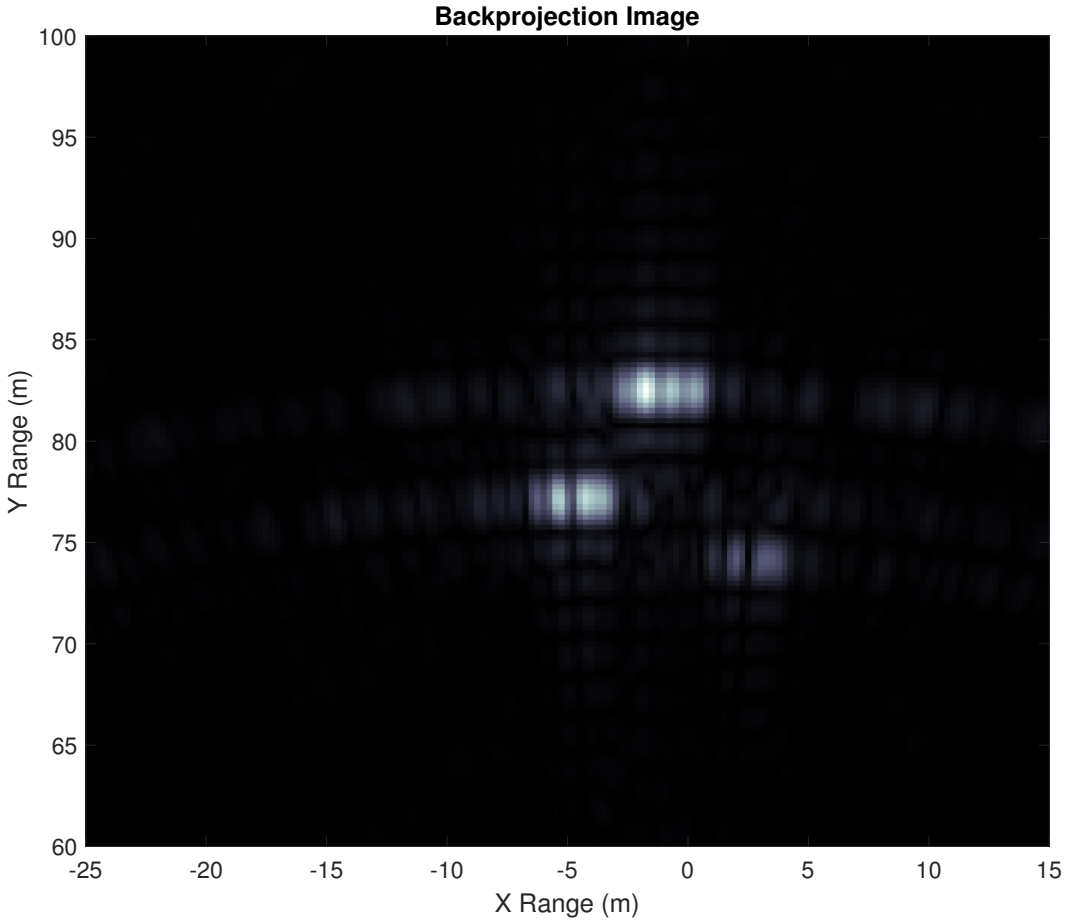

Figure 6.6: A SAR image of the target scene using the interpolated Kalman filter to form the position estimates.

and thus result in a more focused image.

To further illustrate the effectiveness of the proposed upsampled fusion algorithms, SAR images are also formed using the spline interpolation method to interpolate position estimates for each radar pulse using only GPS measurements (Fig. 6.7), GPS/IMU measurements fused with a Kalman filter (Fig. 6.8), and GPS/IMU measurements fused with a particle filter (Fig. 6.9). The spline method does not allow for an accurate enough position estimation in order to adequately compensate for phase during the backprojection algorithm. Because the phase is not adequately compensated for, the resulting backscatter images are unable to be focused. This

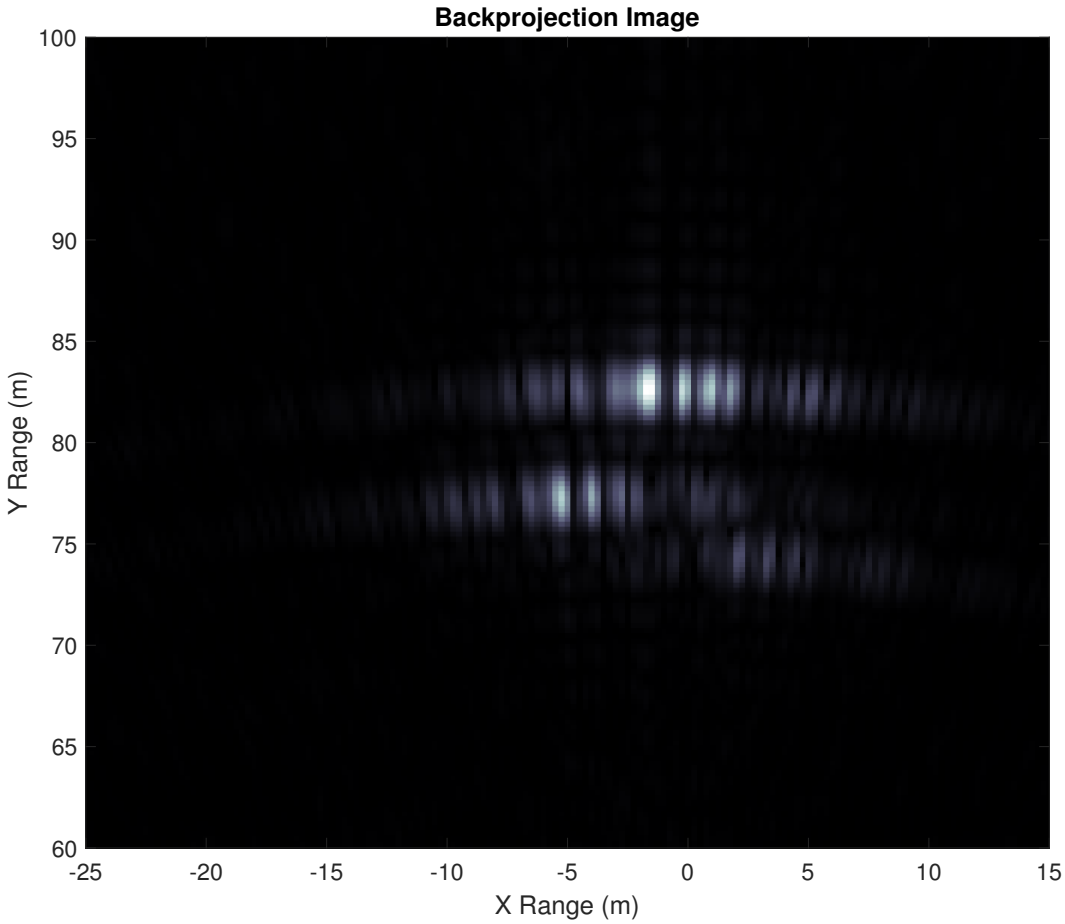

Figure 6.7: A SAR image of the target scene using the spline interpolation of GPS measurements to form the position estimates.

not only validates the need for accurate and sufficiently sampled INS data but also indicates that the proposed upsampled fusion algorithms are better suited for SAR imaging applications compared to traditional interpolation techniques.

To provide some more details, in Fig. 6.7, the raw measured GPS data are interpolated using the spline method. This interpolation method does not correct for the errors in the GPS position as the IMU measurements are not considered. As a result, polynomial interpolation is used on the GPS measurements to provide a position estimation for each pulse of the radar. While the position solution is provided for each pulse, the errors from this method prevent the formation of focused

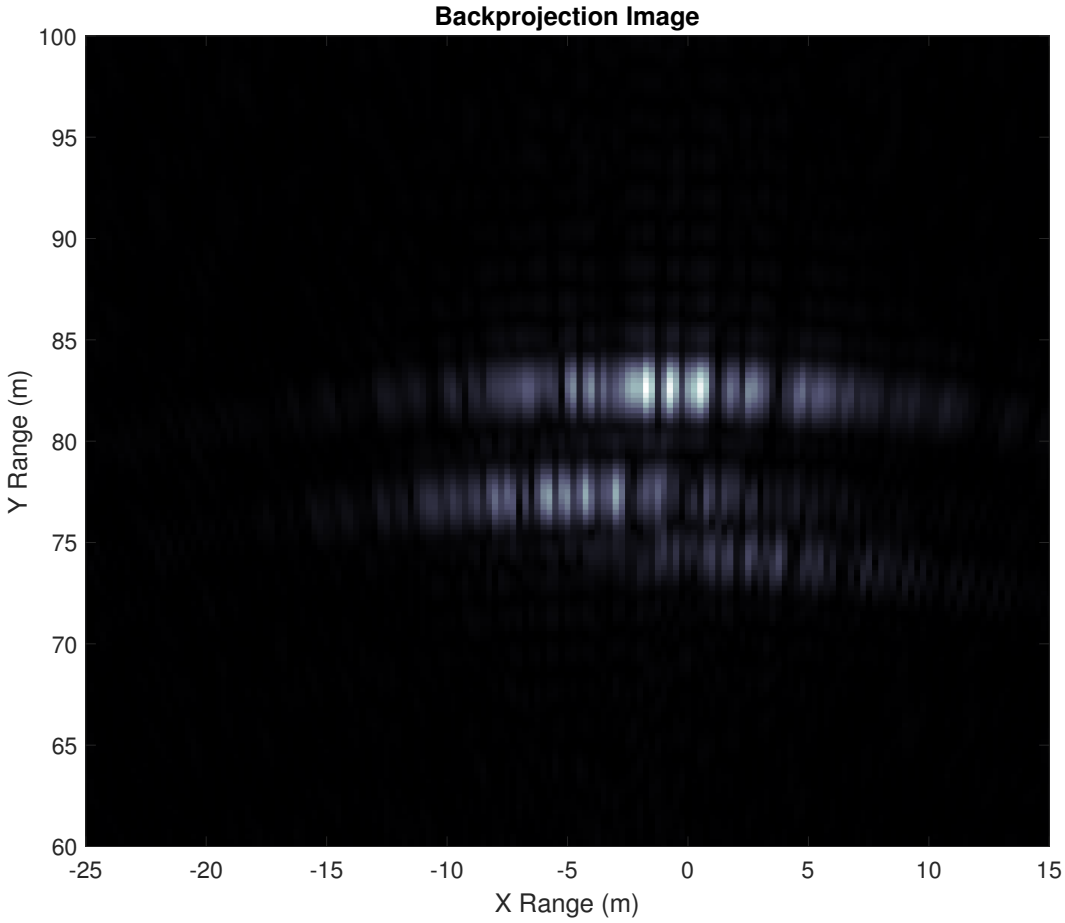

Figure 6.8: A SAR image of the target scene using the spline interpolation of GPS/IMU measurements fused using the Kalman filter to form the position estimates.

SAR images as the GPS errors, and the errors introduced by the spline interpolation, introduce large errors in the SAR signal phase. In Fig. 6.8 and Fig. 6.9, the spline interpolation technique interpolates between the position solutions provided by the IMU fused with the GPS using the Kalman and particle filter, respectively. In these results, the IMU measurements are incorporated and the position solution is provided on the IMU sampling rate. The result is a position solution with the GPS and IMU errors corrected by the fusion algorithms. The spline interpolation method is then used on the fused position solutions to provide radar positions for

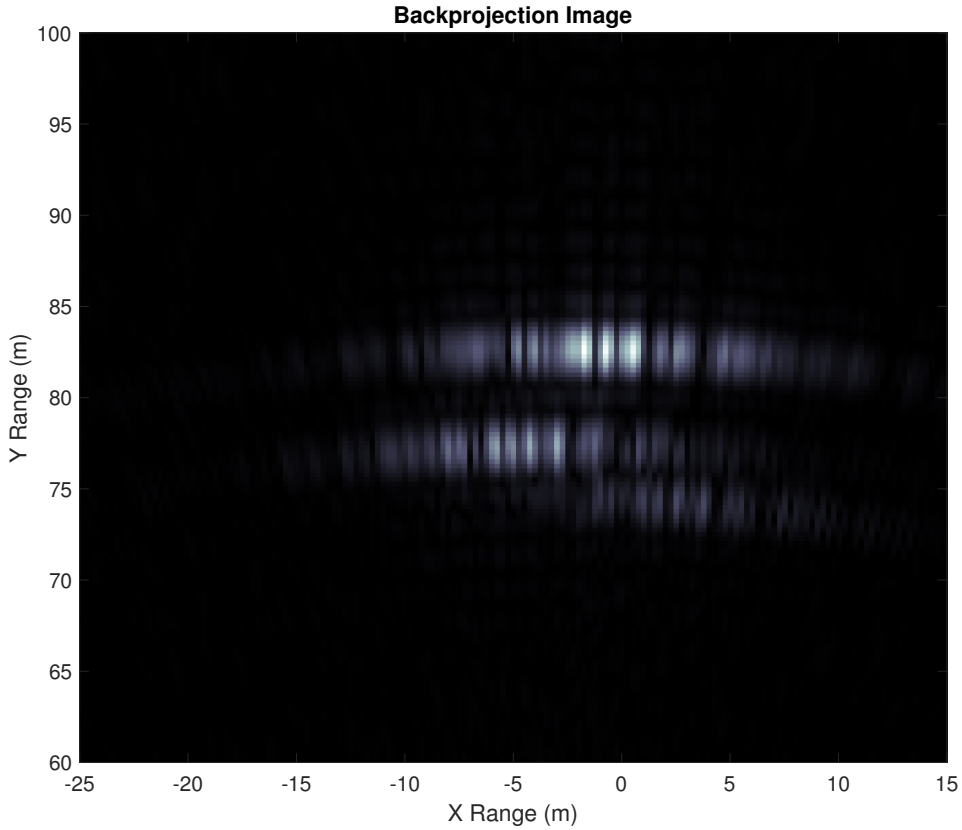

Figure 6.9: A SAR image of the target scene using the spline interpolation of GPS/IMU measurements fused using the particle filter to form the position estimates.

each pulse transmitted by the radar. Even though the position solutions provided at the IMU sampling rate incorporate the motion model and are corrected position estimates from the sensors, the spline interpolation ignores the motion model and external forces on the radar. Moreover, the IMU sampling rate of 200 Hz is still drastically lower than the 3 kHz PRF of the radar. As a result, the spline interpolation technique introduces additional phase errors. These errors are readily seen in the SAR image as smeared (defocused) targets.

From these results, it is clear that while both the proposed interpolated Kalman and UPF algorithms may be used to produce quality SAR images, the UPF exhibits better performance. While the targets are still easily visible in the same configura-

tion as in Figs. 6.2 and 6.5, the targets are defocused compared to those in Fig. 6.5 and also undergo a translational shift indicating the presence of large errors in the platform positioning. In summary, the results of the interpolation technique indicate that the use of lower sampling rate GPS/IMUs can be used with a high PRF SAR system and generate focused SAR images without the need for autofocus techniques and processing.

6.4 Airborne SAR

An airborne SAR test is used to further prove the interpolation algorithm's capabilities in producing position solution for each pulse of the radar with 3dimensional motion. In order to accomplish this, the SAR system was instrumented on a similar Piper Warrior to the one used during the flight test described in chapter 5.10. The horn antennas during this experiment are mounted externally to the aircraft. In addition, the SAR system is integrated into the same cargo bay as the NovAtel IMU system. The aircraft flew paths north to south while the radar illuminated the stadium and captured the echoes reflected from the stadium. An overlay of the focused SAR image on a google maps image of the target scene is shown in Fig. 6.4. Additionally, the focused SAR image with no transparency is shown in Fig. 6.11.

Figure 6.10: Airborne SAR image of University of Oklahoma stadium overlaid on Google Earth image.

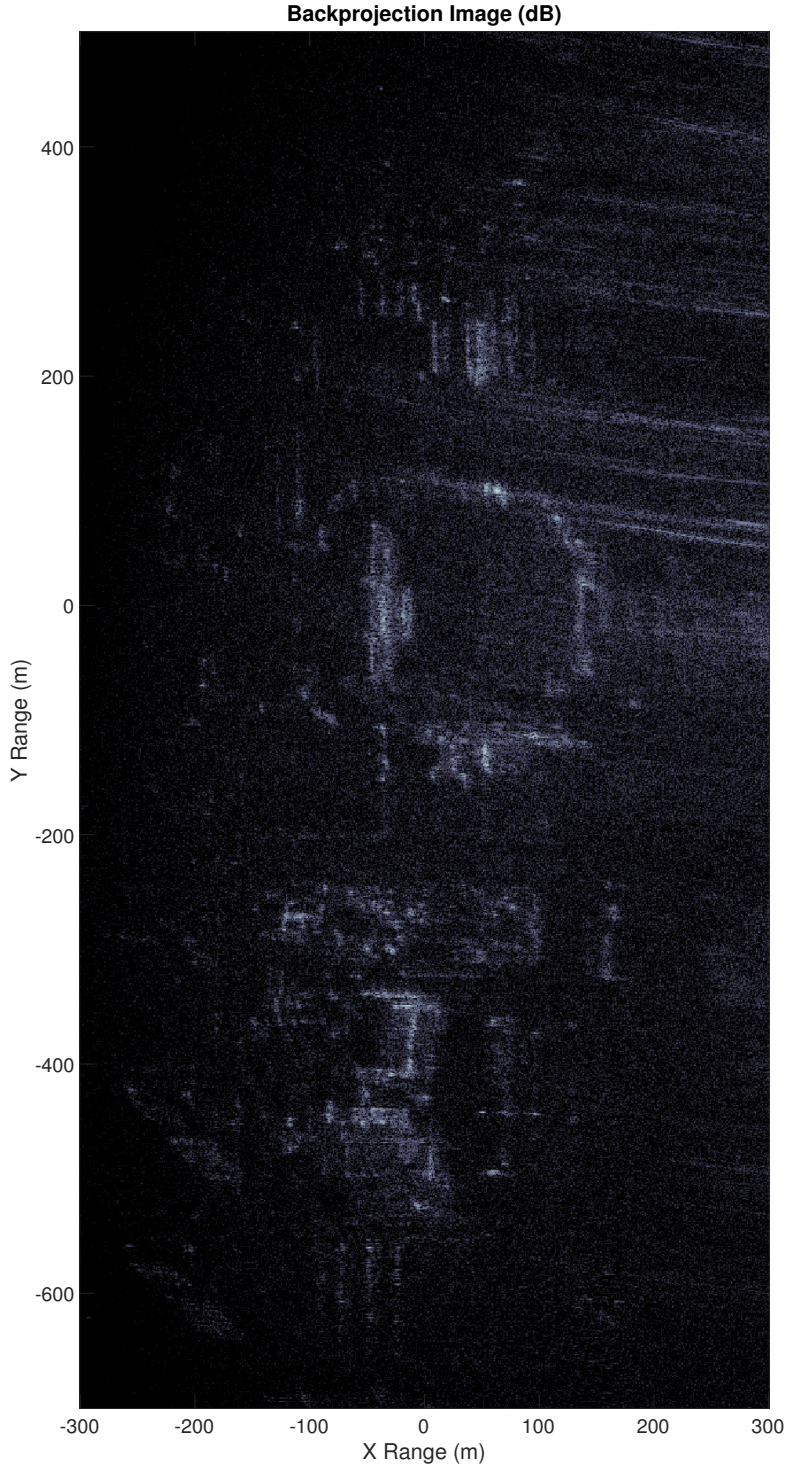

Figure 6.11: The focused SAR image of the University of Oklahoma stadium.

The focused image accurately represents the target scene and the general shape of the stadium can be resolved. It can also be observed in the focused image that the shapes and relative locations of the surrounding buildings can also be resolved using the NovAtel system with the upsampled particle filter technique. These results show confidence that the NovAtel system utilizing the UPF technique developed in this dissertation can produce an accurate enough PNT solution in 3-dimensional motion. In addition, the use of the interpolation algorithm paired with the NovAtel system to focus SAR images is shown to be a success. As a result, the technique is verified in simulation and instrumentation where a real target scene can be imaged utilizing the technologies presented in the previous chapters.

6.5 Multi-IMU

The multi-IMU is implemented on the same SAR system used for the interpolation tests. A similar target scene is also utilized however two trucks are used as targets and are arranged in the field as opposed to the previous scene with three corner reflectors as targets. The radar is instrumented on the cart with both the NovAtel and multi-imu navigation solutions utilizing the interpolation technique. The image from the NovAtel system is shown in Fig 6.12 and the two targets can be seen as well as the trees depicted in Fig6.4.

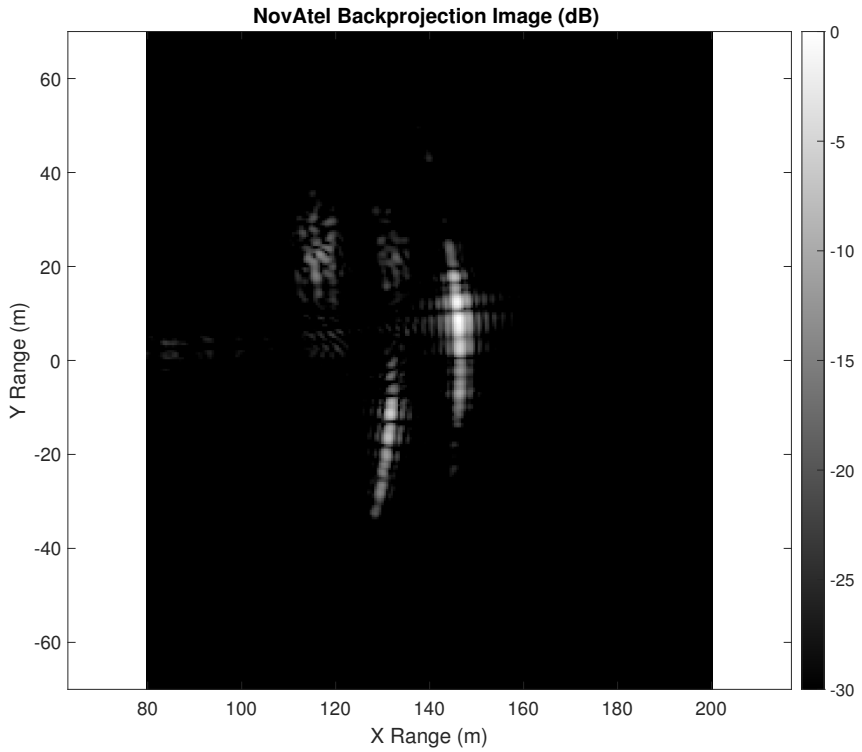

Figure 6.12: A SAR image of the target scene using the NovAtel IMU to form the position estimates.

The NovAtel system can focus the SAR image and produce 2 distinct targets. In addition, the system is also able to resolve the trees that were also in the scene. Similar to the ground tests done for the interpolation method, the NovAtel IMU produced images that is representative of the target scene. The multi-IMU solution for the same experiment is captured in addition to the NovAtel system and a SAR image is formed. The multi-IMU data used is the data collected in tandem with the NovAtel system. Furthermore, the SAR image from the multi-IMU navigational solution using the same radar pulses as the NovAtel system is shown in Fig. 6.13.

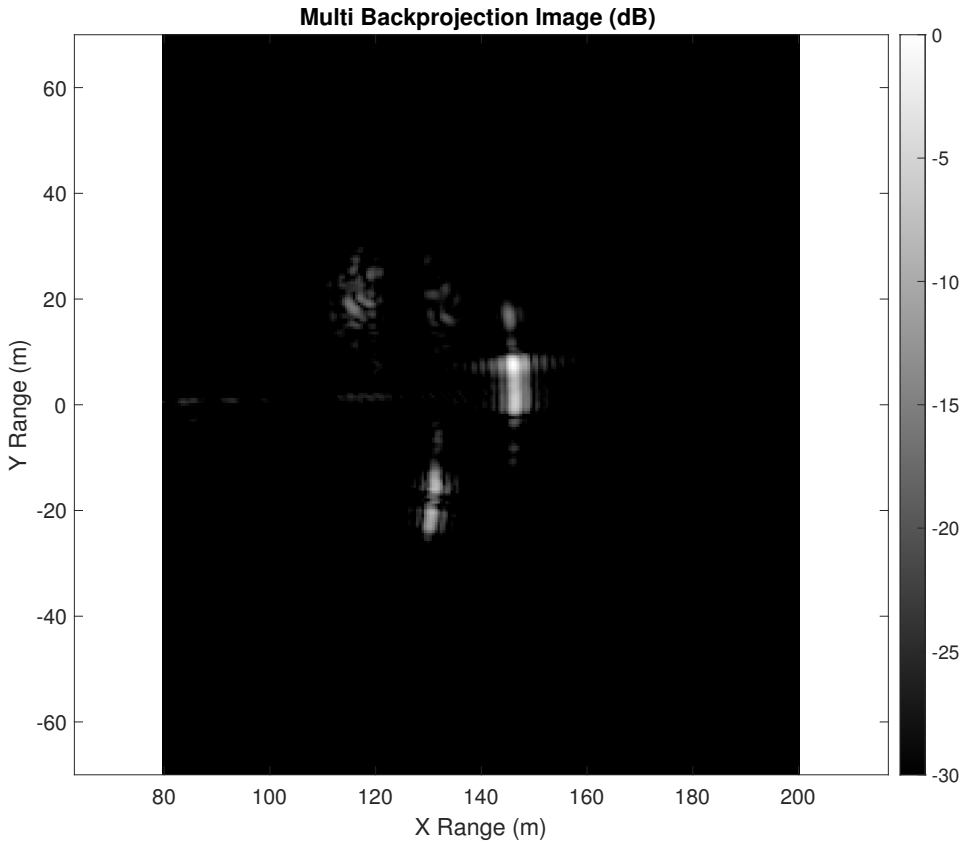

Figure 6.13: A SAR image of the target scene using the multi IMU to form the position estimates.

Visual inspection shows that the multi-IMU system can better focus the image as the targets are tighter and do not span as many pixels as the targets resolved using the NovAtel system. The results obtained by both systems show that the multi-IMU is capable of producing high accuracy position solutions on par with the high-end NovAtel IMU. In addition, the system is capable of producing PNT for SAR applications when paired with the interpolation method. The results show that the fusion of multiple lower grade IMUs can be used as a SAR PNT solution. Furthermore, the interpolation method allows for lower grade IMUs with sampling rates much lower than the SAR PRF can be used to produce synchronous PNT solutions for

each pulse of the SAR system. Now that the interpolation technology introduced in this dissertation has been proven to be functional, further improvements can be implemented to optimize the abilities of the method.

6.6 Summary

In this chapter, the SAR system utilized to validate the data fusion techniques is detailed. In general, the system is a miniaturized all commercial of the shelf system that operates at a 16.6 GHz. The results from various ground base experiments are presented with this system instrumented with the NovAtel INS and the multi-IMU INS to form SAR images. The SAR data showed the interpolation technique is able to produce positional accuracy high enough for the formation of SAR images. Furthermore, the interpolation technique presented outperformed the popular spline interpolation techniques when comparing the quality of the SAR images formed. The system is then tested in a flight tests to validate the interpolation performance on an airborne platform. Lastly, a comparison of the SAR images formed from the NovAtel system and the multi-IMU system using the same radar data is shown. As a result, the multi-IMU method showed capability in producing images that were more focused than the images formed using the NovAtel system. Validating that three lower-grade, lower C-SWAP sensors can be fused to provide a positional accuracy that is akin to the a higher-grade, higher C-SWAP sensor.

The results presented in this chapter successfully verify that the novel contributions of this dissertation successfully address the problems of INS systems providing positional solutions at the PRF of SAR and the multi-IMU technique to minimize C-SWAP without sacrificing accuracy. The focused SAR images from the ground test show that the multi-IMU method is capable of outperforming the high-grade NovAtel INS system in SAR applications. The contributions of this

work enables the miniaturization of SAR systems by allowing lower C-SWAP INS integration with miniature SAR systems.

7 Conclusions and Future Work

7.1 Summary

Current solutions to navigational problems provide challenges that are unique to the application of SAR. This is largely due to tight accuracy requirement leveraged by the signal processing techniques utilized to focus a SAR image. The challenge of obtaining accurate positional estimates of the SAR platform is an issue that is currently being solved by increasing the accuracy of a single IMU. In addition, modern pulse SAR systems require positional updates at much higher rates than what can be produced by the currents solutions. As a result, two navigational challenges arise when attempting to miniaturize SAR systems. The first challenge is producing highly accurate positional solutions at the update rate required. The second challenge is to reduce the C-SWAP of the navigational system without compromising the positional accuracy. These challenges are discussed in chapter 1.

The navigation of a moving platform first requires knowledge of the geolocation of the platform. Locations inherently are relative to a point of reference. These points of reference are often origins of a coordinate system used to describe the location. Furthermore, multiple coordinate systems exist and describe location given different reference points. In order to establish a location for the platform, sensors are used to observe the physical state of the platform. However, the sensors have inherent noise that negatively affects the accuracy of the platform's estimated location. In general, the sensors popularly used are GPS and IMUs and each has distinct limitations that contribute to the inaccuracies of the final position estimation. Additionally, the state observations made by the sensors are often expressed in a different coordinate system than the location of the platform. As a result, the transformation between these coordinate frames also contributes errors to the positional estima-

tion of the platform. The functionality of the sensors and the coordinate frames is presented in chapter 2.

Utilizing the information received by the sensors to produce a positional solution can be done in various ways. The most basic is to initialize the estimator with an initial position and the new positions are calculated using the IMU state measurements. Utilizing a motion model allows for the prediction of positional solutions based on the accelerations values measured by the IMUs. This method is known as *dead reckoning* and does not account for the errors in the IMU state measurements. As a result, the position solution compounds the errors from the IMUs and introduces an ever-increasing amount of error. In order to combat the compounding errors, the idea of *data fusion* allows for the predicted positional solution to be corrected based on additional measurements obtained about the platform state. These techniques and topics are described in section 2.2.5.

The Kalman filter is a popular and effective data fusion method that is utilized to estimate position solutions. The method utilizes statistical models of the errors within the system and calculates a weighted average between the prediction via a motion model and the observed position measurement. In addition, the Kalman filter also updates the statistical confidence of the predicted solution to be recursively used in the next time epoch. This method uses GPS measurements to correct the sensor drift caused by the IMUs. As a result, the positional accuracy of GPS or better can be obtained while producing positional solutions at the increased update rate IMU. The math and fusion process of the Kalman filter is detailed in section 3.1.

An alternative fusion technique is the particle filter which utilizes a sample representation of the posterior distribution to estimate the position of the platform. The sample representation utilizes the measurement of the state to re-sample the repre-

sentation of the posterior distribution. As a result, the distribution converges to the true distribution of the estimated state. The position of the platform is calculated by taking the expected value of the posterior distribution thus, the accuracy of the sample representation of the distribution is directly proportional to the accuracy of the final state estimation. These concepts are explored in section 3.2.

In order to have the navigational system produce positional solutions at the PRF of the SAR system, an interpolation method is required. The update rates of the navigation systems are often slower than the PRF of most modern radars. Traditional spline interpolations techniques are not sufficient for producing sharply focused SAR images. An interpolation technique that utilizes the motion model and the IMU measurements to predict the platform location more often. The interpolation technique implementation for both the Kalman filter and the particle filter is detailed in section 3.3.

The SAR technique utilizes a moving radar to synthetically create a larger aperture to increase the amount of energy that is transmitted to ”illuminate” the target scene. The energy is reflected from the targets of the illuminated scene and can be used to form an image of the target scene. In order to create a sharp and focused image, the position of the radar at each pulse is required to coherently combine the energy reflected from each scatterer and align the phases of the waveform. As a result, the SAR application requires the navigation system to produce solutions for each pulse of the radar with high positional accuracy. The applications space of navigation solutions in the SAR application is explained in chapter 4.

An attempt to minimize the C-SWAP of the navigational system, the concept of data fusion is leveraged where the collection of multiple measurements is combined to obtain a more accurate solution. In this way, the concept can be extended to an instrumented approach where additional sensors are added to the system to ob-

tain a more accurate solution. This concept as it pertains to decreasing C-SWAP is counter-intuitive, however, the C-SWAP is decreased if the additional sensors used have a combined lower c-SWAP compared to the single sensor approach. Additionally, the accuracy benefits obtained by the fusion technique allow for lower-grade sensors to be utilized to achieve similar results to the brute force approach of using a single high-grade sensor. The fusion method utilized to achieve these concepts is augmenting the navigation fusion with an additional SIR step. In doing so, the posterior distribution is estimated utilizing multiple sensors observing the physical state of the platform. The result is a posterior distribution that is more accurate as it is based on more measurements. The process and augmentation SIR step is discussed in chapter 5.

The augmentation of the SIR method performs well for the multi-IMU measurement and does produce higher accuracy in the positional solutions than a single IMU of the same quality. The method does have limitations that pertain to scaling the method for a large number of sensors whereby the increase in positional accuracy does not linearly increase with each additional sensor. As a result, there is a point where the addition of another sensor does not provide enough benefit to outweigh the computational requirements required of the additional sensor. In addition, the weights of the sensors used for SIR are currently calculated based on GPS measurements. This causes the accuracy of the GPS measurement to heavily impact the accuracy of the positional solution. These limitations are discussed in section 5.2.

The SIR method for multi-IMU fusion is verified first in simulations where flight paths and sensor measurements are simulated and fused using the multi-IMU method. The simulations include a simple flight path generated in MATLAB and different sensor variances are simulated. The second simulation utilized a 3rd party

python library to produce the flight paths and sensor measurements. The fused results indicated the solution is capable of both producing higher quality position solutions than a single IMU of the same grade and producing position solutions for every pulse of the SAR system. Details of these simulations and results are presented in section 5.3.

With the confidence the method is feasible as proven in simulations, an instrumented system is then used to verify the algorithm on data collected on a moving platform. The instrumentation first tested the interpolation techniques to verify the interpolation techniques did not introduce additional errors when producing position solutions at a finer update rate. Once the interpolations were verified, the interpolation technique is paired with the multi-IMU fusion technique and the results were compared to a highly accurate IMU. The results showed that the fusion of 3 lower-grade IMUs are capable of producing solutions that were as accurate or more accurate than the high-grade IMU. These results are explained in section 5.6.

Finally, the interpolation techniques are implemented on a SAR system and the performance of the navigation solution is tested. The target application for the algorithms is to address the issues of decreasing C-SWAP in a SAR system and to produce positional solutions on a finer update rate. As a result, the SAR system implemented is used to verify the designed algorithms are sufficiently solving the issues within the target application. SAR images are focused on point targets on ground-based tests to verify the images can be focused using the interpolation technique. The multi-IMU method is then deployed on the SAR system and the focused images were compared to images focused using the higher grade IMU. These tests and results are presented in chapter 6.

7.2 Conclusion

The location of a navigational platform is not an easy solution to obtain accurately. The current and most popular approach utilizes GPS signals to approximate the location of the platform. The challenge with utilizing GPS signals is caused by inaccuracies in the location approximation. These inaccuracies are caused by erroneous signal reflections and are reliant the on line of sight between the receiver and the satellite. Additionally, the transmission range of GPS signals is significantly large and limits the update rate of the position solutions. This is a major limitation for SAR applications where position solutions for every pulse need to be extremely accurate and on a fast time scale compared to the update rate of GPS. The introduction of IMUs allows for an increase in update rates because positional estimates can be made without relying on the long transmission times of GPS. However, the IMUs have inherent errors that are compounded over time as the position estimation is a recursive process. The compounding errors cause the position estimation to drift or ”walk” over time. In order to remedy this, the concept of data fusion is used to combine or ”fuse” the information from both sensors to provide more accurate position solutions at a faster update rate. The addition of an IMU and data fusion is still unable to produce position solutions fast enough for SAR application. An interpolation method was designed and implemented to specifically provide position solutions that are synchronous with the PRF of the SAR system. The interpolation method allowed for accurate position solutions capable of producing more focused SAR images than the traditional spline interpolation method.

The interpolation method provides a good solution to increasing the update rate of positions that are synchronous with the SAR system. However, the limitation of obtaining highly accurate position solutions still requires a highly accurate IMU. Highly accurate IMUs are often bulky and heavy which increases the C-SWAP re-

quirements for a SAR platform. While often SAR platforms are capable of supporting the larger C-SWAP requirements, the reduction of C-SWAP is required miniaturizing SAR platforms. The challenge here is to reduce C-SWAP while maintaining the accuracy of the positional estimates. Utilizing the strength of data fusion, a method of fusing multiple lower-grade sensors using the sequential importance resampling to obtain a position solution with equivalent accuracy as a single high-grade sensor was developed.

The fusion of the multiple smaller, lower-grade sensors paired with the interpolation techniques to synchronize the position updates with the PRF of the SAR system allows for a reduction in C-SWAP without trading image quality. The method presented in this dissertation opens the door for small form factor SAR systems that can be deployed on smaller unmanned drones. In addition, the fusion of multiple low-grade IMUs allows for an increase in positional accuracy without having to replace the navigation system completely. Furthermore, the additional sensors help minimize the drift in the positional accuracy and can increase the duration a navigational platform can navigate without a GPS update.

The contributions of this dissertation allow for the reduction of C-SWAP of PNT systems without sacrificing accuracy. In addition, the traditional trade-off of increasing positional accuracy results in a proportional increase in C-SWAP is no longer a limitation in the design of PNT solutions. As a result, PNT solutions can now be developed to achieve an increase in accuracy by adding additional IMUs. This allows for engineers to leverage lower C-SWAP IMUs and maintain the positional quality of the solution provided.

In conclusion, the interpolation method presented in this dissertation allows for any IMU update rate to be synchronized with the PRF of a SAR system. As a result, the design constraint of utilizing IMUs with comparable update rates to the

SAR PRF is removed. In addition, the interpolation method provides the fundamental synchronization technique required for the multiple sensor fusion technique presented. The multi-IMU technique developed removes the design constraint of trading positional accuracy for C-SWAP. Maintaining positional accuracy without having to increase C-SWAP allows for the miniaturization of SAR systems to be more easily achieved. Lastly, these methods have been instrumented and verified in ground and airborne platforms. The results of the instrumented methods show that it is possible to synchronize and fuse multiple sensors to achieve a more accurate position estimate than a single sensor and the method can be used to reduce the C-SWAP of at SAR PNT solution. The reduction in C-SWAP is also beneficial applications beyond SAR. Any application that requires a PNT solution can leverage the contributions in this dissertation to miniaturize the PNT solution. Conversely, PNT solutions can now achieve an increased positional accuracy than any single IMU can provide. As a result, the contributions in this dissertation removes the trade-off between C-SWAP and positional accuracy.

7.3 Future Work

As the multi-IMU algorithm has been proven to be successful in producing positional accuracy that is greater than a single IMU of the same kind, the next step is to prove the theory out for IMUs with different characteristics. In this way, the effects of different quality IMUs can be explored and their effects on accuracy can be characterized. In addition, the permutations of different quality IMUs can potentially allow for additional advantages in both accuracy and C-SWAP. An example hypothesis is an addition of a slightly more accurate IMU with a minor increase to C-SWAP relative to the other IMUs provides a significant boost in positional accuracy that outweighs the increase in C-SWAP. Given the hypothesis holds true,

system engineers will have an increased flexibility where the impacts to C-SWAP can still be maintained while potentially increasing positional accuracy.

Another area of expansion is utilizing *spatio-temporal dithering* concept where a small amount of perturbation is intentionally added into the system to increase sample independence. In this application, one technique that can be utilized is to instrument the system by perturbing the locations of the sensors spatially. The spatial dithering can lead to each sensor to measure slightly different characteristics in the system state which increases sample independence. For example, a 3 IMU system can be instrumented with an IMU located on the center of gravity of the platform with the other two on either side of the axis of travel. The configuration allows for the rotation to be measured from different points on the platform where the 2 IMUs of center from the center of gravity will experience opposing forces in rotation. Furthermore, the configuration can also be changed by differing the orientations of the IMUs to potentially addressing sensor biases in specific axis. The idea is to orient the sensors in a way that the effects of sensor bias in each axis are opposed so that the overall effects of sensor bias is minimized when processed. Lastly, the sensor measurements can be dithered temporally where the sensors are forced to be a synchronous to each other in hopes of producing more independent samples that increase the positional accuracy of the system. The interpolation techniques presented allows for different sampling speeds of the sensors to be utilized. As a result, the advantages of utilizing different sampling rate IMUs to produce measurements for the platform can provide another area of flexibility where a high-grade, slow sampling IMU can be coupled with low-grade fast sampling IMUs to maintain the level of accuracy desired.

Another area to expand this work into is in the area of distributed PNT where the location of a platform can be determined with measurements from disparate

sources. This area becomes extremely relevant with the developments in drone technology that allow for the utilization of swarms in remote sensing. In addition, the lower C-SWAP while maintaining PNT accuracy is a key enabler in realizing the use of drones for remote sensing. In SAR applications, the requirement of PNT data relative to each of the members in the swarm is needed to coherently process the information collected. In the case of the swarm creating a larger aperture, the phase center of the larger aperture needs to be accurately measured. As a result, the phase center will have to be estimated using INS systems distributed across the swarm.

The distribution drives changes to the fusion technique to account for the changes to the phase center contributed by each member of the swarm. Distributed fusion provides a unique challenges where the true location of each element relative to the other elements needs to be estimated. Additionally, the distribution of the sensors causes the probability distribution of the sensors to drastically change where now the sensors measurements may not be independent, identically, distributed. One area of benefit in the distributed fusion application is the possibility of the position estimation across multiple elements to be independently computed. The benefits could pave the way for reconfigurable apertures when utilizing a drone swarm to create an aperture. In addition, the individualized position solutions allow for graceful degradation or self healing apertures.

References

[1] Aceinna. *gps_ins_sim, Open-Source, Python-based GNSS-INS Simulation*. https://github.com/Aceinna/gnss-ins-sim. Version v2.1. 2018.

[2] Marcelo Albuquerque, Pau Prats, and Rolf Scheiber. "Applications of Time-Domain Back-Projection SAR Processing in the Airborne Case". In: *7th European Conference on Synthetic Aperture Radar*. 2008, pp. 1–4.

[3] M. Arulampalam et al. "A Tutorial on Particle Filters for Online Nonlinear/non-Gaussian Bayesian Tracking". In: *IEEE Transactions on Signal Processing* 50.2 (2002), pp. 174–188.

[4] O. Aydogmus and M.F. Talu. "Comparison of Extended-Kalman and Particle-Filter-Based Sensorless Speed Control". In: *IEEE Transactions on Instrumentation and Measurement* 61.2 (2011), pp. 402–410.

[5] C. Baker et al. "IEEE Std. 521-2019 - IEEE Standard Letter Designations for Radar-Frequency Bands". In: *IEEE Standards* (2020).

[6] Yaakov Bar-Shalom and Xiao-Rong Li. *Multitarget-multisensor tracking: principles and techniques*. Vol. 19. YBs Storrs, CT, 1995.

[7] C. Boucher and J. Noyer. "A Hybrid Particle Approach for GNSS Applications with Partial GPS Outages". In: *IEEE Transactions on Instrumentation and Measurement* 59.3 (2009), pp. 498–505.

[8] W.C. Carrara et al. *Spotlight Synthetic Aperture Radar: Signal Processing Algorithms*. Artech House remote sensing library. Artech House, 1995. ISBN: 9780890067284. URL: https://books.google.com/books?id=uztiQgAACAAJ.

[9] H. Carvalho et al. “Optimal nonlinear filtering in GPS/INS integration”. In: *IEEE Transactions on Aerospace and Electronic Systems* 33.3 (1997), pp. 835–850. DOI: 10.1109/7.599254.

[10] Shao-Hung Chan, Ping-Tsang Wu, and Li-Chen Fu. “Robust 2D indoor localization through laser SLAM and visual SLAM fusion”. In: *2018 IEEE International Conference on Systems, Man, and Cybernetics (SMC)*. IEEE. 2018, pp. 1263–1268.

[11] Yee Kit Chan and Voon Koo. “An introduction to synthetic aperture radar (SAR)”. In: *Progress In Electromagnetics Research B* 2 (2008), pp. 27–60.

[12] M. D’Arco et al. “An Online Quality Control System for GPS Stations used for Geodetic Surveillance”. In: *2012 IEEE International Instrumentation and Measurement Technology Conference Proceedings*. IEEE. 2012, pp. 507–511.

[13] P. Daponte et al. “A Method for Real-time Compensation of Magnetometers Embedded on Smartphones”. In: *2016 IEEE International Instrumentation and Measurement Technology Conference Proceedings*. IEEE. 2016, pp. 1–6.

[14] P. Del Moral, A. Doucet, and A. Jasra. “Sequential Monte Carlo Samplers”. In: *Journal of the Royal Statistical Society: Series B (Statistical Methodology)* 68.3 (2006), pp. 411–436.

[15] M.D. Desai and W.K. Jenkins. “Convolution backprojection image reconstruction for spotlight mode synthetic aperture radar”. In: *IEEE Transactions on Image Processing* 1.4 (1992), pp. 505–517. DOI: 10.1109/83.199920.

[16] Manlai Ding et al. “W Band Mini-SAR on Multi Rotor UAV Platform”. In: *2019 IEEE 2nd International Conference on Electronic Information and Communication Technology (ICEICT)*. 2019, pp. 416–418. DOI: 10.1109/ICEICT.2019.8846356.

[17] P. M. Djuric et al. “Particle Filtering”. In: *IEEE signal processing magazine* 20.5 (2003), pp. 19–38.

[18] A. Doerry, E. Bishop, and J. Miller. “Basics of backprojection algorithm for processing synthetic aperture radar images”. In: *Sandia National Laboratories Report, No. SAND2016–1682* (2016).

[19] Armin W Doerry. “Motion measurement for synthetic aperture radar”. In: *Sandia National Laboratories Report SAND2015-20818, Unlimited Release* (2015).

[20] A. Doucet, N. De Freitas, and N. Gordon. “An Introduction to Sequential Monte Carlo Methods”. In: *Sequential Monte Carlo Methods in Practice*. Springer, 2001, pp. 3–14.

[21] A. Doucet, N. deFreitas, and N. Gordon. *Sequential Monte Carlo Methods in Practice*. Springer Science & Business Media, 2001.

[22] A. Doucet, S. Godsill, and C. Andrieu. “On Sequential Monte Carlo Sampling Methods for Bayesian Filtering”. In: *Statistics and Computing* 10.3 (2000), pp. 197–208.

[23] Arnaud Doucet, Neil J Gordon, and Vikram Krishnamurthy. “Particle filters for state estimation of jump Markov linear systems”. In: *IEEE Transactions on signal processing* 49.3 (2001), pp. 613–624.

[24] Arnaud Doucet, Adam M Johansen, et al. “A tutorial on particle filtering and smoothing: Fifteen years later”. In: *Handbook of nonlinear filtering* 12.656-704 (2009), p. 3.

[25] Michael Israel Duersch. *Backprojection for synthetic aperture radar*. Brigham Young University, 2013.

[26] P. H. Eichel, D. C. Ghiglia, and C. V. Jakowatz. “Speckle processing method for synthetic-aperture-radar phase correction”. In: *Opt. Lett.* 14.1 (Jan. 1989), pp. 1–3. DOI: 10.1364/OL.14.000001. URL: http://www.osapublishing.org/ol/abstract.cfm?URI=ol-14-1-1.

[27] I. Engedy and G. Horváth. “Path Reconstruction Based on Gyroscope Bias Estimation using GPS”. In: *2015 IEEE International Instrumentation and Measurement Technology Conference (I2MTC) Proceedings*. IEEE. 2015, pp. 1465–1470.

[28] J. Fang and X. Gong. “Predictive Iterated Kalman Filter for INS/GPS Integration and its Application to SAR Motion Compensation”. In: *IEEE Transactions on Instrumentation and Measurement* 59.4 (2009), pp. 909–915.

[29] James Fienup. “Phase Error Correction by Shear Averaging”. In: *Tech. Dig. Series; Signal Recovery and Synthesis* 15 (Jan. 1989).

[30] H. Fourati. “Heterogeneous Data Fusion Algorithm for Pedestrian Navigation via Foot-mounted Inertial Measurement Unit and Complementary Filter”. In: *IEEE Transactions on Instrumentation and Measurement* 64.1 (2014), pp. 221–229.

[31] “GPS-AIDED INERTIAL NAVIGATION METHOD AND SYSTEM”. WO2016042545A1. shmuel Boyarski. Mar. 24, 2016.

[32] P.D. Groves. *Principles of GNSS, Inertial, and Multisensor Integrated Navigation Systems*. GNSS technology and applications series. Artech House, 2008. ISBN: 9781580532556.

[33] M. Jew, A. El-Osery, and S. Bruder. "Implementation of an FPGA-based aided IMU on a low-cost autonomous outdoor robot". In: *IEEE/ION Position, Location and Navigation Symposium*. 2010, pp. 1043–1051.

[34] Simon J Julier, Jeffrey K Uhlmann, and Hugh F Durrant-Whyte. "A new approach for filtering nonlinear systems". In: *Proceedings of 1995 American Control Conference-ACC'95*. Vol. 3. IEEE. 1995, pp. 1628–1632.

[35] Steven M Kay. *Fundamentals of statistical signal processing: estimation theory*. Prentice-Hall, Inc., 1993.

[36] T.A. Kennedy. "Strapdown inertial measurement units for motion compensation for synthetic aperture radars". In: *IEEE Aerospace and Electronic Systems Magazine* 3.10 (1988), pp. 32–35. DOI: 10.1109/62.9371.

[37] R. H. Kenney et al. "An All-COTS High Sampling Frequency Pulse-Doppler Imaging Radar". In: *2020 IEEE Radar Conference (RadarConf20)*. 2020, pp. 1–6. DOI: 10.1109/RadarConf2043947.2020.9266708.

[38] "LANE-LEVEL NAVIGATION SYSTEMS FOR GROUND VEHICLES WITH LIDAR AND CELLULAR SIGNALS". US20210278548A1. Zak M Kassas, Mahdi Maareef, and Joe Khalife. Sept. 9, 2021.

[39] Xin-yi Liu, Gan-lin Shan, and Jing-jing Shi. "Multi-sensor allocation based on Cramér-Rao Low Bound". In: *2014 IEEE Workshop on Electronics, Computer and Applications*. 2014, pp. 467–470. DOI: 10.1109/IWECA.2014.6845658.

[40] D Llaveria, A Camps, and H Park. “Correcting the ADCS Jitter Induced Blurring in Small Satellite Imagery”. In: *IEEE Journal on Miniaturization for Air and Space Systems* (2020).

[41] P. S. Madhukar and L. B. Prasad. “State Estimation using Extended Kalman Filter and Unscented Kalman Filter”. In: *2020 International Conference on Emerging Trends in Communication, Control and Computing (ICONC3)*. 2020, pp. 1–4. DOI: 10.1109/ICONC345789.2020.9117536.

[42] P. S. Madhukar and L. B. Prasad. “State Estimation using Extended Kalman Filter and Unscented Kalman Filter”. In: *2020 International Conference on Emerging Trends in Communication, Control and Computing (ICONC3)*. 2020, pp. 1–4. DOI: 10.1109/ICONC345789.2020.9117536.

[43] M. Mallick, T. Kirubarajan, and S. Arulampalam. “Out-of-sequence measurement processing for tracking ground target using particle filters”. In: *Proceedings, IEEE Aerospace Conference*. Vol. 4. 2002, pp. 4–4. DOI: 10.1109/AERO.2002.1036893.

[44] “METHOD AND DEVICE FOR LOCATING A VEHICLE”. US20210318779A1. Benjamin Rollet. Oct. 14, 2021.

[45] R. T. Nallapu et al. “Robust Spin Control Design for the AOSAT+ Mission Concept”. In: *IEEE Journal on Miniaturization for Air and Space Systems* 1.1 (2020), pp. 10–31.

[46] A. El-Osery, S. Bruder, and D. Laughlin. “High-accuracy heading determination”. In: *2013 8th International Conference on System of Systems Engineering*. 2013, pp. 308–313.

[47] O. Payne and A. Marrs. “An unscented particle filter for GMTI tracking”. In: *2004 IEEE Aerospace Conference Proceedings (IEEE Cat. No.04TH8720)*. Vol. 3. 2004, 1869–1875 Vol.3. DOI: 10.1109/AERO.2004.1367969.

[48] O. Payne and A. Marrs. “An unscented particle filter for GMTI tracking”. In: *2004 IEEE Aerospace Conference Proceedings (IEEE Cat. No.04TH8720)*. Vol. 3. 2004, 1869–1875 Vol.3. DOI: 10.1109/AERO.2004.1367969.

[49] Mark A Richards. *Fundamentals of radar signal processing*. Tata McGraw-Hill Education, 2005.

[50] G.G. Rigatos. “Particle Filtering for State Estimation in Nonlinear Industrial Systems”. In: *IEEE Transactions on Instrumentation and Measurement* 58.11 (2009), pp. 3885–3900.

[51] B. Ristic, S. Arulampalam, and N. Gordon. *Beyond the Kalman Filter: Particle Filters for Tracking Applications*. Artech house, 2003.

[52] Dennis Roddy. *Satellite communications*. Vol. 11. McGraw-hill New York, 2006.

[53] S. Sabatelli et al. “A Double-stage Kalman Filter for Orientation Tracking with an Integrated Processor in 9-D IMU”. In: *IEEE Transactions on Instrumentation and Measurement* 62.3 (2012), pp. 590–598.

[54] P. Samczynski et al. “Effective SAR image creation using low cost INS/GPS”. In: *2014 15th International Radar Symposium (IRS)*. 2014, pp. 1–4. DOI: 10.1109/IRS.2014.6869243.

[55] Piotr Samczyński. “Applications of a Modern micro-SAR System for Small UAV Operations (From Active to Passive SAR Technology)”. In: *2018 19th International Radar Symposium (IRS)*. 2018, pp. 1–8. DOI: 10.23919/IRS.2018.8448020.

[56] Simo Sarkka. “On unscented Kalman filtering for state estimation of continuous-time nonlinear systems”. In: *IEEE Transactions on automatic control* 52.9 (2007), pp. 1631–1641.

[57] J. Shen et al. “Evaluation of Unscented Kalman Filter and Extended Kalman Filter for Radar Tracking Data Filtering”. In: *2014 European Modeling Symposium*. IEEE. 2014, pp. 190–194.

[58] Miroslav Simandl, Jakub Královec, and T Soderstrom. “Anticipative grid design in point-mass approach to nonlinear state estimation”. In: *IEEE Transactions on Automatic Control* 47.4 (2002), pp. 699–702.

[59] Miroslav Šimandl and Ondřej Straka. “Nonlinear estimation by particle filters and Cramér-Rao bound”. In: *IFAC Proceedings Volumes* 35.1 (2002), pp. 79–84.

[60] I. Skog and P. Händel. “A Low-cost GPS Aided Inertial Navigation System for Vehicle Applications”. In: *2005 13th European Signal Processing Conference*. IEEE. 2005, pp. 1–4.

[61] Merrill Ivan Skolnik. “Radar handbook”. In: (1970).

[62] S. Sukkarieh, E.M. Nebot, and H.F. Durrant-Whyte. “A High Integrity IMU/GPS Navigation Loop for Autonomous Land Vehicle Applications”. In: *IEEE Transactions on Robotics and Automation* 15.3 (1999), pp. 572–578.

[63] B. Sun et al. “Fine Resolution Position Estimation Using Kalman Filtering”. In: *2019 IEEE International Instrumentation and Measurement Technology Conference (I2MTC) (I2MTC 2019)*. Auckland, New Zealand, May 2019.

[64] W. Sun and F. Sun. “Novel approach to GPS/SINS integration for IMU alignment”. In: *Journal of Systems Engineering and Electronics* 22.3 (2011), pp. 513–518.

[65] Y. Tao and H. Hu. “A Novel Sensing and Data Fusion System for 3-D Arm Motion Tracking in Telerehabilitation”. In: *IEEE Transactions on Instrumentation and Measurement* 57.5 (2008), pp. 1029–1040.

[66] “ULTRA-TIGHT COUPLED GPS AND INERTIAL NAVIGATION SYSTEM FOR AGILE PLATFORMS”. US200701018286A1. H. Wang. May 24, 2007.

[67] D.E. Wahl et al. “Phase gradient autofocus-a robust tool for high resolution SAR phase correction”. In: *IEEE Transactions on Aerospace and Electronic Systems* 30.3 (1994), pp. 827–835. DOI: 10.1109/7.303752.

[68] E. A. Wan and R. Van Der Merwe. “The unscented Kalman filter for nonlinear estimation”. In: *Proceedings of the IEEE 2000 Adaptive Systems for Signal Processing, Communications, and Control Symposium (Cat. No.00EX373)*. 2000, pp. 153–158. DOI: 10.1109/ASSPCC.2000.882463.

[69] E. A. Wan and R. Van Der Merwe. “The unscented Kalman filter for nonlinear estimation”. In: *Proceedings of the IEEE 2000 Adaptive Systems for Signal Processing, Communications, and Control Symposium (Cat. No.00EX373)*. 2000, pp. 153–158. DOI: 10.1109/ASSPCC.2000.882463.

[70] Eric A Wan and Rudolph Van Der Merwe. “The unscented Kalman filter for nonlinear estimation”. In: *Proceedings of the IEEE 2000 Adaptive Systems*

for Signal Processing, Communications, and Control Symposium (Cat. No. 00EX373). Ieee. 2000, pp. 153–158.

[71] M. Wang. "Data Fusion of MEMs IMU/GPS Integrated System for Autonomous Land Vehicle". In: *2006 IEEE International Conference on Information Acquisition*. IEEE. 2006, pp. 80–84.

[72] L. Wei, C. Cappelle, and Y. Ruichek. "Camera/laser/GPS Fusion Method for Vehicle Positioning Under Extended NIS-based Sensor Validation". In: *IEEE Transactions on Instrumentation and Measurement* 62.11 (2013), pp. 3110–3122.

[73] S.A.S. Werness et al. "Moving target imaging algorithm for SAR data". In: *IEEE Transactions on Aerospace and Electronic Systems* 26.1 (1990), pp. 57–67. DOI: 10.1109/7.53413.

[74] X. Wang, J. Guo, and N. Cui. "Adaptive extended Kalman filtering applied to low-cost MEMS IMU/GPS integration for UAV". In: *2009 International Conference on Mechatronics and Automation*. 2009, pp. 2214–2218.

[75] Y. Xu et al. "Research on Particle Filter Tracking Method Based on Kalman Filter". In: *2018 2nd IEEE Advanced Information Management,Communicates,Electronic and Automation Control Conference (IMCEC)*. 2018, pp. 1564–1568. DOI: 10.1109/IMCEC.2018.8469578.

[76] M.B. Yeary et al. "Spectral Signature Calculations and Target Tracking for Remote Sensing". In: *IEEE Transactions on Instrumentation and Measurement* 55.4 (2006), pp. 1430–1442.

[77] Y. Zhai and M. Yeary. "Implementing Particle Filters with Metropolis-Hastings Algorithms". In: *Region 5 Conference: Annual Technical and Leadership Workshop, 2004*. IEEE. 2004, pp. 149–152.

[78] Y. Zhai, M. Yeary, and S. Nemati. “Enhanced Video Surveillance Using a Multiple Model Particle Filter”. In: *2007 IEEE Workshop on Signal Processing Applications for Public Security and Forensics*. IEEE. 2007, pp. 1–4.

[79] Y. Zhai, M. Yeary, and D. Zhou. “Target Tracking Using a Particle Filter Based on the Projection Method”. In: *2007 IEEE International Conference on Acoustics, Speech and Signal Processing-ICASSP'07*. Vol. 3. IEEE. 2007, pp. III–1189.

[80] Y. Zhai et al. “A New Centralized Sensor Fusion-tracking Methodology Based on Particle Filtering for Power-aware Systems”. In: *IEEE Transactions on Instrumentation and Measurement* 57.10 (2008), pp. 2377–2387.

[81] Y. Zhai et al. “An Object-tracking Algorithm Based on Multiple-model Particle Filtering with State Partitioning”. In: *IEEE Transactions on Instrumentation and Measurement* 58.5 (2009), pp. 1797–1809.

[82] Y. Zhai et al. “Visual Target Tracking Using Improved and Computationally Efficient Particle Filtering”. In: *2006 International Conference on Image Processing*. IEEE. 2006, pp. 1757–1760.

[83] Y. Zhai et al. “Visual Tracking Using Sequential Importance Sampling with a State Partition Technique”. In: *IEEE International Conference on Image Processing 2005*. Vol. 3. IEEE. 2005, pp. III–876.